INTEGRATED MECHANISTIC ANALYSIS OF UNSTEADY AERODYNAMICS, ENERGETICS AND SCALING IN BIOFLIGHTS

生物飛行の統合力学解析：非定常空気力学、エネルギー学及びスケーリング則

February 2023

XUE YUJING

Graduate School of
Science and Engineering
CHIBA UNIVERSITY

（千葉大学審査学位論文）

INTEGRATED MECHANISTIC ANALYSIS OF UNSTEADY AERODYNAMICS, ENERGETICS AND SCALING IN BIOFLIGHTS

生物飛行の統合力学解析：非定常空気力学、エネルギー学及びスケーリング則

February 2023

XUE YUJING

Graduate School of
Science and Engineering
CHIBA UNIVERSITY

ABSTRACT

Biological flapping flights in insects, bats and birds are generally characterized by wave phenomenon in terms of flapping-wing motions and body oscillation. As most computational and experimental studies have focused on hovering flights associated with single or paired wing models, the interaction between the flying body and the flapping wings as well as the biofluid wave-based energetic scaling law in flapping forward flight remains an open question.

To tackle the central problem of unsteady aerodynamics, energetics and scaling in bio-flights, we firstly address a comprehensive computational fluid dynamic (CFD) study on insect aerodynamics and energetics at various flight velocities. A high-fidelity CFD wing-body (WB) model based on the realistic insect morphology and kinematics is built up, which enables trimmed flapping flights via a genetic algorithm embedded with a CFD-driven model. The WB interaction effects on velocity-dependent aerodynamic performance are unveiled in terms of leading-edge-vortex-based and body-vortex-based mechanisms as well as their correlations with the generation of aerodynamic forces and power consumption. While leading-edge-vortices are a convergent mechanism responsible for creating most of the aerodynamic force, the body-vortices created by WB interactions can augment the vertical force at all flight velocities, producing a 10% increase in fast flights. The time-averaged body-mass-specific mechanical power produces a *J*-shaped curve, which lowers power costs in intermediate- and high-velocity flights and saves energy from the WB interaction.

Further extensive investigation into energetics and scaling is to unravel a universal macro-aerodynamic principle to unify the biofluid wave by deriving a scaling argument *We*, which correlates the transition of wave energy between transverse (lateral motion of flapping wings) and longitudinal (forward movement of body) wave with energetic cost, linking flight speed to wing kinematics, wing-to-body mass ratio as well as gravity. Through experimental observations and high-fidelity CFD simulations, we uncover a universal scaling law that bio-locomotors obey a specific *Re*-*We* relation covering all the

bio-fluid regimes and they could maximize the flight-speed-specific *We* via regulating stroke frequency and amplitude. We infer that the wave phenomenon in bio-locomotion is an ultimate propulsive strategy as consequence of evolution in nature, which may help to give solutions and provide design guideline for future biomimetic flapping micro air vehicles.

Key words: forward flight, computational fluid dynamics, flapping aerodynamics, energetics, scaling law

Acknowledgement

Years of my doctoral experience are fleeting, looking back on the past, this precious time has given me plenty of transitions and experiences, precipitation and peace, memories and warmth.

First, I would like to express my respect and gratitude to my dear supervisor Prof. Hao Liu. The great academic vision and pursuit of him inspire my initial belief in the scientific world. He always offers patient guidance during my research exploration and clears the obstacles in the way of my growth. His virtuousness and gentleness have influenced my attitude toward life and my determination to achieve long-term goals. I am very fortunate to have met such a good mentor at the beginning of my research life.

Special thanks go to the scientists who give me selfless help during my Ph.D. period, Prof. Dmitry Kolomenskiy and Prof. Toshiyuki Nakata. Their enthusiasm and rigor for academic issues have deeply influenced me. Their professional knowledge and valuable advice offer me much help to solve academic problems.

I also want to give my gratitude to Dr. Xuefei Cai, Dr. Ru Xu and Xiangdong Zhang for their devotion and support in my daily research. They are not only collaborators but also friends, who always give me tremendous guidance and courage in the past years. I also appreciate the selflessness and dedication of Tamiko Kanke and Jing Fang, as well as all the other lab members at both Chiba University and Shanghai Jiao Tong University. They are sources of warmth and happiness on ordinary days during COVID-19.

Thanks to my family and boyfriend who have always been my strong backing. They create a warm and loving growth environment for me, willing to be my earth, and let me fly higher. Their existence enables me to have a spiritual harbor and the courage to move forward, no matter what setbacks and difficulties I encounter.

Read more, travel more. The doctoral stage is a precious pearl in the growing river of

my entire life and the fruits of the future are still waiting for me to achieve. Hope I can maintain the original intention and go my way.

Our research acknowledges the support from the Japan Society for the Promotion of Science (KAKENHI No. 18K13693 and No. 19H02060).

Yujing Xue

Chiba University

February 2023

Contents

Chapter 1 General introduction

1.1 Macroscopic flapping propulsion in bio-locomotion

The flapping wing motions as one of finest experiments in nature has been widely adopted as a propulsive strategy to achieve locomotion by million species of flying insects, bats and birds. Typically, the insect flapping-wing motion consists of rotational motion between strokes and translational motion during the down and up strokes. These complex motions generate the aerodynamic forces in various flight environments and significantly enhance the maneuverability of flyers [4]. With the sensorimotor pathways to realize power transition from muscles to wings [8], flying insects can achieve excellent flight performance by continuously varying their flapping wing kinematics [6]. Insect flapping flight employs a closed-loop, highly integrated system that contains a system of inner working and an external mechanical system. The nonlinear internal working system is composed of musculoskeletal mechanics and sensorimotor neurobiology [8]. Meanwhile, the passive open-loop external mechanical system create aerodynamic force and maintain maneuverability via integrating the wing-body kinematics, the flapping aerodynamics, the body dynamics, and the mechanisms of flight stabilization [8].

With the rapid development of micro air vehicles (MAV), insects and birds biomimetic research has been a new mainstream in the interdisciplinary field of biomechanics and biomimetic flight robots. Tremendous efforts have been made to unveil the insect and bird flight mechanics [5]. In particular, unraveling the wing-body unsteady aerodynamics, energetics and scaling law in macroscopic biological flapping flights are the core scientific problems for innovative design of the biomimetic micro air vehicles that realize efficient propulsion in various environments.

1.2 Wing-body kinematics and unsteady aerodynamics

Hovering flight has attracted considerable attention in previous insect studies, as its ease of staying a particular point in space for experimental observation and theoretical and computational modeling. The insect flapping aerodynamics is characterized by vortical structures on the wing with large-scale, combined with complicated wing-body kinematics and elastic structures [10, 11, 13, 15]. However, extensive studies on forward flapping flight are more significant, as flying insects spend most of their lifetime perform forward flights for migration, prey hunting and territory. Toughness on both experimental and computational studies obstacles the previous exploration on forward flight mechanisms of flying insects. High-speed video filming should be achieved in wind tunnels on tethered or freely fling insects in various forward flight velocities with challenges in recording and tracking the wing-body kinematics with high resolution. Ennos [16] filmed the free flight of several typical insect species and summarized their morphological and kinematic measurements. Tobalske *et al* [17] measured the three-dimensional wing-body kinematics of rufous hummingbirds over a broad velocity of 0~12 m/s in a wind tunnel. Willmott and Ellington [18] conducted the experimental observation on the body and wing kinematics of hawkmoth *Manduca* in a series of forward flight velocities 0.9 ~ 5.0 m/s.

The flapping-wing aerodynamics for the hovering flight and forward flight of insects has been explored [9-11, 19-21] to solve a central problem involving the complex vortex dynamics and wake topology production, and their correlations with aerodynamic force generation [7, 8, 22]. Both experimental and computational studies have explored the flapping-wing-based mechanisms through high-speed video filming [16-18], conventional smoke trail [23-27], and mono-stereo particle image velocimetry (PIV) techniques [28-32]. In addition, a host of powerful CFD (computational fluid dynamics) tools has been employed to study the hovering and forward flight of fruit flies [33], bumblebees [34], dragonflies [35-37], butterflies [38, 39], cicadas [40, 41], hummingbirds [42], hawk moths

[43, 44], as well as tiny beetles [45] and wasps [46]. A variety of flapping-wing aerodynamic mechanisms have been investigated, such as delayed stall [14], clap-and-fling [47, 48], and wake-capture and rotational lift mechanisms [14, 49]. In particular, the leading-edge vortices (LEV) are likely to be a universal mechanism on the aerodynamic force enhancement in aerial animals [4, 5, 8, 13, 14, 50, 51].

Flapping aerodynamics in forward flight of insects and birds has been mainly explored in terms of unraveling the relationship between aerodynamic force production and near- and far-field vortex dynamics. Rayner [53] and later Phlips *et al* [54] investigated avian forward flights and proposed generic theoretical models to predict the aerodynamic forces and power cost based on momentum theories and vortex dynamics. Dudley [55] investigated the aerodynamic mechanisms and power requirements in 15 species of butterflies' forward flight through quasi-steady analysis. Willmott *et al* [24] carried out a series of conducted flow visualization of the transient vortical flow structures associated with tethered moths in a wind tunnel with various inflows (as forward flight) velocities from 0.4 to 5.7 m/s and found that a LEV exists in all velocities with its size increasing with increasing the flight velocities. Bomphrey *et al* [28] analyzed the tethered moths flow structures at freestream velocities of 1.2 and 3.5 m/s through DPIV (digital particle image velocimetry) technique demonstrating the LEV is continuously across the thorax region along the wingtip, which contributes significantly to supporting body weight. Srygley and Thomas [25] explored the free-flying butterflies lift-generating mechanisms in and pointed out that butterflies employ a selective combination of the LEV mechanisms, the clap and peel, and the rotational mechanisms, integrating all of them to create high lift forces in complex flights of hovering and maneuvering but merely utilizing some in steady forward flight. Nagai *et al* [56] performed both experimental and computational studies on a bumblebee wing undergoing flapping motions in some forward flight velocities and reported that the LEV with a spanwise flow is observed in downstroke with a high advance

ratio but almost invisible in upstroke. CFD-based studies of free forward flights were conducted with a fruit fly model by Yao and Yeo [57] and a hawkmoth model by Yao and Yeo [43], in which the time evolution of vortical wakes was visualized in terms of three-dimensional structures of vortex shedding and downward jet-streams and their association with lift and thrust forces production.

However, the studies on unsteady aerodynamics and energetics have been mainly focused on single or paired flapping wings, it remains poorly understood in terms of the interplay between insect body and wings at various flight velocities. The impact of the moving body and its interplay with flapping wings on vortex-dominated flow structures and aerodynamic force production has been studied experimentally for the hovering and forward flight of insects and birds. Smoke-trail-based studies on butterfly free flight [25] and on dragonfly forward flight [26] reported a LEV-like near-field flow structure across the thorax region of the body, which is in agreement with the study of Bomphrey *et al* [28] for tethered moths at freestream velocities of 1.2 and 3.5 m/s obtained via flow visualizations and digital PIV methods, suggesting a significant body-induced contribution to vertical force. CFD-based studies have also considered flapping forward flight (e.g., in cicadas [40, 41], fruit flies [57], hawk moths [43], and hummingbirds [42, 58]) and have confirmed the formation of body-based vortices attached to the upper body surface and pointed out some notable enhancements to lift stemming from the wing-body (WB) interaction in fruit fly hovering flight [59, 60] and in forward flights of cicadas [40, 41] and hummingbirds [42, 58]. Whereas these studies have focused on and have thus been limited to the flapping aerodynamics associated with hovering or some specific forward flight velocities, an overall understanding of how flying insects regulate their wing kinematics and body motion in correlation as a function of flight velocity to enhance aerodynamic force production via the WB interaction remains an open question.

In addition, few studies have investigated how the morphological and dynamic

parameters affect the WB interactions for aerodynamic force production in flapping forward flight of birds and insects. Liu *et al* [41] reported a CFD-based analysis of cicada forward flight and investigated how the minimum WB distance, body inclination angle, and reduced frequency affect lift enhancement owing to WB interactions. Wang *et al* [58] investigated the advance ratio and inclination angle of the body and how the tail shape affects the WB interaction in hummingbird forward flight. Conversely, it remains unclear how, over a broad range of flight velocities, the aspect ratio *AR* [61, 62], the wing-to-body mass ratio (WBMR) [63, 64], and the reduced frequency *k* [41] correlate with the WB interaction in terms of the unsteady aerodynamics in insect forward flight.

Motivated by these, the insect aerodynamics at various flight velocities including forward flights, particularly the wing-body interaction effects on velocity-dependent aerodynamic performance with LEV-based and body-vortex-based mechanisms, as well as their correlations with generation of aerodynamic force remains a challenge and need to be further unveiled.

1.3 Flapping energetics and power efficiency

The bio-fluid flapping energetics in biological flights has been widely studied in terms of unveiling the energy consumption and power efficiency in hovering and forward flight of insects and birds. Experimental and computational analysis based on the high-speed videography [18], simplified theoretical model [65] and computational fluid dynamics (CFD) [5] have shown a variety of energetic mechanisms correlated with wing and body morphology [64], kinematics [18] and unsteady flapping aerodynamics [5, 18, 40]. Significant features of power consumptions have been reported via various shapes of power curves against flight velocities in flapping insects of bumblebee [66] and hawkmoth [5, 65, 67] as well as flying birds of hummingbirds [68, 69], pigeons, cockatiels [69], magpies [70] and flycatcher [53, 71]. The total mechanical power is consisting of

aerodynamic requirements and inertial costs induced by aerodynamic loads and wing inertia, respectively, where the aerodynamic power for forward flight is the power required to produce vortex wake for lift and thrust production and powers needed to overcome drags [4]. The inertial power can be calculated to be the products of inertial forces on wings with the velocity [9]. Willmott and Ellington [65] investigated the inertial and aerodynamic power components associated with hawkmoth *Manduca* forward flights and reported that the inertial power reaches the highest in hovering but remains unchanged in forward flight almost equivalent to the aerodynamic power. Wan *et al* [40] showed that in cicada forward flight more power is consumed in downstroke responsible for producing sufficiently large vertical force to support the weight while comparatively less power cost is observed in upstroke to generate a thrust to overcome the body drag to move forward. It is worth noting that these studies have been conducted either at some specific flight velocities or employed simplified aerodynamic models with quasi-steady approach, the blade-momentum theory as well as the discrete vortex-sheet method [4] without taking account for the impact of wing-body interaction. An overall unraveling of the forward flight energetics over a broad range of flight velocities under a comprehensive parameter space of aspect ratio, wing-to-body mass ratio and reduced frequency are still needed.

More importantly, several universal principles scaling macroscopic flight [72] and aquatic locomotion [73] have been proposed based on the aerodynamic and energetic mechanisms covering a wide range of Reynolds number (*Re*). Taylor *et al* demonstrate the a narrow range of Strouhal number (*St*) for cruising flying and swimming animals to achieve high power efficiency [72] and further Gazzola *et al* derived a scaling relation span eight orders of Reynolds number, which links velocity to body kinematics and fluid properties. However, considering that most macroscopic locomotion in nature essentially characterize in waves, a unique biofluid wave-based scaling law for biological flight of insects, bats and birds over a broad range of *Re* and flight velocities still remain uncovered.

The energetic-optimizing strategy is of great significant for various avian and aquatic species. Typically, two dimensionless indices Froude mechanical efficiency η_{Fr} [74] and cost of transport *CoT* [74-76] has been proposed as measurements of bio-fluid energetic efficiency. Cost of transport represents the energetic cost per unit distance, aiming at minimizing input power at a certain velocity to move a certain mass [74-76]. However, optimizing the Froude efficiency represents maximizing the useful power output to power expense in the air [74]. Tucker [75] first calculated the cost of transport for a variety of walking, running and flying animals. Butler [69] found that for long-distance travel the ideal transport mode is flight and reported that regardless of transport mode CoT decreases with increase animal mass. According to Templin [77] and Shyy *et al* [4], the best cruising speed is considered corresponding to the minimum cost of transport, which is generally higher than that with minimum required flight power. Simulations on forward flight of hawkmoth indicates that long-distance migration may benefit from higher velocity, as the energy per unit distance decreases monotonically with advance ratio [43].

According to Gazzola *et al*, it seems to be a general propulsion principle to regulate cruise kinematics for optimal *St* [72]. The wing kinematics involving flapping frequency and stroke amplitude is proved to play an important role on power consumption. A significant rise in power is found over the speed range of simulated hawkmoth with a significant rise in the wingbeat frequency [43]. Honeybees could produce excess aerodynamic powers via increase flapping amplitude and keeping frequency unchanged [78]. Moreover, the computational and experimental studies on undulatory swimming made comparisons between the two energy-optimizing strategies and demonstrated that fish could regulate tail-beat frequency and amplitude to minimize CoT rather than Froude mechanical efficiency [74, 76]. Identification for the dominant energetic-optimizing strategy obeyed by broad range of bio-flyers remains still untouched.

Overall, a wave-based scaling arguments need to be proposed bringing together the

biofluid aerodynamics and wave energy expenditure through investigating the correlations with Reynolds number (*Re*) and Strouhal number (*St*) in biological flapping flights over a broad range of various species including insects, bats and birds at various flight speeds. Further, whether some combination of flapping frequency and stroke amplitude can optimize flight-velocity-specific Froude efficiency, Cost of Transport and Wave Energy number, and which propulsive strategy is the ultimate one in biological locomotion remain challenging questions and require further investigation.

1.4 Bio-inspired vehicles with flapping wings

The bio-inspired vehicles with flapping wings are now an integrated research area covering biology, computer science, mechanical engineering, and aeronautical engineering. Micro air vehicles (MAVs) fly in Reynolds number regimes of most aerial animals 10^4~10^5 or lower, normally with flight speeds of 10m/s and maximum size of 15cm. They have the advantage to monitor the complex environments and assess of emergence situations [8]. The MAVs inspired by bioflight systems have a remarkable increase recently. Numerous bio-inspired designs have been proposed, consisting of the fixed-wing, the rotary-wing as well as the flapping-wing vehicles [79, 80]. Through years of natural selection, designs of bio-flight system have been demonstrated to be alternatively scaled down in size, which also provide aerodynamics and control challenges in low-velocity autonomy. Therefore, biomimetics in bioinspired systems are required to offer novel and breakthrough mechanisms to guide the future MAVs [80].

The strategy of biomimetic MAVs in insect-inspired flight includes a control autonomy and biomimetic design system. Downsizing will lead to many challenges: unsteady aerodynamics with low Reynolds number, nonlinear control strategies, elastic wings, electromagnetic motors power density, high and fast-resolution sensing, and miniaturization [8]. It is important to achieve high power frequency for generating

sufficient lift force. It is also a must for light wings and body, which, however, offers restrictions on the combination of the actuators and power sources, leaving constraints on the size, wing kinematics, and available aerodynamic forces. Such scaling issues also result in problems related to the autonomy: they constrain the sustainable flight for long-time higher-level performances, causing higher energetic cost and lower flight stabilization. To solve these scaling issues, a systematic design would be required for the future MAVs [8].

Recently, the flapping-wing MAVs with insects or birds size have been increasingly developed [81, 84, 96]. Most of them have a mass of 10^{-2} to 10^{0} kg and a wingspan of 10^{-2} to 10^{0} m. For larger MAVs [83], vision or autonomous control systems can be payload to achieve the obstacle avoidance. Without rudders or elevators, some MAVs could also realize manoeuvring by actively control of the wing feathering motion [85]. Despite the challenges on miniaturization and small-scale propulsion, studies on bioinspired flight systems have successfully reported three prototypes, the X-wing [81, 82], the insect-like Robobee [96], and the Nano-Hummingbird [83]. The DelFly with two paired flexible wings employs the gear-crank linkage to achieve the clap-and-fling mechanism [81, 82]. For aerodynamics, the X-wing MAVs are able to augment the aerodynamic force generation benefiting from three cycles of clap-and-fling. The Nano-Hummingbird with two-wings [83] shows a wingspan of 16.5 cm and the weight of 19 g. With all the control components put together, the stability and maneuverability can be realized by the active control of the flapping wings. The Robobee [96] has the weight of 80 mg and wingspan of 30 mm, with flapping frequency of 120 Hz, which possesses the piezoelectric motors with high-power density. This MAV could achieve a tethered hovering stabilization and basic flight manoeuvres [8]. After the first successful takeoff of the Robobee, several bioinspired vehicles with flapping wings have also been developed, including the untethered autonomous flapping MAV powered with photovoltaic array [86] and the hybrid microrobot capable of transitioning between aerial and aquatic environments [2, 3].

The energy transition from motor to mechanical system of flapping wings may play a significant role on modifying the wing dynamics and enhancing the aerodynamic performance. The insect wing motor has been studied by Harne *et al* [87] as a compression 'bistable click' mechanism. They reported the amplitude and wing dynamics can be dramatically changed through a flight mechanism which could modify compression characteristics and motor axial support stiffness. These flexible structures related with wing-hinge may provide enhancement of the flexibility while achieving robustness of control autonomy based on the passive and active mechanisms [8].

Overall, the macroscopic aerodynamic and energetic scaling in bio-flights uncovering the mechanical principles for insect-inspired aerial robots require comprehensive investigation. Moreover, how the flexible structures including flexible wings and wing hinges and the deformable body [5, 12, 30, 88, 89] work interactively to retain robustness in various flight conditions leaves us future challenges to unveil the passive and active mechanisms associated with the scaling effects of body-based and wing-based control strategies in biological flights, which will further inspire flapping-wing MAVs design.

1.5 Objective and approach

This study aims at unraveling the underlying mechanisms associated with unsteady aerodynamics, energetics and scaling law in biological flapping flight over a broad range of flight velocity. We develop the wing-body morphological model of flapping insects and the realistic wing-body kinematics for hovering and forward flight with different velocities constructed from experimental data. The model is further modified for trimmed forward flight by using a genetic algorithm embedded with a CFD-driven aerodynamic model. Also introduced is a versatile and high-fidelity CFD model specifically designed for the forward flapping flight of flying insects; this model enables precise prediction of vortical dynamics, aerodynamic forces, and power consumed for various wing-body kinematics and flying

motions. In Chapter 2, an overall image of the unsteady aerodynamics with the near-field and far-field vortex-dominated flow structure is given in various forward flight velocities, including LEV-based mechanisms and wake topologies associated with the aerodynamic force production. In Chapter 3, a comprehensive analysis is conducted on the power consumption and energetic efficiency over a broad range of forward flight velocities and their correlations with aerodynamic performance. In Chapter 4, a systematic discussion is exerted on the wing-body interaction in terms of the body-vortex-based mechanisms and its effect on aerodynamic force enhancement in various forward speeds, with parametric effects of aerodynamics and energetics involving aspect ratio, wing-to-body mass ratio, and reduced frequency. In Chapter 5, a universal macro-aerodynamic principle to unify the biofluid wave is unraveled by deriving a scaling argument *We* that correlates the transition of wave energy with energetic cost, allowing an extensive identification of the ultimate propulsive strategy in biological flights. In Chapter 6, an insect-inspired wing kinematics-based flight control strategy optimized by deep reinforcement learning is developed tasked with achieving robust autonomous control for bumblebee hovering stabilization under full 6-DoF large disturbances. Finally, the key findings and conclusions reached in this study as well as our perspective views on future directions are summarized in Chapter 7.

Chapter 2 Unsteady aerodynamics in insect forward flight

2.1 Introduction

In the past decades, hovering flight in insects has attracted considerable attention relating to flapping-wing aerodynamics, flight control and stability as its ease of staying a particular point in space for experimental observation and theoretical and computational modeling. The flapping-wing aerodynamics in hovering flight of insect has been studied extensively with the purpose of answering a central problem on the complex wake topology and vortex dynamics generation, and their correlations with aerodynamic force [7-11, 19-22]. A variety of flapping aerodynamic mechanisms have been proposed and investigated [14, 47-49]. In particular, the LEVs (leading-edge vortices) are probably a universal mechanism enhancing the aerodynamic force production in flying animals [4, 5, 8, 13, 14, 50, 51]. However, a comprehensive insight into the flapping aerodynamics and energetics in various forward flight velocities remains yet poorly explored.

Toughness on both experimental and computational studies obstacles the previous exploration on forward flight mechanisms of flying insects. High-speed video filming should be achieved in wind tunnels on tethered or freely fling insects in various forward flight velocities with challenges in recording and tracking the wing-body kinematics with high resolution [16-18]. It is also of difficulties to quantify the flow structures with high-resolution in insects' forward flight with conventional smoke-trail or even mono/stereo particle image velocimetry (PIV) flow-visualization techniques [28-32]. CFD-based studies provide another powerful tool for quantifying while clarifying the complex near-field and far-field vortical structures with wake topology, vortex dynamics, and the aerodynamic performance in forward flights of various insects and birds [33-46].

The main subject in the previous studies however has been focused on and limited to the flapping aerodynamics in forward flight at one or two certain velocities.

Flapping aerodynamics in forward flight of insects and birds has been mainly explored in terms of unraveling the relationship between aerodynamic force production and vortex dynamics [24-25, 28, 53-56]. CFD-based studies of free forward flights were conducted with a fruit fly model by Yao and Yeo [57] and a hawkmoth model by Yao and Yeo [43], in which the time evolution of vortical wakes was visualized in terms of three-dimensional structures of vortex shedding and downward jet-streams and their association with lift and thrust forces production. However, compared with our understanding of hovering aerodynamics in insect flight, a central question on how the forward flight aerodynamics in flying insects correlates with various flight velocities and flying motions, in terms of the LEV mechanisms, the wake topology including vortex dynamics and downwash jet-stream, the lift and thrust force production, the wing-body interaction as well as the wing-body kinematics, remains yet open.

In this chapter, we unravel the underlying mechanisms associated with flapping aerodynamics in forward flight of insects over a broad range of flight velocity. We describe a wing-body morphology of *Manduca Sexta*, and the realistic wing-body kinematics comprising hovering and five forward flights, which are constructed based on experimental data and further modified for trimmed forward flights with a genetic algorithm embedded with a CFD-driven aerodynamic model. A versatile and high-fidelity CFD model that is specified for the forward flapping flight of flying insects is further introduced, which enables precise prediction of vortical dynamics, aerodynamic forces and torques as well as power with different wing-body kinematics. An overall image of the near-field and far-field flow is given in various forward flight velocities, including LEV-based mechanisms and wake topologies; a comprehensive analysis is conducted on the aerodynamic force production in the forward flights and their correlations with the LEV

dynamics.

2.2 Morphological and kinematics models

We construct a WB morphological model of the hawk moth *Manduca Sexta* and mimic the realistic WB kinematics based on experiments from Willmott and Ellington [18, 65], which cover a broad range of flight velocities. Detailed morphological parameters of the hawk moth are listed in Table 2-1: the wing length R = 50.64 mm, the body length L = 41.85 mm, and wing mean chord length c_m = 18.6 mm are used as reference lengths. The wing aspect ratio $AR = 2R^2/S_w$, where the single wing area $S_w = c_m R$. The body mass m_b = 1.995 mg and the WBMR is 4.49%. Note that we define the ratio between wing mass m_w and body mass m_b as the wing-to-body mass ratio (WBMR) $\varepsilon = m_w/m_b$.

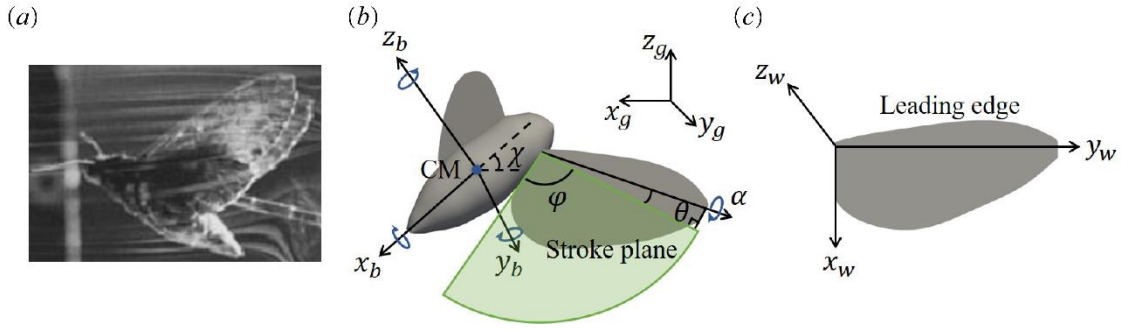

Fig. 2-1 (*a*) Morphology of the hawk moth *Manduca Sexta* during fast forward flight [24]. (*b*) Schematic of coordinate systems and WB kinematic parameters of a hawk moth model. (*c*) Definition of a wing-fixed (x_w, y_w, z_w) coordinate system.

Table 2-1 Morphology of hawk moth *Manduca Sexta*

Species	m_b (mg)	m_w (mg)	ε (%)	L (mm)	R (mm)	c_m (mm)	AR
Hawk moth	1995	89.58	4.49	41.85	50.64	18.6	5.445

The realistic WB kinematic model is composed of a pair of flapping wings and a moving body and mimicks the flapping flight from hovering to forward flight at five typical velocities [9]. Fig. 2-1 defines three coordinate systems: global (x_g, y_g, z_g),

body-fixed (x_b, y_b, z_b), and wing-fixed (x_w, y_w, z_w). The kinematics of body is represented by the stroke plane angle β_{SP} and the body inclination angle χ, which vary with flight speed. The positional angle φ is the rotation axis projection of sweep angle within the stroke plane, the feathering angle α is the geometric angle of attack around the rotation axis, the deviation angle between stroke plane and rotation axis is the elevation angle θ. The wing kinematics is defined by the three angles expressed as the first three terms of a Fourier series [9], the positional φ, elevation θ, and feathering angle α are as follows:

$$\begin{aligned}\varphi(t) &= \sum_{n=0}^{3}[\varphi_{cn}\cos(n\omega t) + \varphi_{sn}\sin(n\omega t)],\\ \theta(t) &= \sum_{n=0}^{3}[\theta_{cn}\cos(n\omega t) + \theta_{sn}\sin(n\omega t)],\\ \alpha(t) &= \sum_{n=0}^{3}[\alpha_{cn}\cos(n\omega t) + \alpha_{sn}\sin(n\omega t)],\end{aligned} \qquad (2-1)$$

where ω means the flapping frequency and n is from 0 to 3. This first three Fourier terms-expressed kinematic model (Eq. 2-1) has been verified to well fit to the experimental measurements [18], and by many numerical studies [9, 10, 21] to be able to reasonably mimicking the flapping-wing kinematics for various real species. The coefficients φ_{cn}, φ_{sn}, θ_{cn}, θ_{sn}, α_{cn}, and α_{sn} for all flying motions and flight velocities are determined based on measurements by Willmott and Ellington of tethered flights in a wind tunnel [18]. A list of flapping frequency f, stroke amplitude Φ, body angle χ and stroke plane angle β_{SP} appears in Table 2-2 and shows that the flapping frequency fluctuates slightly but within a narrow range of 24.8–26.1 Hz for hovering and five flight velocities. Upon increasing the flight velocity, the body angle decreases, whereas the stroke plane angle clearly increases.

Table 2-2 Measured wing-body kinematic parameters of *Manduca Sexta* in hovering and various forward flight. Data from Willmott and Ellington [18].

Speed (m/s)	f (Hz)	Φ (deg.)	χ (deg.)	β_{SP} (deg.)
Hovering	25.4	113.2	33.9	23.4

0.9	25.6	105.5	27.8	23.3
2.1	24.8	99.5	25.8	37.6
2.9	26.1	97.1	19.9	44.4
3.8	24.8	102.7	20.0	52.7
5.0	25.0	103.9	18.0	56.4

2.3 A bio-inspired dynamic flight simulator

A bio-inspired, dynamic flight simulator [9] has been utilized, which allows versatile integrable modeling of realistic geometries, WB kinematics, and the aerodynamics of flapping-induced hovering and forward flights. We employ a fortified Navier–Stokes solver based on finite-volume method with a dynamically moving overset-grid multi-blocked system, which was verified to be self-consistent for incompressible flows (see Fig. 2-2). Through adding forcing terms into NS equations, the fortified algorithm could be achieved, which is further discretized through replacement of the term related with time employing the Pade scheme with second-order accuracy of implicit Euler scheme [9]. The solver was also validated through a variety of benchmark tests able to predicting unsteady aerodynamics with vortex structures, forces and torques, power consumption and energetics for Reynolds numbers *Re* ranging from 10^1 to 10^4 for different insects species [4, 10, 11, 21, 64, 88, 90, 91]. The morphological model is constructed through a wing-body grid generator, which could reconstruct geometry via differential geometric method. Fig. 2-2 depicts the geometry and grid system of CFD insect model.

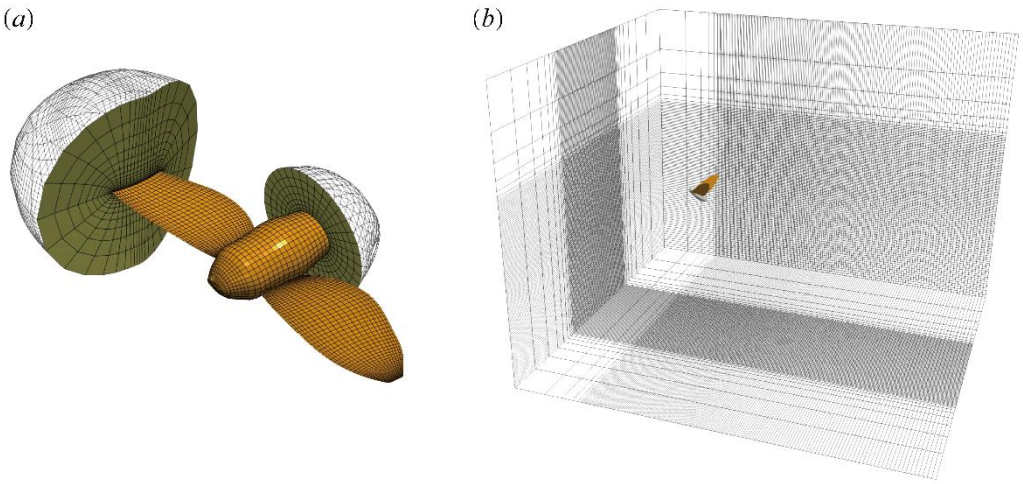

Fig. 2-2 (*a*) Overset-grid and multi-blocked systems of a hawk-moth CFD model comprising two wing blocks and one body block, as well as (*b*) a background grid block.

We conduct an extensive study in terms of the grid dependency for the current model, which contains four overset grid blocks: right- and left-wing grids (39×65×22) with assumed wing thickness of $0.002c_m$, a body grid (37×39×9), and a background grid (165×101×113) for resolving the near- and far-field vortical structures. Verification of the self-consistency were performed and confirmed through comparisons (Fig. 2-3) of time-varying aerodynamic horizontal and vertical forces as well as the pitch torque in hovering flight among different cases: *Case 1*, coarse mesh (body grid: 31×33×7, wing grid: 33×55×19, background grid: 77×85×57), time step $dt = 0.0005T$; *Case 2*, medium mesh (body grid: 37×39×9, wing grid: 39×65×22, background grid: 93×101×69), time step $dt = 0.0005T$; *Case 3*, fine mesh (wing grid: 47×79×27, body grid: 45×47×11, background grid: 111×121×81), time step $dt = 0.0005T$. Our results obviously show marginal discrepancy among different cases.

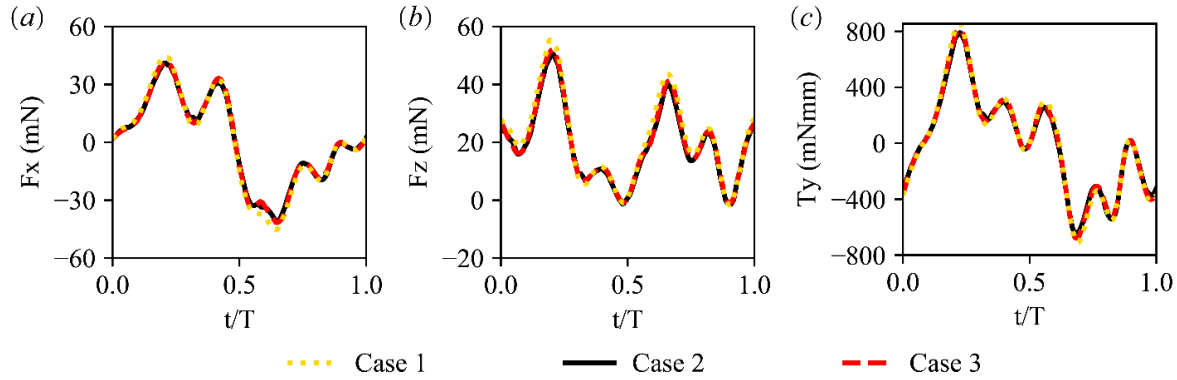

Fig. 2-3 Grid density effect on the time course of forces and torque in a wing-beat stroke of hovering flight in three cases. (*a*) Horizontal force F_x; (*b*) Vertical force F_z; (*c*) Pitch torque T_y.

The energetics in flapping-induced forward flight is evaluated via power consumption (i.e., the mechanical power [9]), which consists of aerodynamic and inertial powers. The aerodynamic forces F_{aero} exerted on the moving body and flapping wings are calculated by integrating over all cells (total cell number *N*) on the wing and body surfaces:

$$\boldsymbol{F}_{aero}(F_x, F_y, F_z) = -\sum_{i}^{N} (\boldsymbol{Flux}_{invis} + \boldsymbol{Flux}_{vis}), \qquad (2-2)$$

in which three force components of F_x, F_y, F_z, as defined in the global system (Fig. 2-1), denote the horizontal force F_x in forward direction, the lateral force F_y, and the vertical force F_z, which is normal to the forward velocity *V*.

2.4 Trimmed forward flight

The estimate of the aerodynamics and energetics of flapping-induced forward flight may be influenced by any unbalanced conditions between free flight and tethered flight at a specific flying velocity. Considering that the WB kinematics is based on the tethered flight measurements [18, 65], we developed a method to ensure the consistency of the CFD modeling by modifying the kinematics of flapping wings to achieve trimmed flights of the hawk-moth model for hovering and forward flight at five velocities.

The trimmed flights are required to satisfy three conditions: the cycle-averaged

forward and backward forces sum to zero, the cycle-averaged vertical force balances weight, and the cycle-averaged pitch torque equals zero. Note that, according to Willmott and Ellington [18], the forward flight with a velocity of 5 m/s was an exception in their experiments because the hawk moths were unable to fly steadily, implying that there might be relatively large errors compared with the other four flight velocities. Note that we fixed here the stroke plane and body angle for each velocity based on the experiments by Willmott and Ellington [18] because very small variations appeared in wind tunnel experiments with a fluctuation around 2°–3° associated with the resultant body inclination due to the relative orientations of the thorax and abdomen [18].

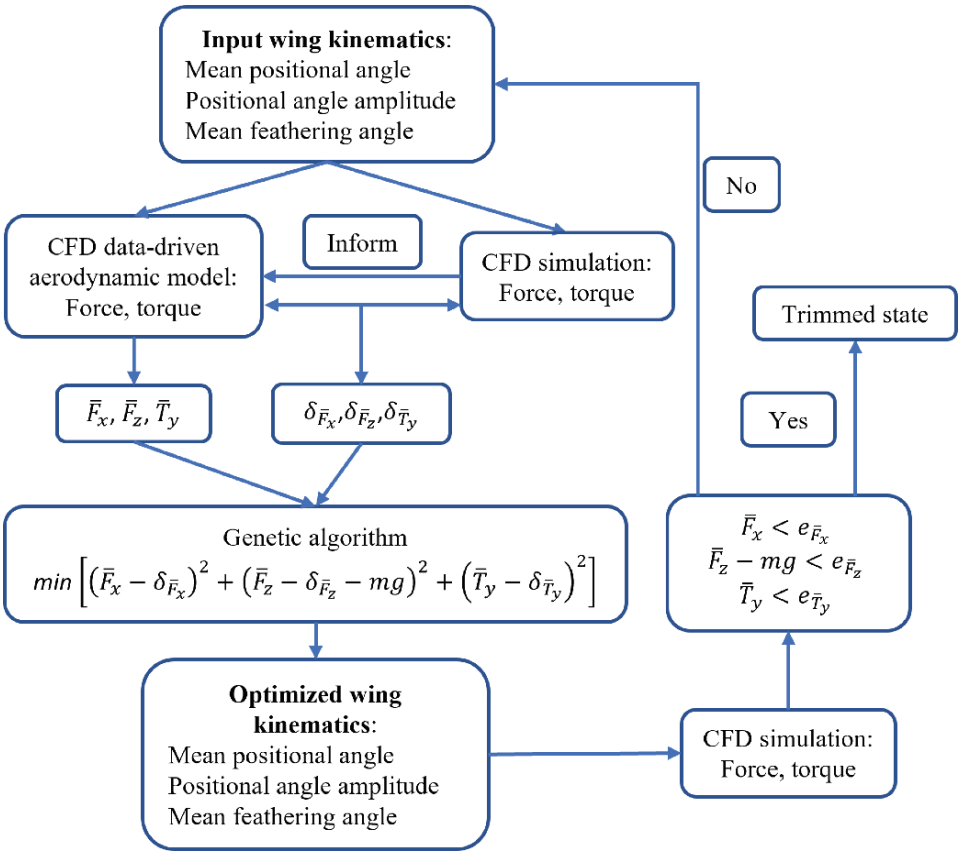

Fig. 2-4 Flow chart of approach to determine trimmed flights (more details are available in Cai *et al.* [92]).

The wing kinematics is finely tuned through an optimal procedure by using a genetic algorithm with the covariance matrix adaptation -based derandomized evolution strategy

[93][94], which is embedded with a CFD data-driven aerodynamic model (CDAM) developed by Cai *et al.* [92]. Fig. 2-4 shows the flowchart to determine the trimmed flights in association with hovering and five forward-flight velocities for a hawk moth. A CFD simulation is first conducted with an initial input of the wing kinematics measured to obtain aerodynamic loads, which are used to identify the coefficients for CDAM to improve the numerical accuracy. With respect to the numerical errors that may exist between the CDAM-based prediction and the CFD results, which are defined as $\delta_{\bar{F}_x}$, $\delta_{\bar{F}_z}$, and $\delta_{\bar{T}_y}$, we use the genetic algorithm to minimize the objective function $\left(\bar{F}_x - \delta_{\bar{F}_x}\right)^2 + \left(\bar{F}_z - \delta_{\bar{F}_z} - m_t g\right)^2 + \left(\bar{T}_y - \delta_{\bar{T}_y}\right)^2$, in which the mean positional angle, the positional angle amplitude, and the mean feathering angle serve as variables. Note that the horizontal aerodynamic force $\bar{F}_x$, the vertical aerodynamic force $\bar{F}_z$, and the aerodynamic pitch moment $\bar{T}_y$ are estimated based on the informed CDAM [92]. In principle, the objective function can be minimized upon approaching zero, leading to the perfect satisfaction of the trim conditions with the wing kinematics. This is then verified by investigating whether the CFD-based hawk-moth flight with the adjusted wing kinematics meets the trim conditions in terms of zero net vertical and horizontal forces and pitch torque. If so, trimmed flight is achieved, and the approach is terminated; if not, the wing kinematics obtained is treated as a new input of the wing kinematics for the next search iteration.

Table 2-3 Mean aerodynamic forces and pitch torques of the trimmed flights in hovering and five forward flight velocities.

Velocity (m/s)	$\bar{F}_x/m_t g$	$\bar{F}_z/m_t g$	$\bar{T}_y/m_t gL$
Hovering	0.03	0.94	0.003
0.9	0.04	0.97	−0.002
2.1	0.01	0.95	0.006
2.9	0.07	1.01	0.014
3.8	0.10	1.04	0.015
5.0	0.04	0.98	−0.016

The adjusted wing kinematics for the trimmed flights comprising hovering and five forward flights is verified to reasonably satisfy the trim conditions via comparing the

time-averaged aerodynamic forces to the hawk moth weight (Table 2-3). The calculated mean vertical forces in all velocities are large enough to support more than 94% of the hawk moth's weight, while the mean horizontal forces are less than 7% of the weight, with the exception of a relatively large horizontal force for forward flight at 3.8 m/s because of the need to avoid overlapping of the two wings during trimming. The pitch-torque-related errors are marginal, at less than 2% of the reference torque $\bar{T}_{y_{ref}} = m_t g L$, where m_t denotes the total mass and L is the body length of the hawk-moth model. Thus, it is reasonable to consider that the trimmed flights are achieved approximately for all flight velocities. Details of the adjusted wing kinematics in hovering and in the five forward flights of 0.9, 2.1, 2.9, 3.8, and 5.0 m/s along with the measurements are given in Fig. 2-5.

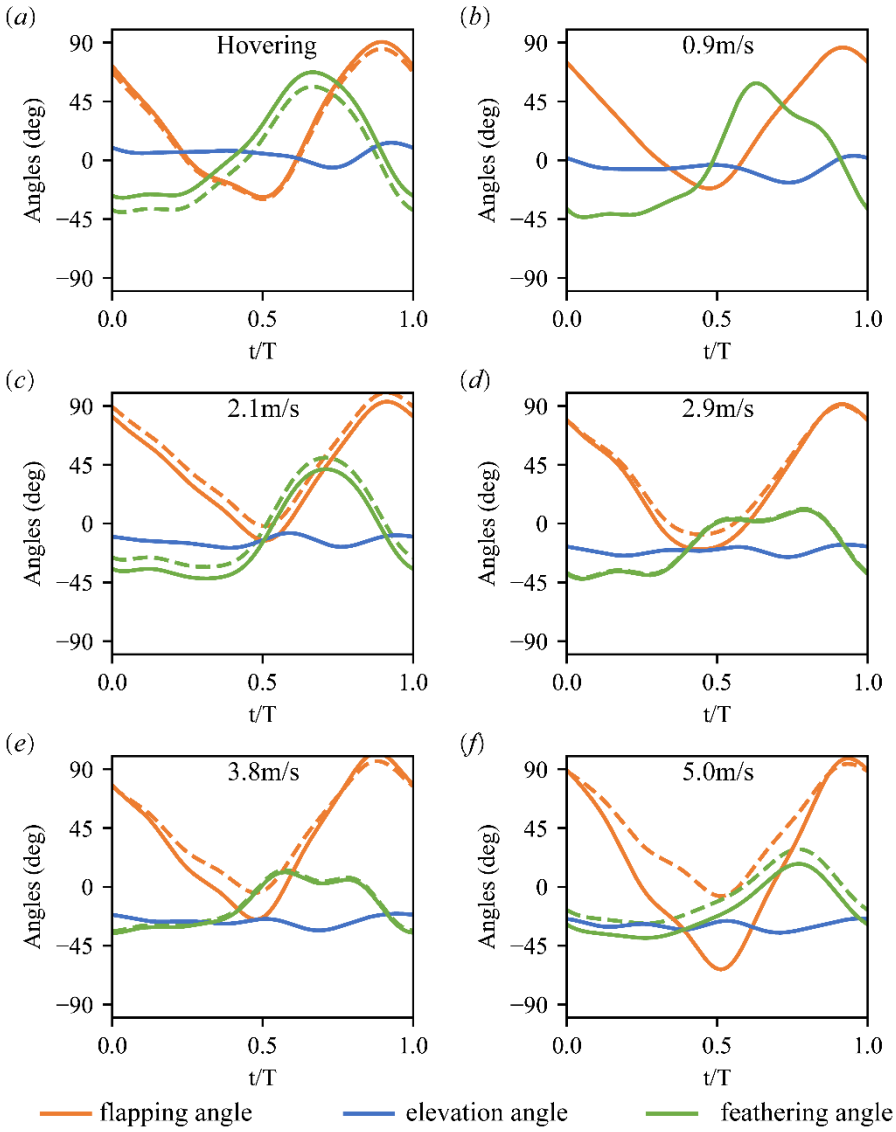

Fig. 2-5 Resultant wing kinematics for trimmed flight (solid line) along with the experimentally measured wing kinematics (dashed line) in hovering (*a*) and five forward flight velocities of 0.9 m/s(*b*), 2.1 m/s(*c*), 2.9 m/s(*d*), 3.8 m/s(*e*), and 5.0 m/s(*f*).

2.5 Near and far field flow structures in forward flight

Near-field vortex dynamics for hawkmoth in hovering and forward flights with velocities of 2.1m/s and 3.8m/s are visualized at the time instants as marked points in

time-course of positional angles (Fig. 2-6). The iso-surface of Q-criterion [95] with $Q = \frac{1}{2}(\|\boldsymbol{\Omega}\|^2 - \|\boldsymbol{S}\|^2) > 0$ is used to identify the vortex structure, where $\boldsymbol{S} = \frac{1}{2}[\nabla \boldsymbol{u} + (\nabla \boldsymbol{u})^T]$ and $\boldsymbol{\Omega} = \frac{1}{2}[\nabla \boldsymbol{u} - (\nabla \boldsymbol{u})^T]$ denote the strain-rate and vorticity tensors, respectively, and $\boldsymbol{u}$ represents the velocity vector. Normalized helicity density is employed in a fashion of color mapping to illustrate the rotational directions of vorticity as illustrated in Fig. 2-7, 2-8 and 2-9.

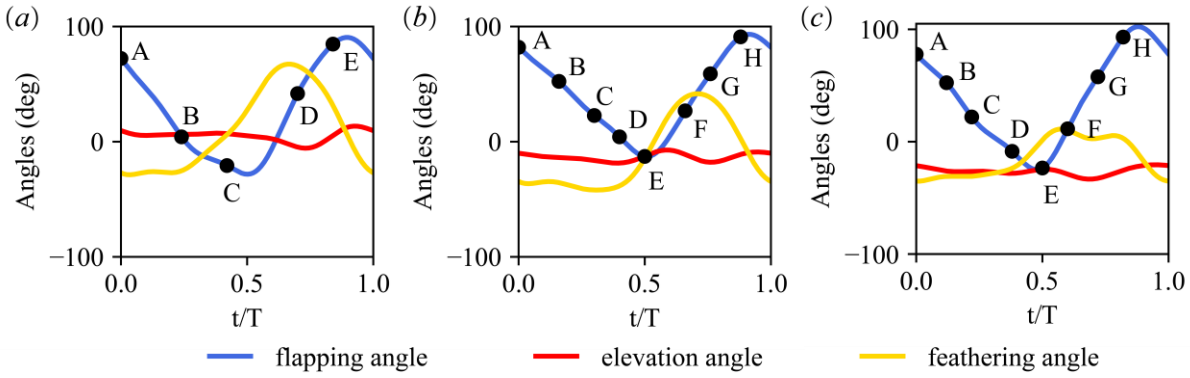

Fig. 2-6 Time courses of positional, elevation and feathering angles: (*a*) hovering flight, (*b*) slow forward flight (2.1m/s), (*c*) fast forward flight (3.8m/s).

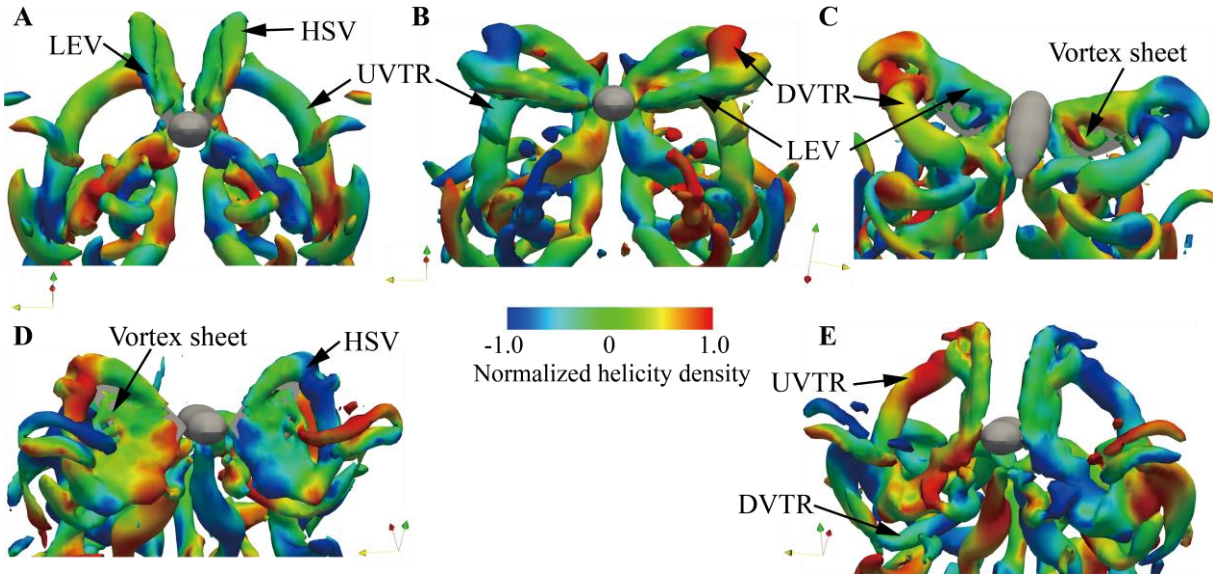

Fig. 2-7 Near-field vortical structures of a hovering hawkmoth model at five instants, *t/T* = 0.0 (**A**), 0.24 (**B**), 0.42 (**C**), 0.70 (**D**), 0.84 (**E**), in a wing beat (Fig. 2-6 (*a*)).

Near-field flow structures

In hovering flight, the near field vortex structures are observed well consistent with those in our previous studies [9, 11]. A horseshoe vortex (HSV) composed of trailing-edge vortex (TEV), leading-edge vortex (LEV), and tip vortex (TV) generates at early downstroke (Fig. 2-7A). As the TEV and LEV grow in strength and size, the trailing-edge vortex then detaches remaining connection with TV. Subsequently, these vortices merge with each other, forming a downstroke vortex tube ring (DVTR) (Fig. 2-7B). This vortex tube ring creates a three-dimensional roll-up vortex sheet (Fig. 2-7C) and a core downward jet [9]. At upstroke (Fig. 2-7D, E), similar HSV and an upstroke vortex tube ring (UVTR) are observed; the UVTR pair connects with the DVTR, displaying an elongated vortex ring shape.

For the trimmed fast forward flight with a speed of 3.8 m/s, compared with hovering flight, a distinct discrepancy lies in the appearance of a body vortex: while the HSV including LEV, TV and TEV (Fig. 2-8 (*a*)A) displays some similarity with that in hovering, an intense body vortex is observed attaching to the upper body overbridging the LEVs generated by the two wings. This phenomenon is also captured computationally in flying cicada at velocities of 1.96 m/s [41] and 2.21 m/s [40], respectively. Moreover, the body vortex comprises a rear-body vortex and a thorax vortex during downstroke. At early downstroke, the rear-body vortex appears at wing base, crossing the upper surface of the body and connecting to the detached LEV and the TEV; eventually the rear-body vortex merges with a head vortex as well as LEV, TV and TEV, forming a downstroke vortex tube ring (DVTR) in a fashion of heart-shape closed-loop (Fig. 2-8 (*a*)B). In mid-downstroke, the rear-body vortex moves backward, developing into two spiral vortex tubes attached onto the aft of the body, as a portion of the DVTR (Fig. 2-8 (*a*)C). In addition, an intense thorax vortex is observed at the thorax, connecting to the head vortex and the rear-body vortex while the DVTR elongates with an inclination from horizontal direction at late

downstroke (Fig. 2-8 (*a*)D).

At early upstroke (Fig. 2-8 (*b*)E), the thorax vortex presents a fast grow in strength and the upstroke LEV starts to shed from leading-edge. Similarly, an integration of the thorax vortex, the head vortex as well as LEV, TV and TEV forms an upstroke vortex tube ring (UVTR) wrapping the two wings (Fig. 2-8 (*b*)F) while the rear-body vortex detaches from the tail. During the end of the upstroke, a breakdown can be observed between the thorax and head vortices while the thorax vortex moves backward, detaching onto the aft body. The UVTR develops downward while deforming, eventually merging with the largely elongated DVTR, eventually forming a wake sheet with an inclination (Fig. 2-8 (*b*)G, H).

Visualization of the near-field flow structures at the velocity of 2.1 m/s (Fig. 2-9) shows that the body vortex is a distinguished feature in the slow forward flight: the thorax vortex is not much intense enough to move rearward but eventually decays and vanishes at the aft body. At early downstroke, the rear-body vortex appears cross the upper body surface (Fig. 2-9 (*a*)A), growing and connecting to the head vortex and LEV and TEV, substantially forming a DVTR (Fig. 2-9 (*a*) B). At mid-downstroke, a similar thorax vortex is observed together with the rear-body vortex, which moves backward in a form of dual body vortices (Fig. 2-9 (*a*)C, D). When the DVTR elongates horizontally (Fig. 2-9 (*b*)E, F), the downstroke thorax vortex develops while connecting to the upstroke LEV, TV and TEV, creating a UVTR (Fig. 2-9 (*b*)G). Note that the thorax vortex remains attached onto the thorax region, substantially forming the subsequent downstroke body vortex (Fig. 2-9 (*b*)H).

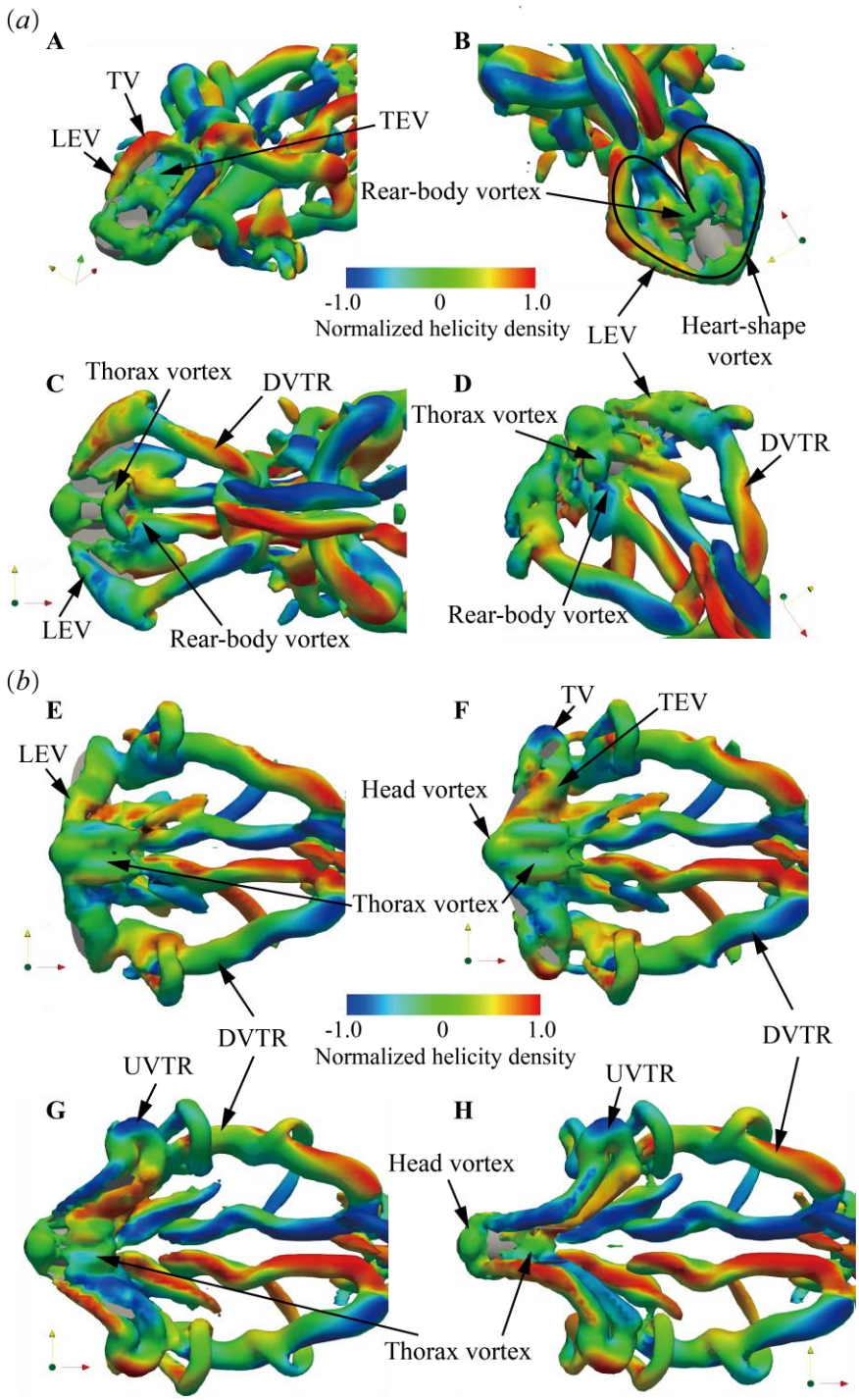

Fig. 2-8 Near-field vortex structures of hawkmoth model at fast forward flight velocity of 3.8m/s at 8 instants as marked in Fig. 2-6 (*c*): (*a*) Downstroke at *t*/*T* = 0.0 (**A**), 0.12 (**B**), 0.22 (**C**), 0.38 (**D**); (*b*) Upstroke at *t*/*T* = 0.50 (**E**), 0.60 (**F**), 0.72 (**G**), 0.82 (**F**).

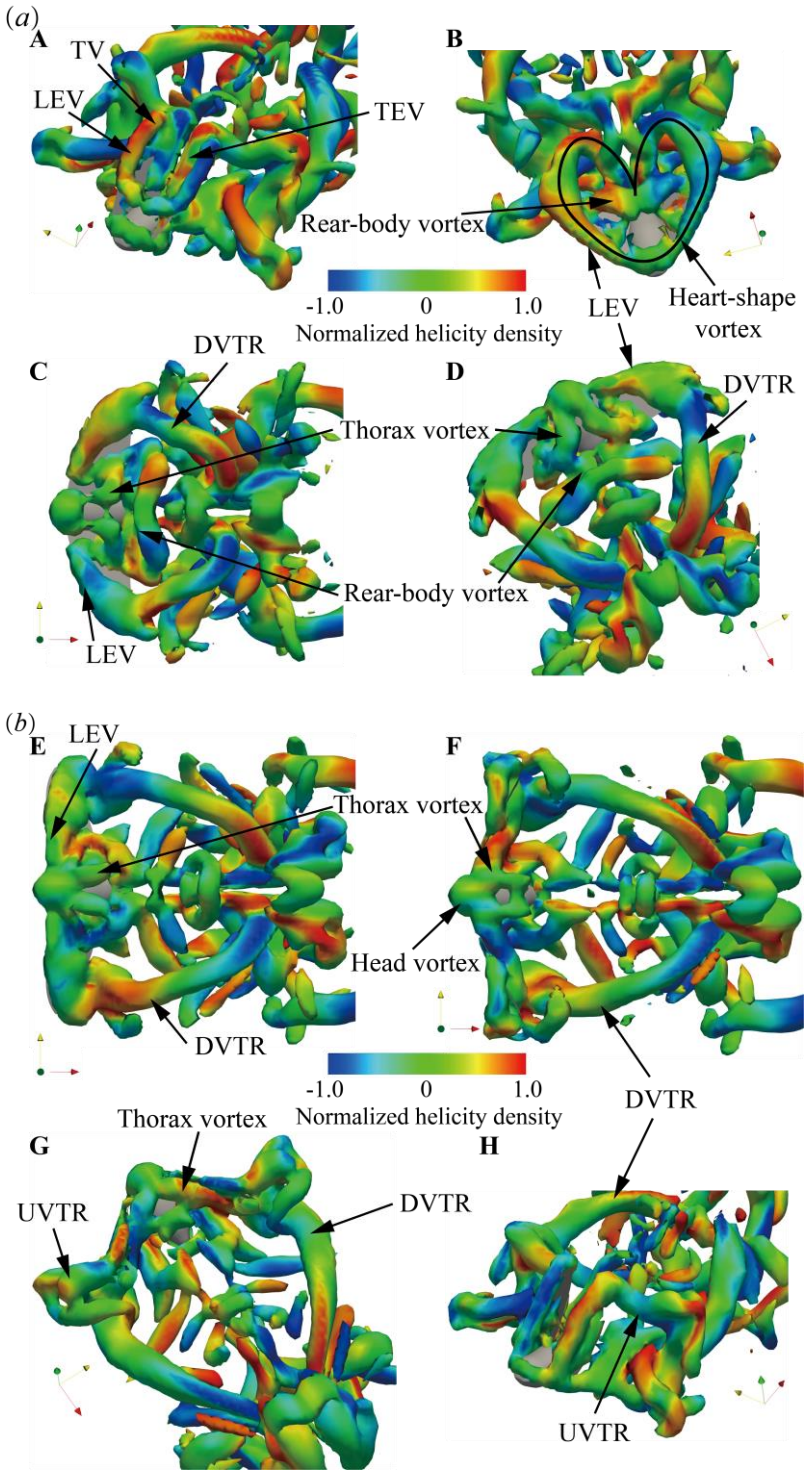

Fig. 2-9 Near-field vortex structures of hawkmoth model at slow forward flight velocity of 2.1m/s at 8 instants as marked in Fig. 2-6 (*b*): (*a*) Downstroke at *t*/*T* = 0.0 (**A**), 0.16 (**B**), 0.30 (**C**), 0.40 (**D**); (*b*) Upstroke at *t*/*T* = 0.50 (**E**), 0.66 (**F**), 0.76 (**G**), 0.88 (**F**).

Far-field flow structures

The far-field flow structures in various forward flight velocities are further visualized in terms of wake topology and downwash as illustrated in Fig. 2-10, 2-11. In hovering flight, the wake presents two intense jets in vortex tube rings (VTR) core below each wing forming the hovering downwash [9]. For forward flight, the wake topology characterized by continuously shedding VTR with the attached body vortex shows an inclination, terms here as the downward angle to horizontal direction (Fig. 2-11 (*fi*)). In slow forward flight, the wake is of complicated structure with the shedding vortices intertwined with a mutual induced field [43]. The downstroke vortex tube rings (DVTR) shed, connecting to the preceding upstroke vortex tube rings (UVTR) and stretching almost horizontally with increasing length as the forward flight velocity increases, which is well consistent with the experiment by Willmott *et al* [24]. Furthermore, the downwash wake shows a specific high induced-velocity region at the VTR core (Fig. 2-11), forming the alternate downward and upward jets in the core of DVTR and UVTR, respectively, particularly in fast forward flight. It indicates that the vertical force production is mainly achieved during downstroke of forward flight while the upstroke may contribution less particularly in fast forward flight.

To quantify the correlations between the downwashes and flight velocities, we herein introduce an index, called downwash angle based on the downwash velocity *w* contours in a cutting plane located at the symmetry plane of hawkmoth's body (Fig. 2-11), defined as:

$$\theta_{downwash} = -\tan^{-1}\left(\frac{1}{n}\sum_{i=1}^{n}\frac{z_i - z_0}{x_i - x_0}\right), \qquad (2-3)$$

where *n* is an integer utilized for representing the shedding DVTR and UVTR in the *n*-th preceding stroke, (x_0, z_0) is the CM position, and (x_i, z_i) is the sideview positions on the cutting plane corresponding to the maximum downwash velocity *w* in the *i*-th preceding stroke. Similar with the body inclinations measured in different flight velocities, the downwash angle shows a decline trend from hovering to fast forward flight (Fig. 2-12). While the body inclination angle χ decreases moderately from 34° to 18° with increasing

forward velocities, the calculated downwash angle $\theta_{downwash}$ presents a sharp drop from 85° down to 10° (Fig. 2-12 (*a*)), varying in tandem with all flight velocities. Furthermore, we illustrate the relationship between the body and downwash angles in Fig. 2-12 (*b*) and find a positive correlation between the two angles associated with five forward flight velocities. With a lower body inclination angle of body kinematics, for instance, in fast forward flight (Fig. 2-10 (*ei*), Fig. 2-11 (*fi*)), the induced downwash velocity field tends to be more horizontal. This indicates that the body kinematics may be an additional factor to exert an impact on the wake topology in hawkmoth forward flight.

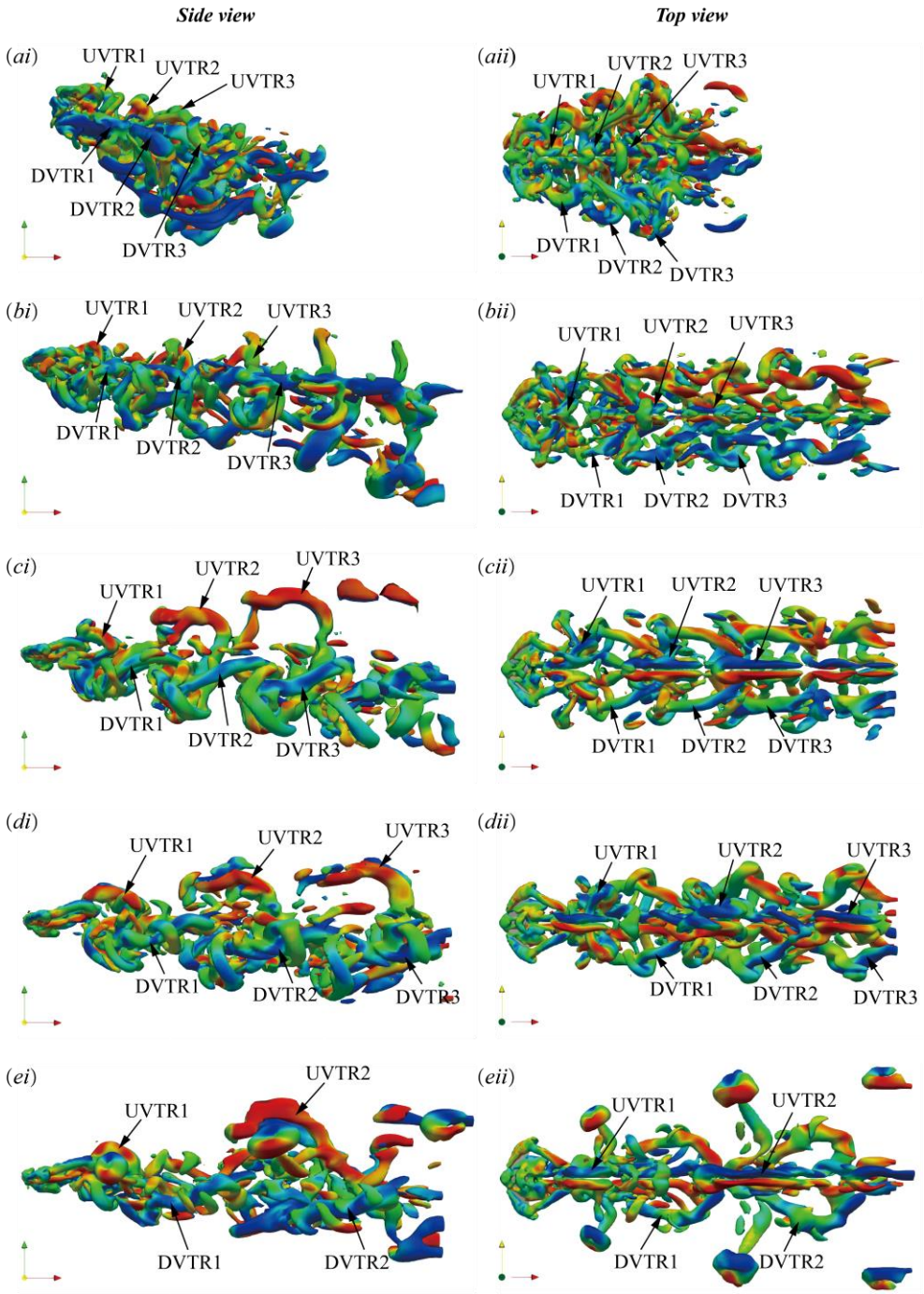

Fig. 2-10 Side- and top-view of wake topology at downstroke of five forward flight velocities: (*a*) 0.9 m/s; (*b*) 2.1 m/s; (*c*) 2.9 m/s; (*d*) 3.8 m/s; (*e*) 5.0 m/s. The iso-surface of *Q*-criterion with a magnitude of 0.015 is utilized to visualize the vorticity and the normalized helicity density is presented for color mapping. The *n*-th downstroke vortex tube rings (DVTR) and upstroke vortex tube rings (UVTR) represent the shed vortices in the *n*-th preceding stroke.

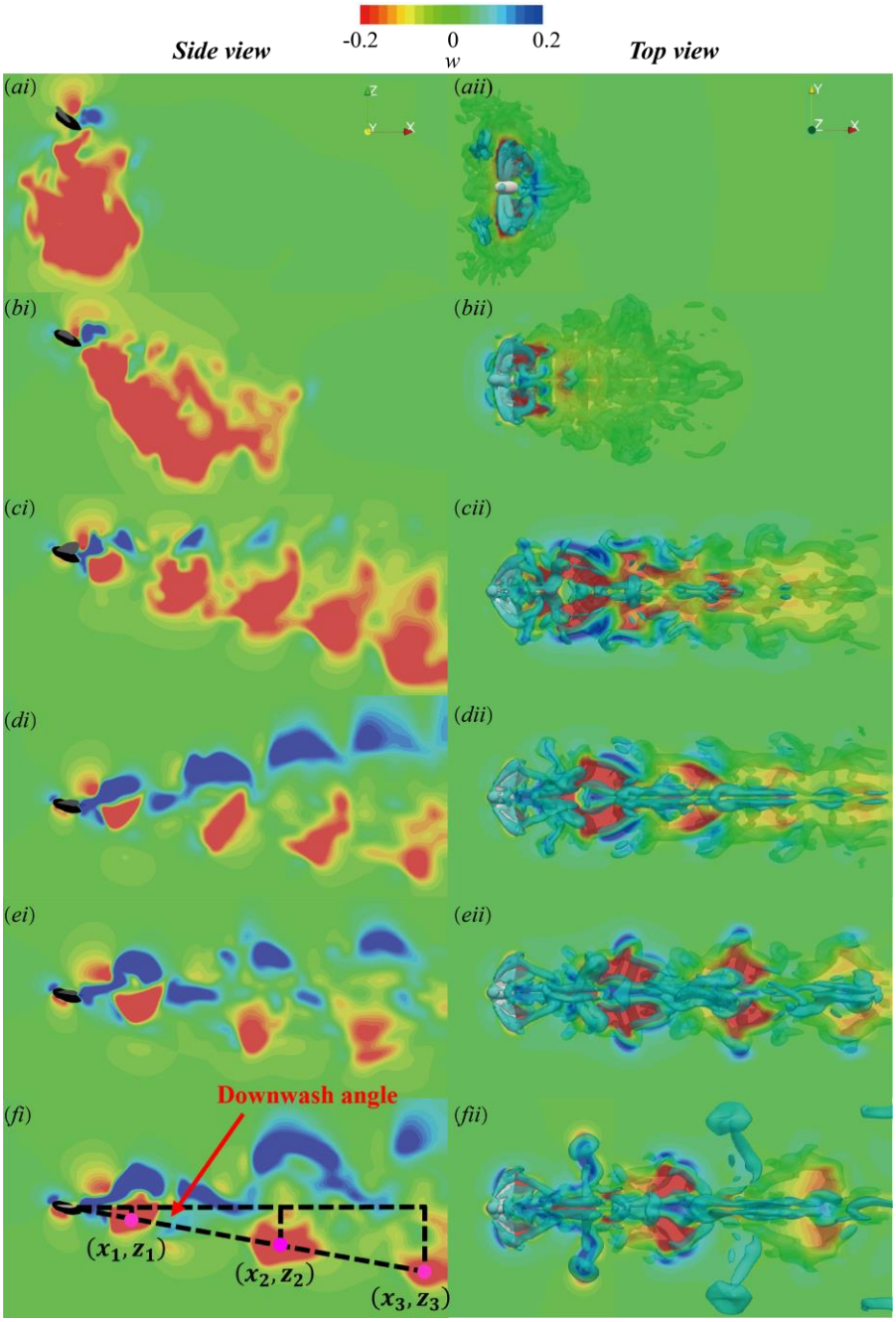

Fig. 2-11 Top-and side-view of the downwash wake topology at downstroke about a hovering (*a*) and forward flight hawkmoth model: (*b*) 0.9 m/s, (*c*) 2.1 m/s, (*d*) 2.9 m/s, (*e*) 3.8 m/s, (*f*) 5.0 m/s. Downwash velocity *w* contours on a cutting plane at the symmetry of insect's body and iso-surface of *Q*-criterion (blue) in a perspective view equals 0.015 are visualized.

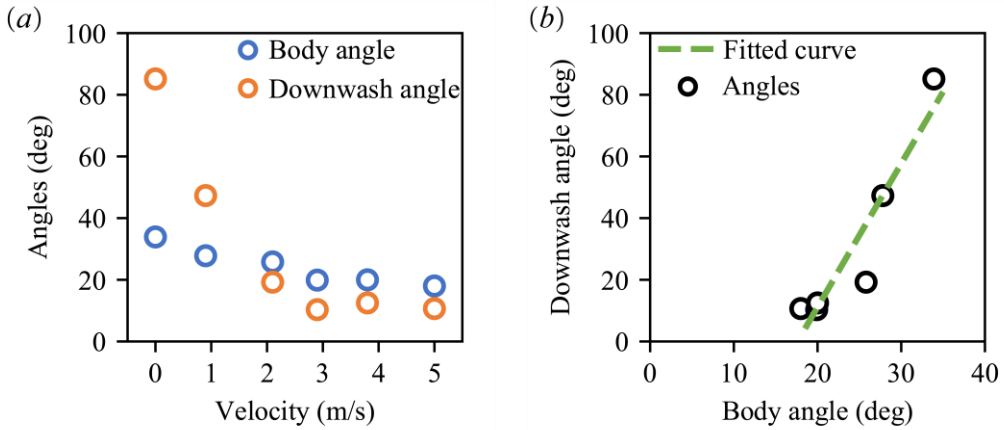

Fig. 2-12 (*a*) Body inclination angles and downwash angles at different flight velocities and (*b*) correlation between the two angles. The dashed line denotes the corresponding fitted curve.

2.6 Aerodynamic force production in forward flight

Aerodynamic force production

Given the overall image of the near-field and far-field flow in various forward flight velocities, we further clarify their correlations with the generation of aerodynamic force and power consumption as well as flight velocity-dependency. The time-course of horizontal and vertical forces in a wing beat stroke are plotted in Fig. 2-13.

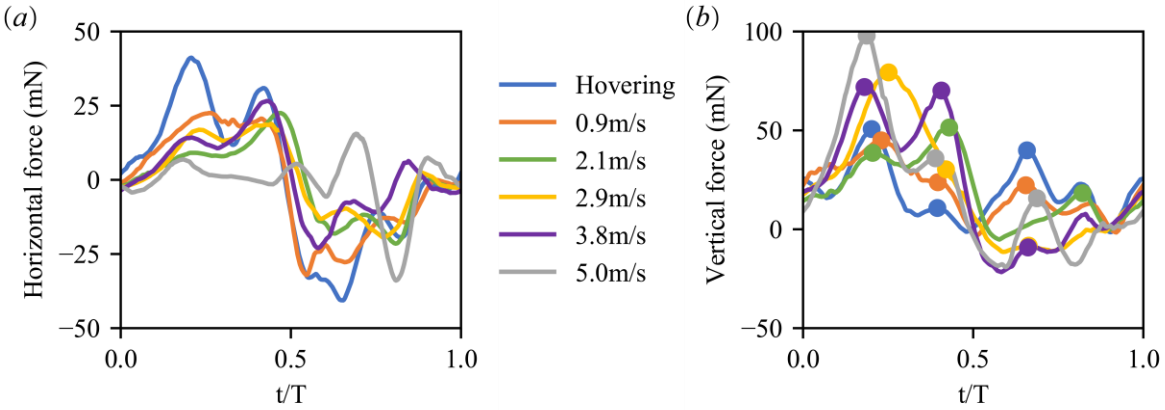

Fig. 2-13 Time-course of horizontal and vertical forces during hovering and forward flights.

According to Table 2-3, the net cycle-averaged horizontal force is approximately zero in all flight velocities, which contributes to a thrust in upstroke but a drag in downstroke. It is noted that the thrust in upstroke and the drag in downstroke decrease progressively as the flight velocity rises from 0.9m/s to 3.8 m/s, well consistent with the observations by Willmott and Ellington [65] that the upstroke contributes to horizontal force in all the flight velocities while decreasing with increasing forward velocity, which is substantially offset by a rising horizontal component produced during downstroke.

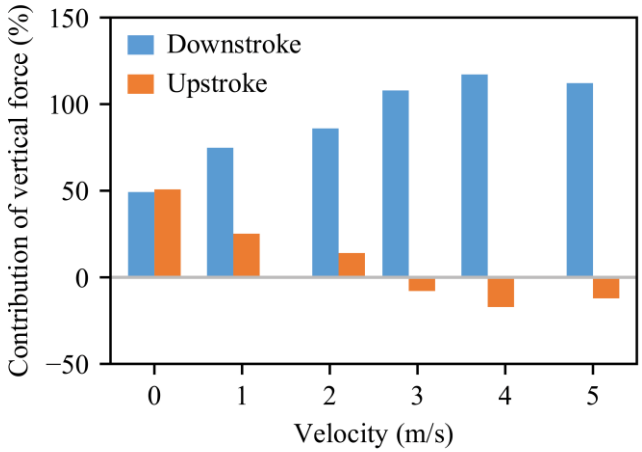

Fig. 2-14 Contribution of upstroke and downstroke to mean vertical forces in hovering and forward flights.

Contribution of upstroke and downstroke to mean vertical forces is further quantified and plotted in Fig. 2-14 for hovering and five forward flights. Obviously, the vertical forces are nearly symmetrical between down-and up-stroke in hovering; in forward flight however, downstroke gives a major contribution to the vertical force production particular at fast forward flight whereas the mean vertical force generated at upstroke declines significantly, even becoming negative at fast flight velocities. The contributions to weight support at downstroke are calculated to be approximately 49% in hovering, and 75% and 86% in forward flights of 0.9 and 2.1 m/s, with a remarkedly increasing downstroke-to-upstroke force ratio of 1.0, 3.0 and 6.1, respectively. Similar trend is also

observed during the downstroke in cicada forward velocity of 2.21m/s, in which a vertical force identical to 79% of the insect weight is produced [40]. This phenomenon is consistent with the features of the wake topologies and downwashes in Fig. 2-10 and Fig. 2-11, that the downstroke plays a crucial role in the production of downward jets while the upward jets induced by upstroke appear particularly in fast forward flight, substantially resulting in the distinguished vertical force generation between down-and up-stroke.

Moreover, a common feature of three peaks is observed in the time courses of vertical forces in all flight modes, at early and late downstrokes, and upstroke (Fig. 2-13), respectively. To investigate the association between LEV and force production, the wing-surface pressure distributions and instantaneous streamlines are also visualized in hovering and five forward flights in Fig. 2-15.

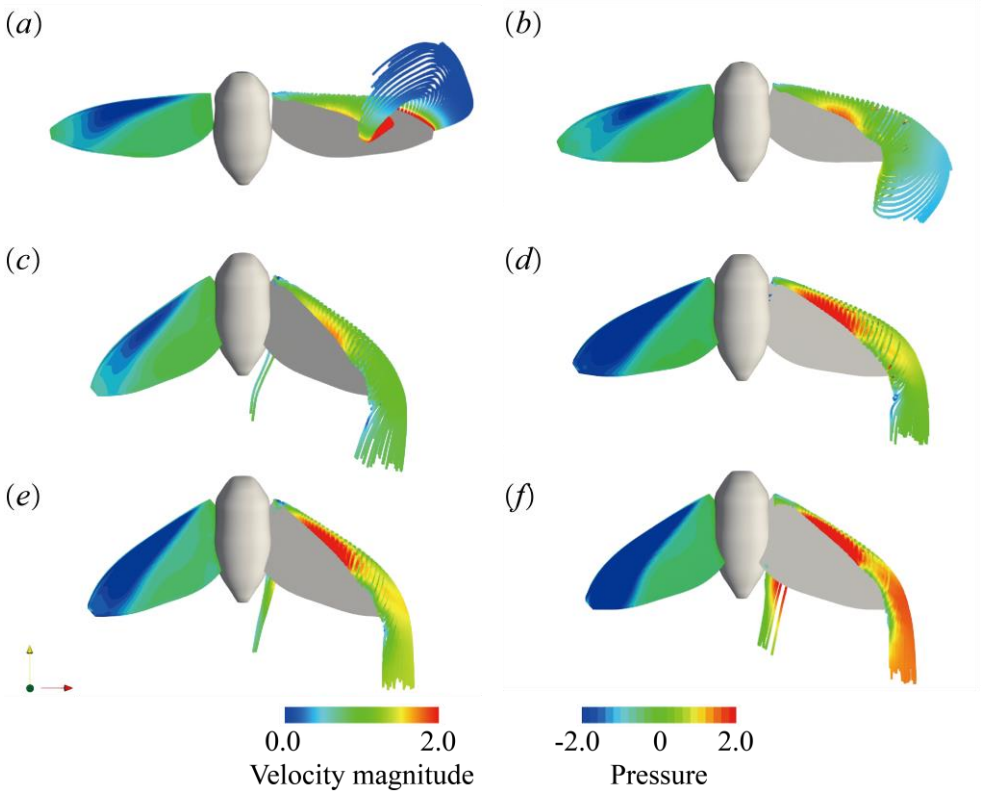

Fig. 2-15 Distributions of wing-surface pressures and instantaneous streamlines during hovering and forward flight at instants (Fig. 2-13 (*b*)) of vertical force peak in first downstroke half (*a*) Hovering; (*b*)

0.9 m/s; (*c*) 2.1 m/s; (*d*) 2.9 m/s; (*e*) 3.8 m/s; (*f*) 5.0 m/s.

The first vertical force peak (Fig. 2-13 (*b*)) is observed at the early downstroke in all flight modes. It essentially corresponds with the initial development of the downstroke LEV (Fig. 2-15), which, as supported by the observations by Willmott *et al* [24], is characterized by a three-dimensional, conical structure with a spanwise core enlarged towards wing tip, becoming more intense in strength but smaller in size with increasing flight velocity. Hence, the negative pressure regions at leading-edge turns out to be larger at fast forward flight velocities (Fig. 2-15), which are responsible for the enhancement of aerodynamic force.

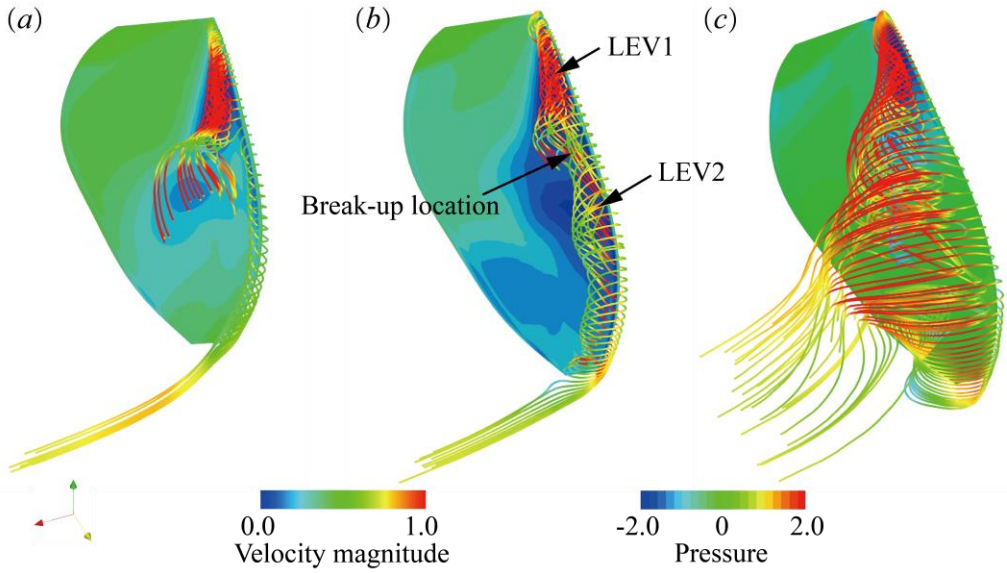

Fig. 2-16 Surface pressure contours and instantaneous streamlines about a flapping wing during downstroke at instants of (*a*) t/T = 0.32, (*b*) t/T = 0.40, corresponding to the 2nd vertical force peak in Fig. 2-13 (*b*), and (*c*) t/T = 0.48 at forward flight velocity of 3.8 m/s.

Before reaching the 2nd peak of the vertical force at late downstroke, the LEV core shows a break-up at approximately 70% of the length, and the tip aera separates early at the second downstroke half in hovering [10], which is also detected in various forward flights with different break-up locations. Fig. 2-16 shows how the LEV aerodynamics vary

during the downstroke through visualizing surface pressure contours and instantaneous streamlines. At this stage, a new negative pressure region is visible between the break-up position and the wing tip, which eventually diminishes rapidly at the end of downstroke. This phenomenon is explicable in terms of dual leading-edge vortices (LEV1 and LEV2) presented at the same time and connected with each other (see Fig. 2-16 (*b*)). Later at the end of downstroke, due to the wing deceleration, LEV2 is pushed off from leading edge [10] accompanying with shedding LEV1, which results in appearance and vanishment of the 2nd force peak.

More importantly, the break-up location vs flight velocity in Fig. 2-17 (*a*) shows a trend to decline from 75% down to 50% of the wing length while moving towards the wing base at fast flight velocities. This causes a decrease in transient vertical force at the 2nd peak, displaying a monotonically linear decrease (Fig. 2-17 (*b*)) with increasing flight velocities. Contribution of the LEVs to the 2^{nd} peak of vertical forces are illustrated in Fig. 2-17 (*c*) through the visualization of pressure contours and resultant forces on wing surfaces, demonstrating that the combination of LEV1 and LEV2 give an optimal contribution to the 2nd force peak at flight velocity of 3.8 m/s (Fig. 2-13 (*b*)). Thus, the break-up location and hence the combination of LEV1 and LEV2 play a crucial role in generation of vertical force during downstroke in various flights.

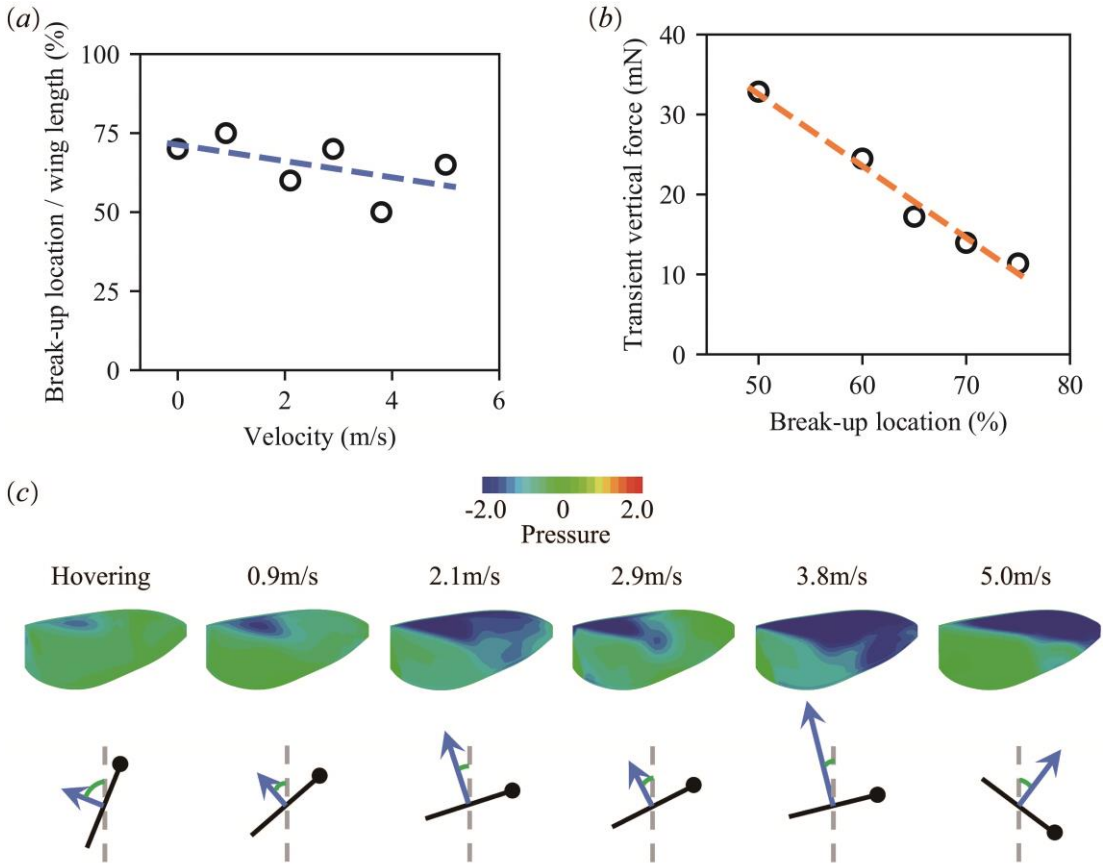

Fig. 2-17 Break-up location vs flight velocity (*a*) and its correlation with transient vertical force in a flapping hawkmoth wing (*b*), as well as pressure contours and resultant forces on wing surfaces in hovering and five forward flights at the instant (Fig. 2-13 (*b*)) of the 2nd vertical force peak (*c*).

The 3rd vertical force peak is observed at early half of upstroke corresponding to the upstroke LEV (Fig. 2-9 and Fig. 2-10), which is also found in Willmott *et al* [24] that during supination, the LEV moves rearward shedding from trailing edge over the upper wing. The vertical force shows a decrease with higher flight velocity probably due to the reduced feathering amplitude in fast forward flight (Fig. 2-5). The existence of negative vertical force peak at the 2nd half stroke is attributed to the first shed vortex ring which lies near the wing plane, resulting in downwash velocity peak [97]. During the rotational phase when the wing reverses, the upstroke LEV grows to be intense in hovering and slow forward flights whereas it turns out to be weakened and even decay in the fast forward

flight velocities greater than 2.1 m/s. This indicates that the asymmetric feature in vortex dynamics and hence aerodynamic force exists at down-and up-stroke, which turns out to be more obvious with increasing forward flight velocity as also observed in Willmott and Ellington [65].

The correlations between the vortex dynamics, wake topology and aerodynamic force thus demonstrate that the LEV-based mechanism is a universal mechanism [98], creating most of the aerodynamic forces in various forward flights.

Chapter 3 Flapping energetics in insect forward flight

3.1 Introduction

In recent years, the bio-fluid flapping energetics in biological flights has been widely studied in terms of unveiling the energy consumption and power efficiency in hovering and forward flight of insects and birds. Experimental and computational analysis [5, 18, 65] based on the high-speed videography, simplified theoretical model and computational fluid dynamics (CFD) have shown a variety of energetic mechanisms correlated with morphology, kinematics and flapping aerodynamics [5, 18, 40, 64]. However, since the flying animals spend most of their lifetime for long-distance migration, hunting and territory, an insight into the central question about how insects achieve the optimal energetic expenditure and flight efficiency over a broad range of flight velocity remains yet poorly explored.

Significant features of power consumption in hovering and forward flights of various insects and birds have been reported by several experimental and numerical studies. Various shapes of power curves against flight velocities have been found in flapping insects [5, 65-67] as well as flying birds [53, 68-71]. Previous studies are mostly conducted with a focus on a specific flying velocity or with some simplified theoretical model based on observations. Therefore, an overall understanding of the forward flight energetics in various flight velocities needs to be explored through unraveling its correlations with the inertial and aerodynamic power components, the total power cost as well as the mechanical efficiency.

To study the bio-fluid energetic expenditure, two typical dimensionless indices Froude mechanical efficiency and Cost of Transport have been proposed. According to Templin

[77] and Shyy *et al* [4], the best cruising speed is considered corresponding to the minimum *CoT*, which is generally higher than that with minimum required flight power. Simulations on forward flight of hawkmoth indicates that long-distance migration may benefit from higher speed, as the energy cost per unit distance decreases monotonically with advance ratio [43]. More importantly, the computational and experimental studies on undulatory swimming demonstrated that fish could regulate tail-beat amplitude and frequency to minimize CoT rather than Froude mechanical efficiency [74, 76]. Since the previous studies relating to bio-flights were mostly focusing on one single energetic indices, the flight-velocity dependency of Froude efficiency and Cost of Transport, as well as the identification for the optimal cruising speed and energetic efficiency for various species in bio-flights remains still unexplored.

In this chapter, we aim to unravel the underlying mechanisms related with flapping energetics in forward flight of four typical insects, covering broad range of flight velocities. We introduce a versatile and high-fidelity CFD model integrating the realistic morphology and kinematics, which enables precise prediction of the aerodynamic forces and powers for forward flight of various flapping insects. A systematic analysis is conducted on the flight-velocity dependency of inertial, aerodynamic power components and total power cost, as well as the correlations with LEV dynamics and aerodynamic performance. Further investigations into two energetic indices Cost of Transport and Froude efficiency allow us to uncover the optimal cruising speed and energetic efficiency in forward flights of various flapping insects.

3.2 Morphological and kinematic models

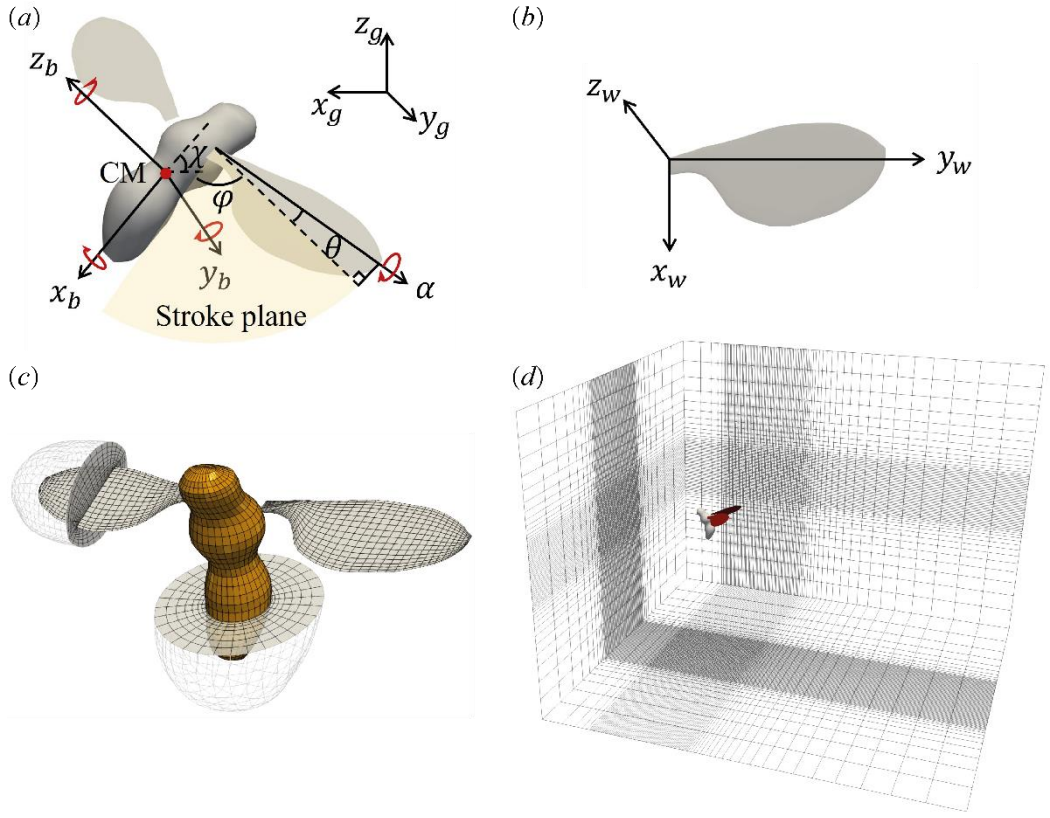

Fig. 3-1 (*a*) Schematic of coordinate systems and wing-body kinematic parameters of fruit fly model: a global (x_g, y_g, z_g) coordinate system, a body-fixed (x_b, y_b, z_b) coordinate systems. (*b*) Definition of a wing-fixed (x_w, y_w, z_w) coordinate system. (*c*) Integrated overset-grid and multi-blocked system of a fruit fly model including a body block and two wing blocks as well as (*d*) a background grid block.

We construct the morphological models for four insects and mimic the realistic experimental kinematics, which cover a broad range of flight velocities for each species, including hawkmoth (*Manduca Sexta*), bumblebee (*Bombus terrestris*), wasp (*Anagrus*), and fruit fly (*Drosophila melanogaster*). Detailed parameters of four insects' models are summarized in Table 3-1. The realistic wing-body kinematic model involving flapping wings and moving body is capable of modeling flapping flights from hovering to various forward speeds [9]. Moreover, the reference length L_{ref} is defined as mean chord length c_m, for hovering flight U_{ref} is referred as the mean wing angular velocity $2\emptyset fR$, where f is the flapping frequency and $\emptyset$ is the flapping amplitude. In hovering flight Reynolds

number is determined as $Re_h = \frac{U_{ref}L_{ref}}{\upsilon} = \frac{2\emptyset fRc_m}{\upsilon}$, and the air kinematic viscosity υ equals $1.5 \times 10^{-5} m^2 s^{-1}$. For forward flight, U_{ref} will be the forward flight speed of insects V_f and then Reynolds number $Re_f = \frac{U_{ref}L_{ref}}{\upsilon} = \frac{V_f c_m}{\upsilon}$. A wide *Re* range is listed in Table 3-1 from $O(10^1)$ for tiny wasps, to $O(10^4)$ for hawkmoths, owing to decreasing flapping frequency and the sharp increasing insect size [11].

Table 3-1 Morphological parameters and Reynolds numbers for four flapping insects. Here listed value of Re_h denotes the Reynolds number in hovering flight while Re_f denotes the Reynolds number in fast forward flight.

Species	m_b(mg)	m_w(mg)	c_m(mm)	R (mm)	Re_h	Re_f
Wasp	0.0134	0.00044	0.1763	0.6	11	6
Fruit fly	1.13	0.0068	0.78	2.39	136	104
Bumblebe	175	0.91	4.0244	13.2	1723	1207
Hawkmot	1995	89.58	18.6	50.64	6615	6200

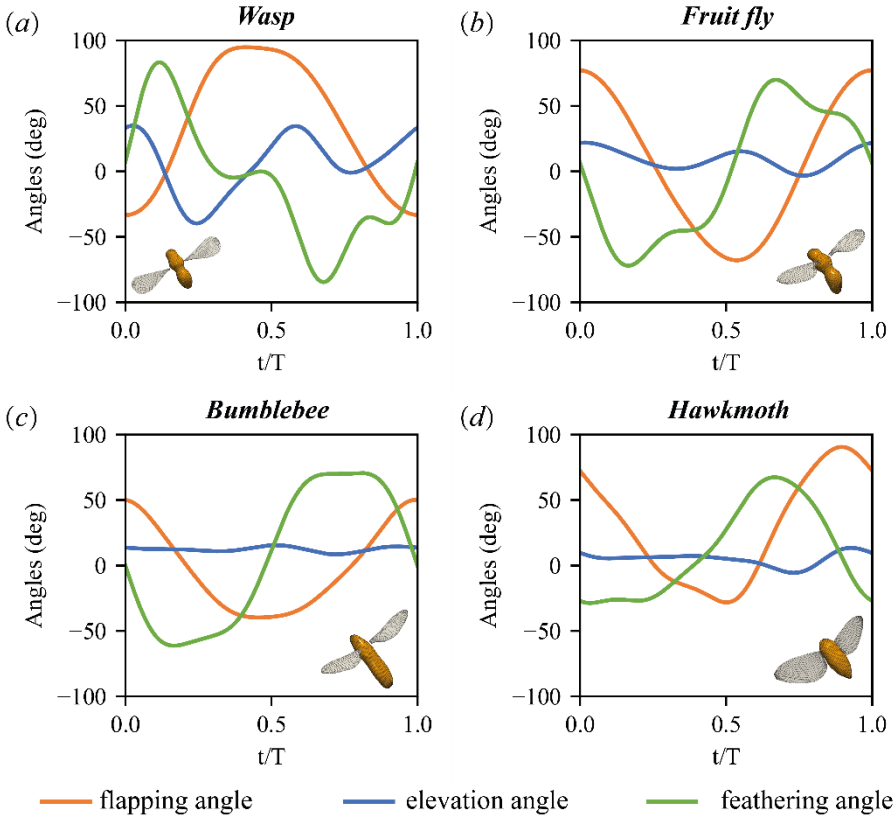

Fig. 3-2 Morphological models and hovering wing kinematics for four insects (*a*) wasp; (*b*) fruit fly; (*c*)

bumblebee; (*d*) hawkmoth.

Wasp (Anagrus)

A wing-body morphological model of a tiny wasp, *Anagrus Haliday* as plotted in Fig. 3-2 (*a*) has a morphology of membrane wing R = 0.6 mm and c_m = 0.1763 mm with the realistic bristled wing mass m_w of 0.00044 mg [99]. The four-winged wasp is constructed approximately with a pair of two wings which is thought to be reasonable with nearly analogous the fore wing and hind wing movement [11, 48]. The wing-body grid system of the tiny wasp involving four-blocked overset grids (body grid: 33×33×9, right-wing and left-wing grid: 33×35×13). The experimental observations by Cheng and Sun [46, 100] are employed for kinematic models with the three flapping angles in various flight velocities. Table 3-2 lists the velocity-dependent flapping frequency f, stroke amplitude Φ, stroke plane angle β_{SP} and body angle χ in various flight velocities, and the low Reynolds number for tiny wasp turns out to be on the order of 10^0~10^1.

Table 3-2 Wing-body kinematic parameters of wasp, *Anagrus* in hovering and forward flights.

Speed	f (Hz)	Φ (Deg.)	χ (Deg.)	β_{SP}(Deg.
Hovering	349	140	86.0	-5.3
0.12	336	141	75.0	5.7
0.25	328	137.3	58.0	22.7
0.33	354	140	42.0	35.9
0.50	354	145	20.6	57.0

Fruit fly (Drosophila melanogaster)

The fruit fly morphological model, *Drosophila melanogaster* is built as Fig. 3-2 (*b*) with grids. The insect's body mass m_b is 1.13 mg and the wing mass m_w is 0.0068 mg for fruit fly, which has mean chord length c_m of 0.78 mm and wing length R of 2.39 mm [11]. Four-blocked overset grids include the body grid: 33×33×9 as well as right-wing and

left-wing grid: 33×35×13. The kinematic models are based on the observation and simulation data [33, 59, 101], where the three flapping angles in various flight velocities are obtained. A list of body angle χ, stroke plane angle β_{SP}, stroke amplitude Φ, and flapping frequency f in various flight velocities are also given in Table 3-3, which show fluctuations with velocity-dependency and the Reynolds number for fruit fly is calculated to be ranging from 10^1 to 10^2.

Table 3-3 Wing-body kinematic parameters of fruit fly, *Drosophila melanogaster* in hovering and various forward flights

Speed	f (Hz)	Φ (Deg.)	χ (Deg.)	β_{SP}(Deg.
Hovering	216	135	0.0	68.0
0.5	208	129	18.0	50.0
1.0	210	131	31.0	37.0
1.5	232	145	46.0	22.0
2.0	240	165	58.0	10.0
2.5	240	160	70.0	-2.0

Bumblebee (Bombus terrestris)

A bumblebee morphological model, *Bombus terrestris* is constructed with mean chord length c_m of approximately 4.0 mm and wing length R of 13.2 mm and. The body mass of bumblebee model m_b is 175 mg and the wing mass m_w is 0.91 mg [66]. As illustrated in Fig. 3-2 (*c*), the wing-body grid system is built with four blocks (body grid: 37×39×19, right-wing and left-wing grid: 37×33×11). The experimental and simulation data [34, 66, 102] are employed for kinematic models of bumblebee. Table 3-4 provides a list of parameters in various flight velocities with the Reynolds number varies from 10^2 to 10^3.

Table 3-4 Wing-body kinematic parameters of bumblebee, *Bombus terrestris* in hovering and various forward flights

Speed	f (Hz)	Φ (Deg.)	χ (Deg.)	β_{SP}(Deg.
Hovering	155	116.0	47.0	6.0

1.0	145	112.0	31.7	16.0
2.5	152	125.0	24.7	28.0
3.5	148	114.0	19.0	35.5
4.5	144	103.0	12.9	43.0
5.5	148	108.0	6.8	50.5

Hawkmoth (Manduca Sexta)

A realistic hawkmoth morphology is built, *Manduca Sexta*, which has mean chord length c_m of 18.6 mm, a wing length R of 50.64 mm and a body length L of 41.85 mm. The body mass m_b is 1,995 mg and the wing mass m_w is 89.6 mg [18]. The wing-body grid system for hawkmoth contains four blocks (right-wing and left-wing grid: 39×65×22, body grid: 37×39×9,), which is illustrated in Fig. 3-2 (*d*). Kinematic models are according to the experimental observations by Willmott and Ellington [18], including three angles in various flight velocities. A list of flapping frequency f (24.8~26.1 Hz), body angle χ, stroke plane angle β_{SP}, and stroke amplitude Φ in various flight velocities are also given in Table 3-5, which are all velocity-dependent, hence resulting in the Reynolds number for hawkmoth fluctuates in an order of 10^3~10^4 from 1000 to 6000 approximately.

Table 3-5 Wing-body kinematic parameters of hawkmoth, *Manduca Sexta* in hovering and various forward flights from the experimental measurements by Willmott and Ellington [18].

Speed	f (Hz)	Φ (Deg.)	χ (Deg.)	β_{SP}(Deg.
hovering	25.4	113.2	33.9	23.4
0.9	25.6	105.5	27.8	23.3
2.1	24.8	99.5	25.8	37.6
2.9	26.1	97.1	19.9	44.4
3.8	24.8	102.7	20.0	52.7
5.0	25.0	103.9	18.0	56.4

An extensive study is conducted on the grid dependency of the fruit fly model, which contains four-blocked overset grids. Verification of the self-consistency were performed

and confirmed through comparisons (Fig. 3-3) of time-varying aerodynamic horizontal and vertical forces as well as the pitch torque in hovering flight among different cases: *Case 1*, coarse mesh (body grid: 27×27×7, wing grid: 27×29×11, background grid: 77×69×57) time step dt = 0.0005T; *Case 2*, medium mesh (body grid: 33×33×9, wing grid: 33×35×13, background grid: 93×85×69) time step dt = 0.0005T; *Case 3*, fine mesh (body grid: 39×39×11, wing grid: 39×41×15, background grid: 111×101×85) time step dt = 0.0005T. Our results obviously show marginal discrepancy among different cases.

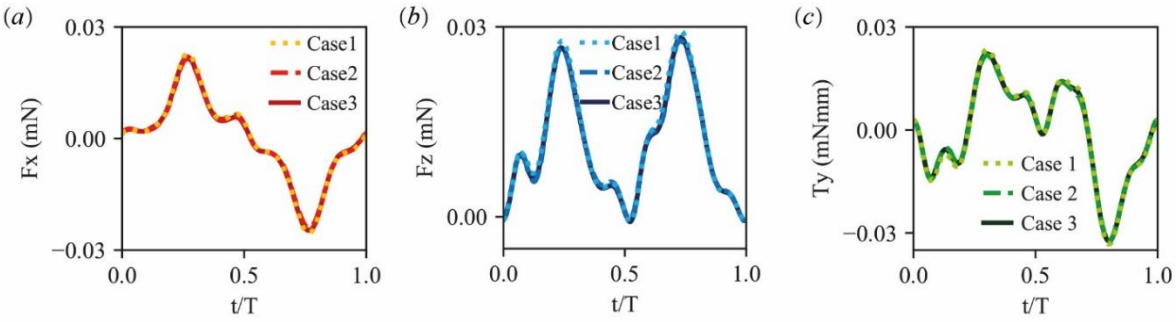

Fig. 3-3 Grid density effect on time-course of forces and torque in a wing-beat stroke cycle of hovering flight in three cases. (*a*) Horizontal force F_x; (*b*) Vertical force F_z; (*c*) Pitch torque T_y.

Considering obtaining precise estimation of energetics in balanced condition, we further employed a method to modify the wing kinematics with intention of achieving trimmed flights of four insect models in various flight velocities. A genetic algorithm (GA) with covariance matrix adaptation based on derandomized evolution strategy (CMA-ES) [93, 94] is employed for finely tuning the wing kinematics, embedded with a CFD data-driven aerodynamic model (CDAM) by Cai *et al* [92]. Flow chart of the approach to determine trimmed flights is illustrated in detail in Fig. 2-4. Satisfying three conditions for trimmed flights, the resultant wing kinematics in the various trimmed flights are achieved for four insect models.

3.3 Evaluation of energetic expenditure

Here we define the aerodynamic and inertial powers as

$$P_{aero} = \sum_i (\boldsymbol{F}_{w,i} \cdot \boldsymbol{v}_{w,i} + \boldsymbol{F}_{b,i} \cdot \boldsymbol{v}_{b,i}) . \quad (3-1)$$

$$P_{iner} = \sum_i (m_{w,i} \boldsymbol{a}_{w,i} \cdot \boldsymbol{v}_{w,i}) , \quad (3-2)$$

where $F_{w,i}$ and $F_{b,i}$ represent the aerodynamic forces acting upon the wings and body respectively, and $v_{w,i}$ and $v_{b,i}$ are the wing velocities and body forward velocities in the *i*-th cell. The inertial power can be considered as the scalar products of the wing inertial forces and the velocity [9], where $m_{w,i}$ is the mass of the cell on the wing model, $a_{w,i}$ and $v_{w,i}$ are respectively the computed wing accelerations and velocities in the *i*-th center. Thus, we estimated the power consumption as total mechanical power, which is described as

$$P_{toto} = P_{aero} + P_{iner} , \quad (3-3)$$

and treat the negative part to be zero throughout the wing beat with no elastic storage [64] when calculating the time-averaged values. The total mechanical body-mass-specific power is further employed for analysis and comparison among a variety of species by dividing total mechanical power with the body mass of insects m_b,

$$P^*_{toto} = P_{toto} / m_b . \quad (3-4)$$

The evaluation of energetic expenditure is based on two typical indices, the dimensionless Froude mechanical efficiency η_{Fr} and cost of transport *CoT*, which have been analyzed in fish swimming [74] and further extended to insect flapping flight,

$$\eta_{Fr} = \frac{\bar{T} \cdot V_f}{\bar{P}_{toto}}, \quad (3-5)$$

$$CoT = \frac{\bar{P}_{toto}}{V_f \cdot m_b} . \quad (3-6)$$

Here, $\bar{T}$ denotes the cycle-averaged thrust defined as the sum of positive aerodynamic

forces components on each surface element relative to the direction of the path of motion. V_f and $\bar{P}_{toto}$ are the forward flight velocity and time-averaged total mechanical power, respectively. Similar to fish swimming [74], the two indices are different in optimizing aerodynamic performance for insect flapping flight and may reach the peak at certain forward flight velocities, respectively.

3.4 Power consumption in various flight velocities

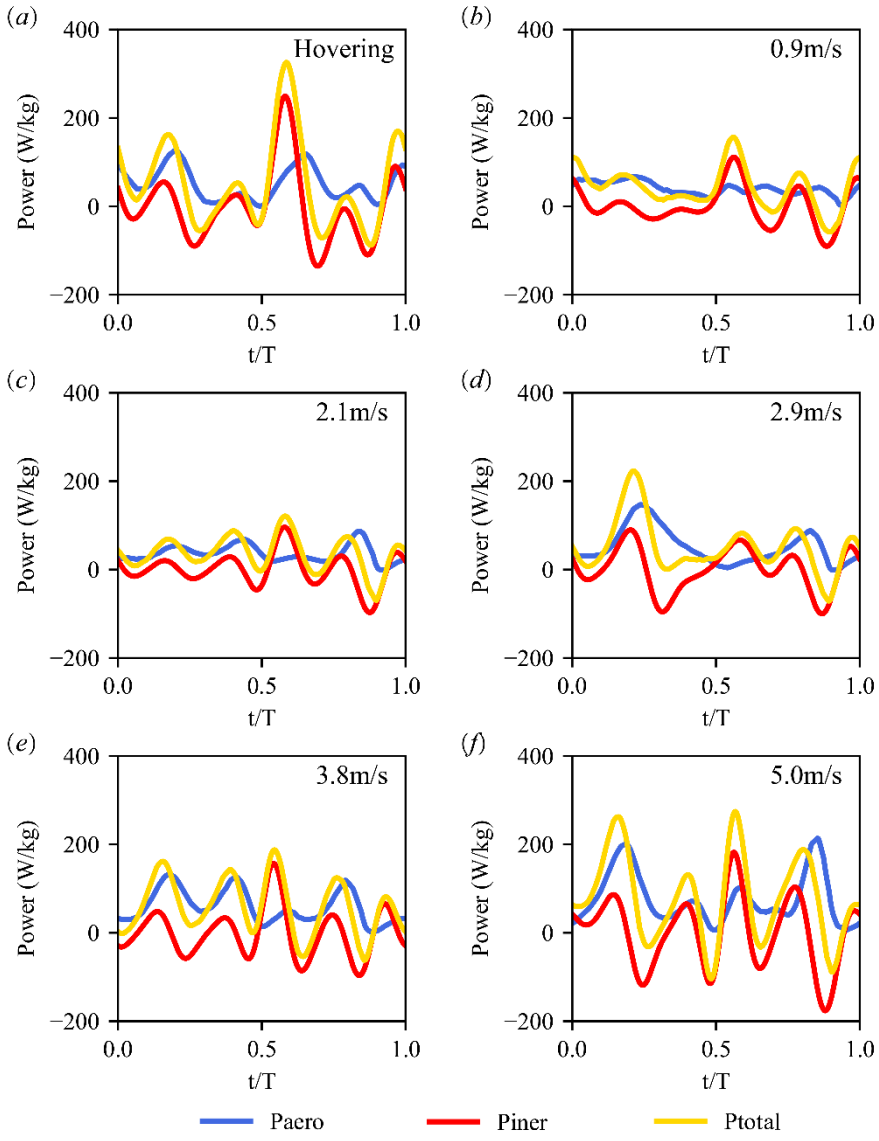

Fig. 3-4 Time-course of three body-mass-specific power components of hawkmoth: aerodynamic power P_{aero}, inertial power P_{iner}, and total mechanical power P_{total}.

We evaluate herein the energetics in terms of power consumption for various forward-flight velocities. The inertial, aerodynamic, and total mechanical powers of hawkmoth are defined by the instantaneous forces and the wing and body velocities, which are calculated in a body-mass-specific manner and plotted in Fig. 3-4. P_{aero} is the power required to overcome air drag (Eq. 3-1), which remains positive and peaks in phase with the high force production. P_{iner} is the power for accelerating the wing (Eq. 3-2), which alternates between positive and negative, increasing during the phase of wing acceleration. The total mechanical power (Eq. 3-3), which becomes negative during the wing decelerating [9]. This commonly occurs during hovering and during forward flight at the five velocities (Fig. 3-4).

Three time-varying body-mass-specific powers produce remarkedly larger amplitudes during hovering and 5.0 m/s of hawkmoth at (Fig. 3-4 (*a*) and (*f*)). Note that the amplitude of inertial power slightly exceeds the aerodynamic power during hovering and slow forward flight. The wing accelerating cost is as high as the total aerodynamic consumption or much higher in low flight speeds [65]. In contrast, at the top 5.0 m/s, the aerodynamic power in a complete wing stroke consumes much more power than the inertial power. This indicates that the power consumption is dominated by inertia during hovering and slow forward flight but is dominated by aerodynamics in fast forward flight because of the trade-off between the wing-acceleration-based inertial power cost and the aerodynamic power requirement.

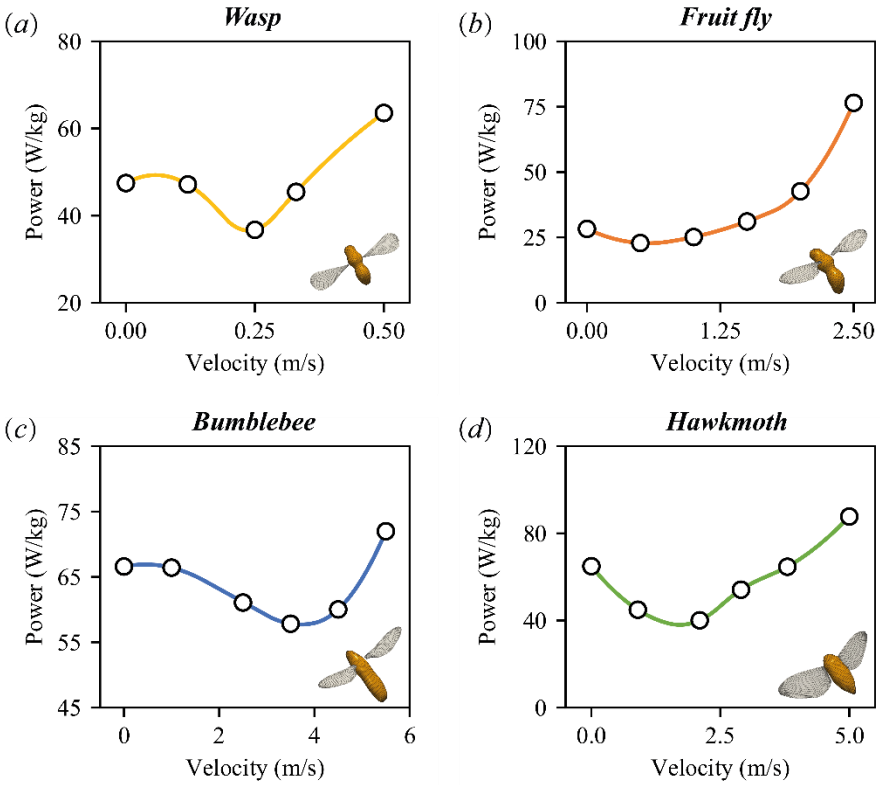

Fig. 3-5 Time-averaged body-mass-specific total positive mechanical powers in hovering and various forward flight velocities for four insect models. (*a*) Wasp; (*b*) Fruit fly; (*c*) Bumblebee; (*d*) Hawkmoth.

The evaluation of energetics in various insect flapping flight is based on the power consumption for four species in a broad range of flight velocities. Defined by the sum of aerodynamic powers P_{aero} and inertial powers P_{iner}, the total mechanical powers are calculated in a body-mass-specific manner P^*_{toto} (Eq. 3-4). The correlation between power cost and flight velocity is investigated in terms of the time-averaged, body-mass-specific, total positive mechanical power for four insects as plotted in Fig. 3-5. The *J*-shaped power curves are commonly observed for all flapping insects covering hovering and a broad range of forward flight velocities (Fig. 3-5). Different shapes of the power curve have been reported in previous studies, as the *U*-shaped curves for bumblebee [66], hawkmoth [5, 65, 67] and birds of cockatiels, doves and magpies [69, 70] as well as the *J*-shaped curve for hummingbirds [68, 69]. As plotted in Fig. 3-5, relatively higher

power consumption occurs in hovering and fast forward flights, which is significantly expensive at the top velocity for all four insects of wasp (63.6 W/kg), fruit fly (76.5 W/kg), bumblebee (72.0 W/kg) and hawkmoth (87.7 W/kg). For the hawk moth, the power requirements increase steeply as the moth approaches the top velocity, which may be attributed to the intense LEVs and downwashes, as depicted in Fig. 2-10 (*e*) and 2-11 (*f*). As observed by Willmott and Ellington [65], a further increase in forward flight velocity over 5 m/s is likely constrained by some limitations in the essential flying-muscle system, which may not produce the required total mechanical power. More importantly, it is also observed that the minimum mechanical powers exist around the intermediate flight velocity of 0.25 m/s for wasp (36.7 W/kg), 0.5 m/s for fruit fly (22.8 W/kg), 3.5 m/s for bumblebee (57.8 W/kg) and 2.1 m/s for hawkmoth (40.1 W/kg). The relatively low power consumption at intermediate flight velocities can be ascribed to the effective utilization on wing drag for generating lift [43], which provides the insects an energetic and efficient forward-flight zone.

3.5 Mechanical efficiency in various flight velocities

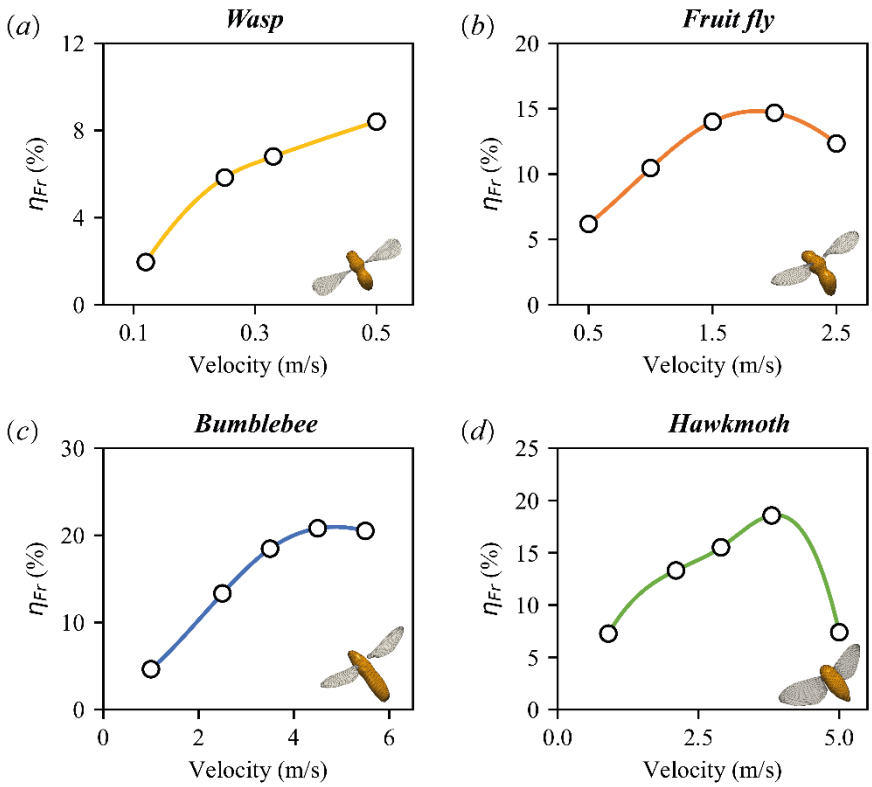

Fig. 3-6 Froude mechanical efficiency (η_{Fr}) in various forward flight velocities for four insect models. (*a*) Wasp; (*b*) Fruit fly; (*c*) Bumblebee; (*d*) Hawkmoth.

One of the energetic expenditure indices Froude mechanical efficiency (η_{Fr}) determined in Eq. 3-5 offers a different path with that of *CoT* for optimizing the energetic efficiency through maximizing the useful power output to power expense in the air [74]. The Froude mechanical efficiency at various forward flight velocities for four flapping insects are calculated and plotted in Fig. 3-6. It can be noticed that the η_{Fr} curve against a broad range of flight velocities shows the lowest value in slow forward flight, and it rises gradually with increasing flight velocity with a remarkable peak at fast forward flights. Maximum η_{Fr} can also be achieved at specific forward flight velocities, such as, 0.5m/s for wasp, 2.0 m/s for fruit fly, 4.5 m/s for bumblebee and 3.8 m/s for hawkmoth, which is

close to the certain velocities corresponding to the minimum *CoT* for four insect models. What's different is that the maximum Froude mechanical efficiency η_{Fr} in various flight velocities is to maximize the utilization of the input power expenditure in the air with the intention of achieving the highest effective output for forward flight.

3.6 Minimum cost of transport at certain flight speed

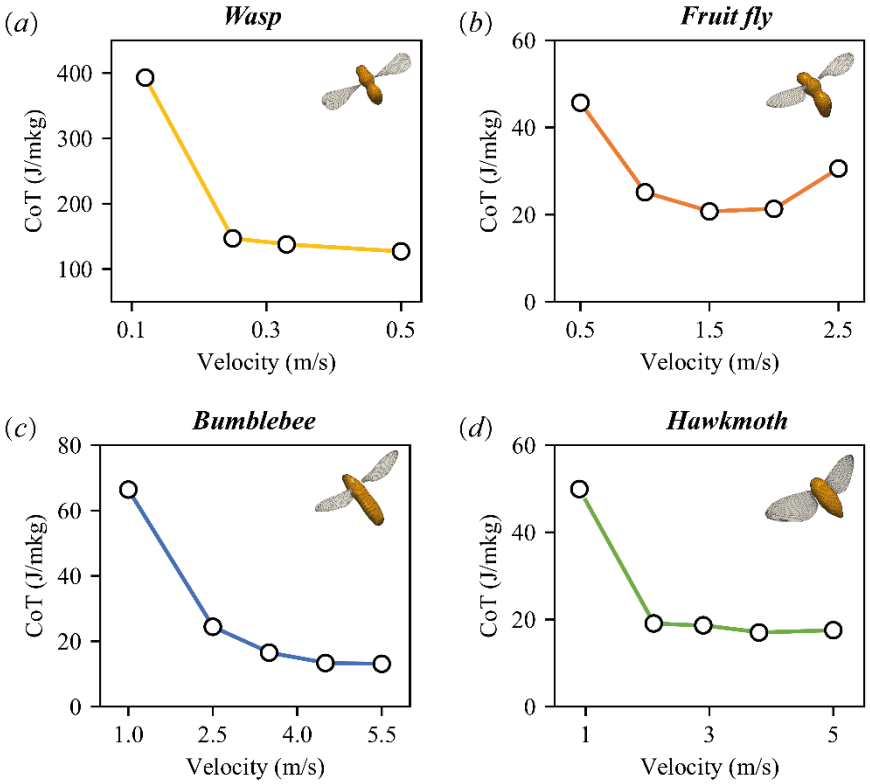

Fig. 3-7 Cost of Transport (*CoT*) in various forward flight velocities for four insect models. (*a*) Wasp; (*b*) Fruit fly; (*c*) Bumblebee; (*d*) Hawkmoth.

The energetic expenditure indices cost of transport (*CoT*) defined in Eq. 3-6 provides a path for optimizing the energetic efficiency through minimizing the input power needed at a certain speed to move a certain mass [74]. We calculate the *CoT* at various forward flight velocities for four flapping insects. As depicted in Fig. 3-7, the *CoT* curves against a broad

range of flight velocities show similar shapes among different species, which appear the highest value in slow forward flight while prone to be lower and even flat in intermediate and fast forward flights. Butler [69] illustrated the *CoT* for several flying insects as a function of body mass and demonstrated that *CoT* decreases from 10^2 to $10^1\ J/m\cdot kg$ as the mass of the flying animals increases from 10^{-3} to $10^0\ g$, which is partially consistent with the current results as the smallest wasp appears the highest magnitude of *CoT*. The *CoT* turns out to reach the minimum at certain forward flight velocities, such as, 0.33~0.5 m/s for wasp, 1.5~2.0 m/s for fruit fly, 4.5~5.5 m/s for bumblebee and 3.8~5.0 m/s for hawkmoth. This indicates when insects flying around certain flight velocity, they may be able to achieve the lowest input power consumption for moving a given mass.

To further demonstrate this conjecture quantitatively, we first try to derive a theoretical scaling law to correlate the cost of transport and the flight velocity. The power consumption in stable forward flight can be divided into horizontal and vertical superposition, such as $P = P_v + P_h$, where the reference vertical powers P_v are defined as the product of reference lift forces L and the reference wing tip velocity V_w while the reference horizontal powers P_h is predicted by product of reference drag D and forward moving speed V_f, such as

$$P = P_v + P_h = L \cdot V_w + D \cdot V_f. \qquad (3-7)$$

As the reference lift force L can be replaced by $m_b g$ in stable forward flight, the reference drag force D is represented by $\frac{1}{2}\rho_{air} C_D {V_f}^2 S$ and the reference wing tip velocity V_w equals to $2\emptyset fR$, Eq. 3-7 can be further written as $P = m_b g \cdot 2\emptyset fR + \frac{1}{2}\rho_{air} C_D {V_f}^2 S \cdot V_f$. Since the surface aera S can be replaced dimensionally by $\frac{m_b}{\rho_{insect} \cdot l}$, the velocity-dependent body-mass specific power consumption is finally represented as

$$P^* = \frac{P}{m_b} = c_1 \emptyset fR + \frac{c_2}{l} {V_f}^3 = C_1 + C_2 \cdot {V_f}^3, \qquad (3-8)$$

where c_1,c_2 are constants, $C_1 = c_1 \emptyset f R$ and $C_2 = \frac{c_2}{l}$, m_b is the body mass, R is the wing length, f is the flapping frequency, $\emptyset$ is the flapping amplitude, l is the body length and V_f denotes the forward flight velocity for four insects. We further verify the theoretical correlation through numerical fitting on the power-velocity curve. As shown in Table 3-6, calculated by $c_1 = \frac{C_1}{\emptyset f R}$ and $c_2 = C_2 \cdot l$, theoretical coefficients c_1,c_2 for four insect models turn out to share close magnitude among species, which indicates that the velocity-dependency on power consumption is universal for four typical insects with various Reynolds numbers.

Table 3-6 Numerical fitting results of the theoretical coefficients

Species	C_1	C_2	c_1	c_2
Wasp	47.39	60.64	9.04×10^1	3.64
Fruit fly	22.12	3.168	1.58×10^1	8.44
Bumblebee	63.15	0.1552	1.85×10^1	2.89
Hawkmoth	43.71	0.3499	1.90×10^1	1.46

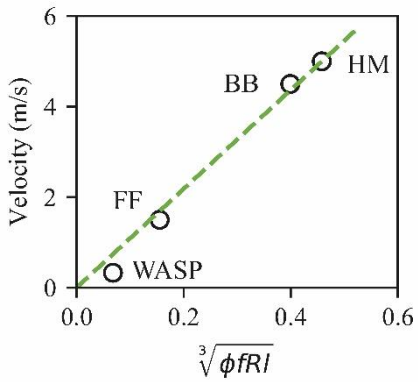

Fig. 3-8 Correlation between the flight velocity corresponding to the minimum *CoT* and the flapping parameters of four insects based on CFD simulations.

Based on the definition of cost of transport (Eq. 3-6), the theoretical scaling between *CoT* and flight velocity can be written as

$$CoT = \frac{P^*}{V_f} = C_1 \cdot \frac{1}{V_f} + C_2 \cdot {V_f}^2. \qquad (3-9)$$

More importantly, with the intention of achieving the minimum *CoT*, the corresponding flight velocity need to satisfy the following condition

$$V_{CoT_{min}} = \sqrt[3]{\frac{C_1}{C_2}} = \sqrt[3]{\frac{c_1 \emptyset f R}{\frac{c_2}{l}}} = \boldsymbol{k} \cdot \sqrt[3]{\emptyset f R \cdot l}\,, \qquad (3-10)$$

where k is a constant. According to CFD simulations, the minimum *CoT* is found to exist at certain flight velocity for all four insect models (Fig. 3-7). Remarkably, it can be seen in Fig. 3-8 that flight velocity $V_{CoT_{min}}$ corresponding to the least *CoT* calculated through CFD simulations appear to be proportional to $\sqrt[3]{\emptyset f R \cdot l}$ for all four flapping insects, implying the feasible prediction on the minimum cost of transport at certain flight speed.

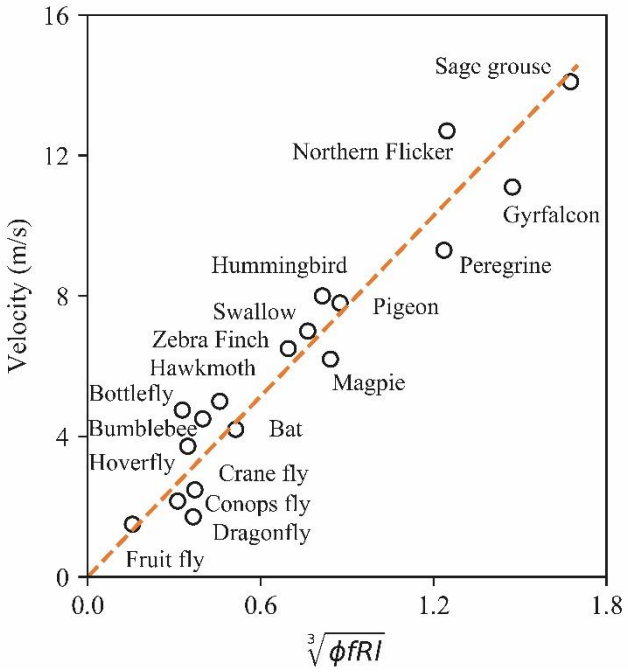

Fig. 3-9 Correlation between the cruising velocity and the flapping parameters of various insects and birds in nature based on experimental observations.

We additionally introduce some experimental observation data involving flapping

insects and birds at cruising condition as plotted in Fig. 3-9. Obviously, it is very likely to exist a proportional relationship between the CoT_{min}- corresponding flight velocity and the flapping parameters. This offers a path for predicting the optimal flight velocity corresponding to the minimum *CoT* for bio-flights, which has been verified through theoretical, numerical and experimental methods. A universal scaling law is also demonstrated for bio-flights that at certain flight velocity flying insects and birds could achieve the least input power for moving a given mass [77] and this special velocity is prone to be the most conducive cruising speed related with the kinematic parameters.

3.7 Elastic storage effect on flapping-wing dynamics robustness

The flapping-wing dynamics in bumblebee hovering is studied through a fluid-structure interaction (FSI) model with a specific focus on the passive and active mechanisms (PAM), which couples unsteady flapping aerodynamics and three-torsional-spring-based elastic wing-hinge dynamics. A PAM strategy of active-controlled stroke, passive-controlled wing pitch and deviation is proposed and verified to be capable of robustly simplifying the control of flapping flight while minimizing the high energetic cost by using elastic storage. The elastic storage in concern with elastic wing hinge enables minimization of the energetic cost while robustness of the flapping-wing dynamics. Featured by a dynamics-based passive elevation-rotation and an aerodynamics-based passive feathering-rotation, the robust flapping-wing dynamics is verified to enable the achievement of aerodynamic force production as well as high power efficiency over a broad range of wing-hinge stiffness.

Flying insects in nature frequently suffer from various external perturbations like rain drop or wind gust, which can largely alter their flapping-wing motions and body attitudes, and substantially lower the aerodynamic performance, flight stability and manoeuvrability. Thus, capability of the external perturbation-rejection is of great importance for insects

flying around under unsteady and complex natural environments. To further investigate how the passive wing deviation and pitch alter the feature of external perturbation-rejection, namely, the external perturbation robustness of flapping flight in bumblebee hovering, we built up a FSI model to simulate and examine how the flapping wings being exerted by a force impulse as a specific external perturbation respond dynamically in terms of the elevation-spring stiffness.

We first applied a downward force impulse on the mass centre of a single flapping wing at mid-downstroke lasting a period of 0.1T with a magnitude of 1500 $\boldsymbol{m_w}$, where $\boldsymbol{m_w}$ is the weight of wing. To examine the effect of the external perturbation on lift force production, we employed the normalized cycle-averaged lift defined as

$$\boldsymbol{L_c(t) = \frac{1}{TL_e}\int_{t-0.5T}^{t+0.5T} lift\, dt}, \qquad \boldsymbol{(3-11)}$$

where $\boldsymbol{L_e}$ denotes the cycle-averaged lift without the external perturbation.

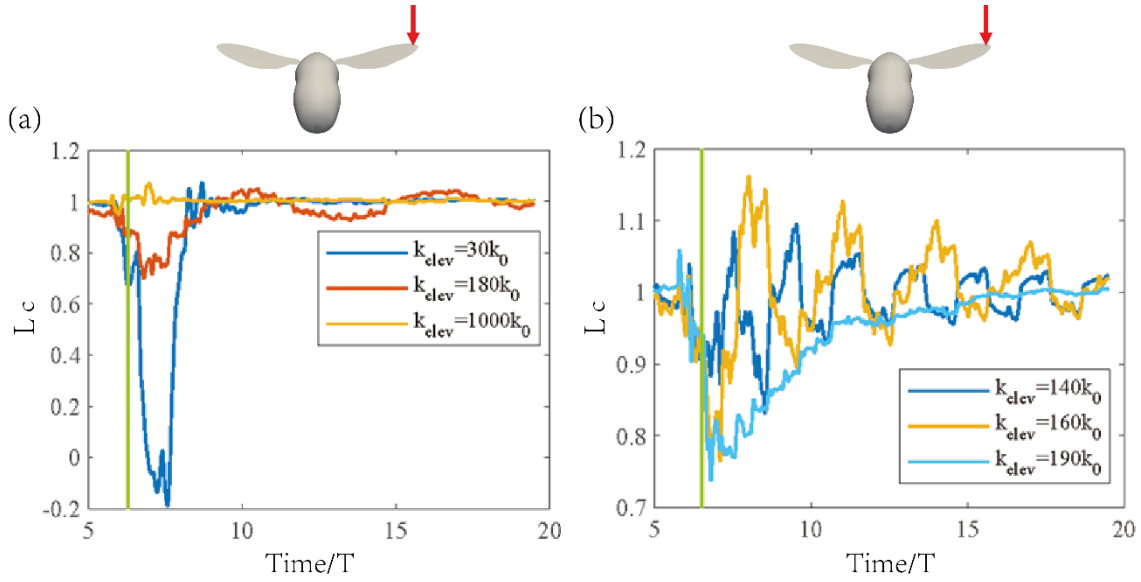

Fig. 3-10 Dynamic response of a flapping wing with passive elevation and feathering under a downward force-impulse perturbation. (a) Three representative elevation-spring stiffnesses in the domains *I* ($30k_0$), *II* ($180k_0$) and *III* ($1000k_0$), and (b) three elevation-spring stiffnesses in domain *II* ($140k_0$, $160k_0$, $190k_0$). Green line represents the time-period that the impulse acts on the wing. The feathering-spring stiffness of $\boldsymbol{k_0}$ ($\boldsymbol{2.61 \times 10^{-6}}$**Nm**) is an optimal value from a numerical study by Kolomenskiy *et al* [102].

Fig. 3-10 shows the dynamic response of a single flapping wing under a downward force-impulse perturbation, which is compared at three representative elevation-spring stiffnesses in the domains *I* ($30k_0$), *II* ($180k_0$) and *III* ($1000k_0$) (Fig. 3-10 (a)), and at three elevation-spring stiffnesses in domain *II* ($140k_0$, $160k_0$, $190k_0$) (Fig. 3-10 (b)). Obviously, the flapping wing is mostly perturbed at the elevation-spring stiffness of $30\boldsymbol{k_0}$ (Fig. 3-10 (a)) in domain *I*. The normalized cycle-averaged lift shows a rapid drop even down to the negative value, implying a crash because the 'very flexible' wing hinge cannot resist the strong force impulse and hence take a much longer period for the wing to return to the original position where a sufficient lift force ($\boldsymbol{L_c}$) is produced enough to sustain the hovering. Comparatively, the capability of the external perturbation-rejection is remarkedly enhanced with the elevation stiffness being increased up to $180\boldsymbol{k_0}$ in domain *II*, where the impulse-induced drop in $\boldsymbol{L_c}$ is declined to approximately 30% of the lift without the perturbation, and the $\boldsymbol{L_c}$ shows some fluctuations but a full recovery during two stroke cycles. With the stiffest elevation-spring ($1000\boldsymbol{k_0}$) in domain *III*, the flapping wing turns out to present the best rejection performance with marginal impact from the external perturbation. Such fluctuation feature that appears right after the external perturbation is further observed by comparison the three different elevation-spring stiffnesses in domain *II* (Fig. 3-10 (b)) but it behaves distinguishably at $140\boldsymbol{k_0}$ and $160\boldsymbol{k_0}$, where the $\boldsymbol{L_c}$ fluctuates around 1 compared to that of a gradual damping to 1 at $190\boldsymbol{k_0}$. Overall, for the six different elevation-spring stiffnesses in the three domains, while the distinguished features are observed the impacts on the wing dynamics due to the downward force-impulse perturbation are all limited to a very short period less than 2 ~ 4 wing beats but show obvious dependency on the domain that they belong to. Whereas the flapping wing with passive elevation and feathering does demonstrate the capability of the external perturbation-rejection over a broad range of the high elevation-spring stiffnesses, e.g., in the domains *II* and *III*.

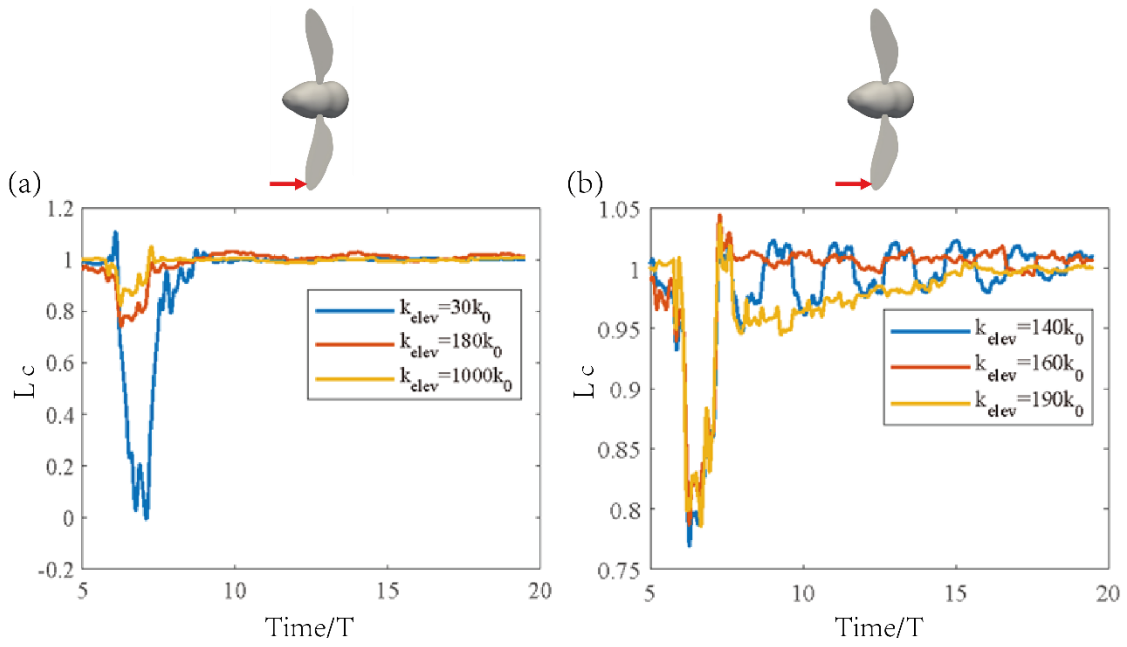

Fig. 3-11 Dynamic response of a flapping wing with passive elevation and feathering under a backward force-impulse perturbation. (a) Three representative elevation-spring stiffnesses in the domains *I* (30k_0), *II* (180k_0) and *III* (1000k_0), and (b) three elevation-spring stiffnesses in domain *II* (140k_0, 160k_0, 190k_0).

Furthermore, as a simple dynamic model of wind gust-induced external perturbations we examined the dynamic response of a flapping wing under a backward force-impulse perturbation, similarly in the domains *I* (30k_0), *II* (180k_0) and *III* (1000k_0) (Fig. 3-11 (a)), and in domain *II* (140k_0, 160k_0, 190k_0) (Fig. 3-11 (b)), respectively. Interestingly, similar trends are observed in the domains *I*, *II* and *III* as seen in the case of the downward force-impulse perturbation although there does exist some discrepancy at the elevation-spring stiffness of 1000$\boldsymbol{k_0}$ where a slight lift drop is present (Fig. 3-11 (a)), and in domain *II* where the lift forces at the three elevation-spring stiffnesses display a rapid recovery with much less fluctuations (Fig. 3-11 (b)). The results imply that the external perturbation-rejection associated with flapping wing under passive elevation and feathering is likely not direction-specific but of robustness in multiple directions.

The PAM-based control strategy is further confirmed capable of enhancing the robustness in association with external perturbation rejection under unsteady conditions of

wind gust. It is revealed that an optimal aerodynamic design in terms of robust vertical force production and high mechanical efficiency can be achieved at an elevation-spring stiffness around $k_\theta = 190k_0$.

Chapter 4 Wing-body interaction effects on aerodynamics and energetics

4.1 Introduction

In the past decades, the flapping-wing aerodynamics for the insects and birds hovering and forward flight has been explored to solve a central problem involving the complex vortex dynamics generation correlated with the aerodynamic force production [7-11, 19-22]. The leading-edge vortices (LEV) are likely to be a universal mechanism for the enhancement of the aerodynamic force in flying animals [4, 5, 8, 13, 14, 50, 51, 103, 104]. However, the studies on unsteady aerodynamics and energetics have been mainly focused on single or paired flapping wings, it remains uncovered in terms of the interactions between flying body and flapping wings at various flight velocities.

The impact of the moving body and its interplay with flapping wings on vortex-dominated flow structures and aerodynamic force production has been studied experimentally for flapping flight of insects and birds. Smoke-trail-based studies on butterfly free flight [25] and on dragonfly forward flight [26] reported a LEV-like near-field flow structure across the thorax region of the body, which is in agreement with the study of Bomphrey *et al.* [28] for tethered moths at freestream velocities of 1.2 and 3.5 m/s obtained via flow visualizations and digital PIV methods, suggesting a significant body-induced contribution to vertical force. CFD-based studies have also considered flapping forward flight (e.g., in cicadas [40, 41], fruit flies [57], hawk moths [43], and hummingbirds [42, 58]) and have confirmed the formation of body-based vortices attached to the upper body surface and pointed out some notable enhancements to lift stemming from the wing-body (WB) interaction in the hovering of fruit flies [59, 60, 105] and in forward flight of cicadas [40, 41] and hummingbirds [42, 58]. Whereas these studies have

focused on and have thus been limited to the flapping aerodynamics associated with hovering or some specific forward flight velocities, an overall understanding of how flying insects regulate their wing kinematics and body motion in correlation as a function of flight velocity to enhance aerodynamic force production via the WB interaction remains an open question.

To investigate the forward-flight energetics, the power costs at various flight velocities have been estimated for insects [43, 65-67] as well as bird species [53, 68, 70]. Note that previous studies were conducted either at specific flight velocities or used simplified aerodynamic models based on the quasi-steady approach, blade-momentum theory, and the discrete vortex-sheet method [4] without considering the wing-body interaction. In addition, few studies have investigated how the morphological and dynamic parameters affect the WB interactions for aerodynamic force and energy consumption in the flapping forward flight of insects and birds. Liu *et al* [41] reported a CFD-based analysis of cicada forward flight and investigated how the minimum WB distance, body inclination angle, and reduced frequency affect lift enhancement owing to WB interactions. Wang *et al* [58] investigated the advance ratio and inclination angle of the body and how the tail shape affects the WB interaction in hummingbird forward flight. Conversely, it remains unclear how, over a broad range of flight velocities, the aspect ratio AR [61, 62, 106], the wing-to-body mass ratio (WBMR) [63, 64], and the reduced frequency k [41] correlate with the WB interaction in terms of the unsteady aerodynamics and energetics in insect forward flight.

Herein we investigate the WB interaction mechanisms associated with flapping aerodynamics and energetics in the hawk moth hovering and forward flight over a broad range of flight velocities. We develop a WB morphological model of the hawk moth and the realistic WB kinematics for hovering and forward flight with five different velocities constructed from experimental data. The model is further modified for trimmed forward

flight by using a genetic algorithm embedded within a CFD-driven aerodynamic model. Also introduced is a versatile and high-fidelity CFD model specifically designed for the forward flapping flight of flying insects; this model enables precise prediction of vortical dynamics, aerodynamic forces, and power consumed for a variety of flying motions. We comprehensively analyze the near-field vortex-dominated flow structures, including LEV- and body-vortex-based mechanisms for WB, wing-wing, and body-only models, and how the WB interaction affects the power consumption and aerodynamic force production as functions of speed. Furthermore, we extensively discuss the parametric effects on WB interactions involving the aerodynamics and energetics over a broad parameter space involving aspect ratio, wing-to-body mass ratio, and reduced frequency.

4.2 Results

4.2.1 Effect of interplay between flapping wings and body on unsteady aerodynamics

We now investigate the flapping aerodynamics associated with the wing-body (WB) interaction for hovering and for forward flight at five velocities. The flapping wings and flying body are now further examined separately in terms of how they depend on flight velocity by illustrating the cycle-averaged body-based aerodynamic forces as a function of forward-flight velocity (Fig. 4-1). This task is undertaken by considering the net horizontal force and the percent of vertical force vs the weight of the hawk moth.

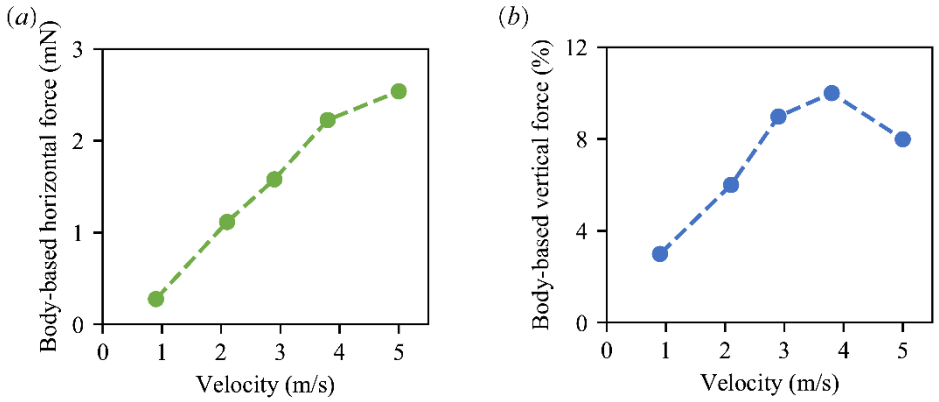

Fig. 4-1 Cycle-averaged body-based forces vs forward flight velocity: (*a*) horizontal forces and (*b*) percentages of body-based vertical forces with respect to the hawk moth's weight.

The flying body experiences a drag force due to the horizontal force, which increases with increasing flight velocity (Fig. 4-1 (*a*)), while producing a lift due to the vertical force, which depends on velocity and is 8% of the hawk moth's weight at greater flight velocities with a maximum of approximately 10% (Fig. 4-1 (*b*)). For the body-based vertical force, the present results are consistent with the observation [65] that the largest body-based vertical force in the fast forward flight of a hawk moth is around 10% of the body weight. It is also reported that the body-induced vertical force is less than 10% for bumblebees [66], 5% for honeybees [107], 3%–4% for fruit flies [57], 12.0% for cicadas [41], and 13.8% [42] or 12.8% [58] for hummingbirds at a specific flight velocity.

We further report that the body-induced vertical force is enhanced by the interplay between the flapping wings and moving body. For comparison, we conducted two additional simulations associated with a body-only model with the two wings removed and a wing-only (WO) model without the body at five forward flight velocities to investigate how the vortex-dominated flow structures in forward flight contribute to the vertical force (Fig. 4-2). The body-based vertical forces of a wing-body model and a body-only model at the flight velocity of 3.8 m/s are firstly compared in Fig. 4-2 (*a*), in which the force is observed to remain almost constant for body-only model while fluctuates between higher peaks for wing-body model throughout a wingbeat stroke. Along with the pressure

distributions on the body surface (Fig. 4-2 (*c*)) and the near-field vortex dynamics (Fig. 4-2 (*d*) and (*e*)) in fast forward flight (3.8 m/s), we can further explain the correlations between vortex dynamics and body-based vertical force production at typical stages of A, B, C, D in Fig. 4-2 (*a*). At the early downstroke (*t/T* = 0.14), a negative-pressure region appears (Fig. 4-2 (*c*) A) with the formation of the first force peak (Fig. 4-2 (*a*) A), corresponding to the location of a rear-body vortex (Fig. 4-2 (*d*) A), which merges with the head vortex and the LEV, tip vortex, and trailing-edge vortex, forming a downstroke vortex tube ring. It moves substantially backward, attaching to the aft of the body at *t/T* = 0.38 (Fig. 4-2 (*d*) B); meanwhile, another negative-pressure region (Fig. 4-2 (*c*) B) corresponding to the intense thorax vortex (TXV) appears (Fig. 4-2 (*d*) B), which is generated by the head vortex and results in the second vertical force peak (Fig. 4-2 (*a*) B). At the early upstroke (*t/T* = 0.66), the intense TXV feeding by the head vortex is developed and strengthened (Fig. 4-2 (*d*) C), leading to a strong negative-pressure region (Fig. 4-2 (*c*) C) and thus the third vertical force peak (Fig. 4-2 (*a*) C). The TXV breaks down with the head vortex, shedding off from the aft of the body (Fig. 4-2 (*d*) D) and leading to a noticeable reduction in vertical force at the late upstroke (*t/T* = 0.82) (Fig. 4-2 (*a*) D). The near-field vortex dynamics and wake topologies of a WB model and a WO model are also visualized and given at the other four flight velocities of 0.9, 2.1, 2.9, 5.0 m/s. The *Q*-criterion iso-surface [95] with $Q = \frac{1}{2}(\|\boldsymbol{\Omega}\|^2 - \|\boldsymbol{S}\|^2) > 0$ identifies the vortex structure (for illustration, the non-dimensional *Q* criterion here is 0.05), where $\boldsymbol{S} = \frac{1}{2}[\nabla\boldsymbol{u} + (\nabla\boldsymbol{u})^T]$ and $\boldsymbol{\Omega} = \frac{1}{2}[\nabla\boldsymbol{u} - (\nabla\boldsymbol{u})^T]$ denotes the strain-rate and vorticity tensors, respectively, and $\boldsymbol{u}$ is the velocity vector. The normalized helicity density serves for color mapping to illustrate the rotational directions of vorticity. Overall, the simulated flow patterns for hawk-moth forward flight in terms of the wing-based leading-edge vortex (LEV) in structure, location, and size are entirely agree with the experiments made by smoke trail [24] and digital PIV techniques [28]. Note that Bomphrey *et al* [28] could not provide time-dependent snapshots of the vortex fields to

illustrate the shedding and formation of the LEV-like structures above the thorax and the rear-body vortex throughout the wingbeat stroke. However, the present simulations have clarified the attachment and detachment nodes of the LEV-like structures above the thorax, as suggested in their study of the forward flight of a tethered hawk moth.

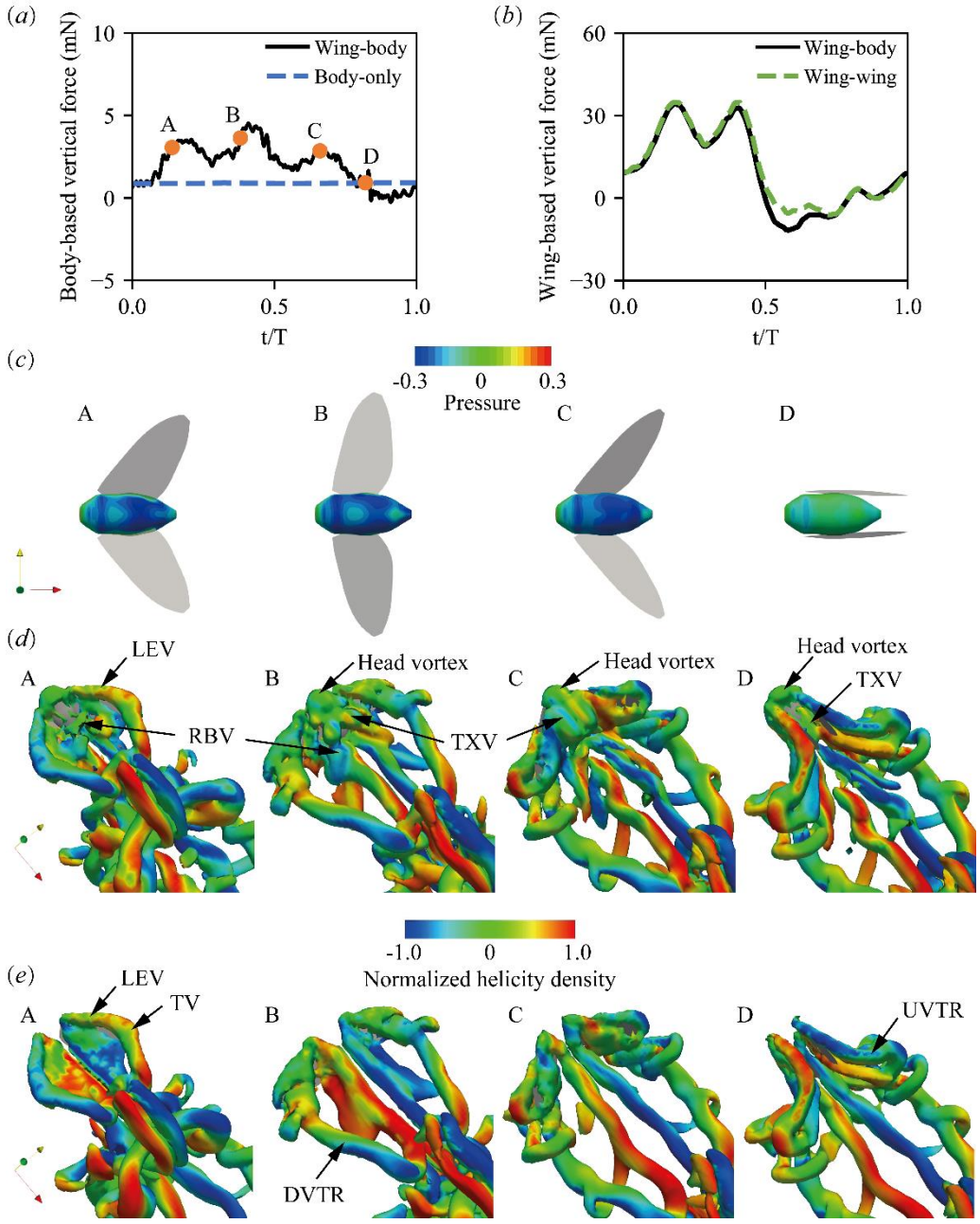

Fig. 4-2 Body-based vertical forces and pressure distributions as well as vortex structures at the flight

velocity of 3.8 m/s. (a), (b) Comparisons of body- and wing-based vertical forces of a WB model, a WO model, and a body-only model. (c) Pressure distributions on body surface of a WB model at four instants: t/T = 0.14 (**A**), 0.38 (**B**), 0.66 (**C**), 0.82 (**D**). (d), (e) Illustration of near-field vortex dynamics of a WB model and a WO model at four instants: t/T = 0.14 (**A**), 0.38 (**B**), 0.66 (**C**), 0.82 (**D**).

Comparatively, while the LEV-based vortex tube rings also appear during down- and up-strokes of the WO model, a pair of parallel vortex tubes (Fig. 4-2 (*e*)) replace the body vortex (Fig. 4-2 (*d*)) produced by the WB model. The WO model produces slight differences from the WB model in the flapping wing-based vertical force (Fig. 4-2 (*e*)) and the LEV features on the wing surface are similar to those of the WB model (Fig. 4-2 (*d*) and (*e*)). Conversely, the body-based vertical force of the body-only model remains almost constant throughout a wingbeat stroke; for instance, it retains the low value of 0.9 mN for the flight velocity of 3.8 m/s (Fig. 4-2 (*a*)) because the WB interaction does not induce a body vortex. The WB model creates a much greater mean vertical force of 2.0 mN for a fast forward flight of 3.8 m/s, with the significant increase of 122% attributed to the interplay between the wing-induced LEVs and the body-induced vortex. Such a WB-interaction-based lift-enhancement mechanism also occurs in cicadas forward flight, where a thorax-based vortex benefits the downwash jet [40], considerably aiding the vortices formation on posterior and thorax of insect [41].

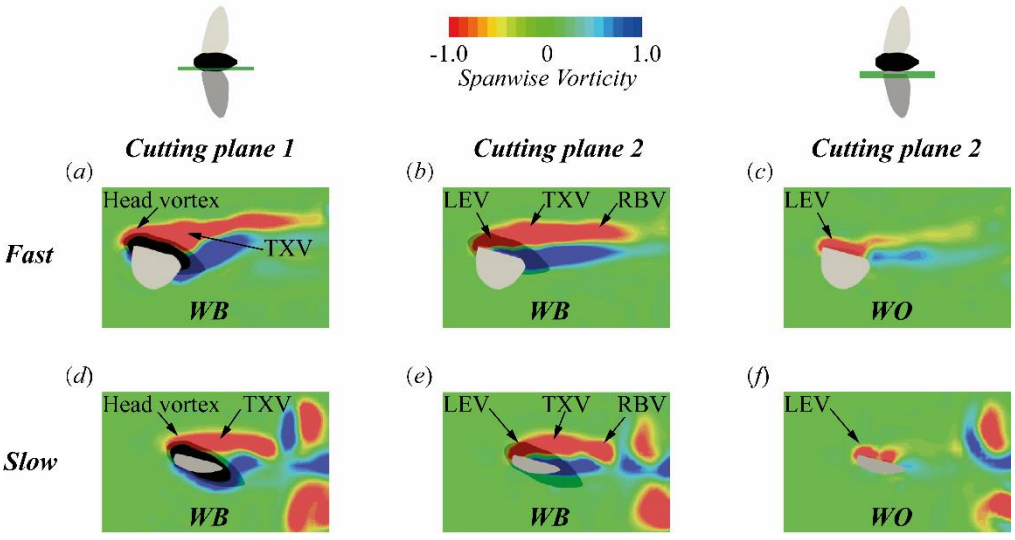

Fig. 4-3 Vortex topologies in the vicinity of the wing root for the WB and WO models at t/T = 0.38 in (*a*)–(*c*) fast forward flight of 3.8 m/s and (*d*)–(*f*) slow forward flight of 2.1 m/s. Vorticity contours are visualized on two cutting planes located at $0.3c_m$ (cutting plane 1 for the WB model) and $0.6c_m$ (cutting plane 2 for the WB and WO models) away from the symmetry plane of the insect's body. The head vortex, LEV, TXV, and rear-body vortex are also marked in the figure.

Overall, the aerodynamic interplay between the body and flapping wings is confirmed to play an important role in hawk-moth forward flight, with the TXV and rear-body vortex detected for all flight velocities. To further investigate the velocity dependence of the WB interaction, Fig. 4-3 plots the vorticity contours in the vicinity of the wing root on two cutting planes for WO and WB models in slow and fast forward flights. On cutting plane 1, both the head vortex and the TXV are attached coherently onto the body surface and are strongly connected to each other (Fig. 4-3 (*a*) and (*d*)): the TXV is larger and stronger at fast forward flight (Fig. 4-3 (*a*) and (*d*)) than at slow forward flight, moving rearward and substantially detaching from the posterior of the body (Fig. 4-2 (*d*) C, D), which corresponds to the enhanced body-based vertical force in fast flight, as shown in Fig. 4-1 (*b*). On cutting plane 2, a wing root vortex is significantly reinforced in the WB model compared with the WO model (Fig. 4-3 (*b*), (*c*), (*e*), (*f*)), which is also confirmed in cicada forward flight [41]. Interestingly, this wing root vortex together with the LEV and TXV are significantly elongated in fast forward flight (Fig. 4-3 (*b*) and (*e*)), as also occurs in the high-advance-ratio forward flight of hummingbirds [58]. In addition, the flapping-wing-induced LEV develops and grows more intense with increasing flight velocity, as observed in smoke-trail experiments [24]. In accordance, the TXV is also strengthened at high flight velocities, as confirmed by digital-PIV-based experiments [28] that report a much more intense TXV at 3.5 m/s than at 1.2 m/s. This velocity-dependent feature in the TXV is tentatively attributed to the interplay between the intense head vortex and the LEVs induced by the WB interaction at high flight velocities (Fig. 4-2 (*d*)). The

same result occurs in hummingbird flight, namely, that the head vortex is strongly associated with the formation of the TXV during most of the flapping cycle [58].

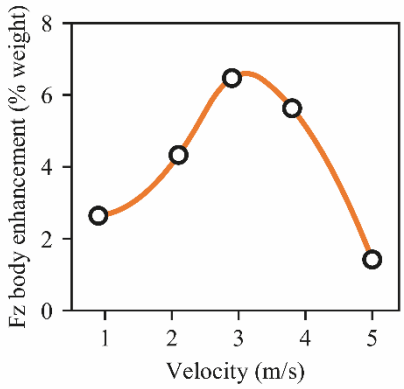

Fig. 4-4 Body-based vertical force enhancement (% weight) on the WB model with respect to the body-only model in various forward flight velocities.

The WB aerodynamic interaction plays a crucial role in producing vertical force. As depicted in Fig. 4-4, the body-based vertical force associated with the WB model is significantly enhanced compared with the body-only model, which depends on the flight velocity. Corresponding to the intense vortex topologies induced by the WB interaction, as shown in Fig. 4-3, the body-based contribution occurs at all flight velocities and is optimal at forward flight velocities of 2.9–3.8 m/s, with a maximum of 6.5% (Fig. 4-4). A similar feature also occurs during hummingbird forward flight [58], displaying some advanced ratios that lead to optimal aerodynamic force production over a specific range of flapping frequencies, which was suggested due to the WB interaction.

Thus, the results show that both the universal LEV-based mechanism [98] and the unique body-vortex-based mechanism and their velocity-dependent interactions are responsible for augmenting the aerodynamic force produced in the forward flight of hawk moths at various velocities.

4.2.2 Interplay between flapping wings and body and its effect on energetics

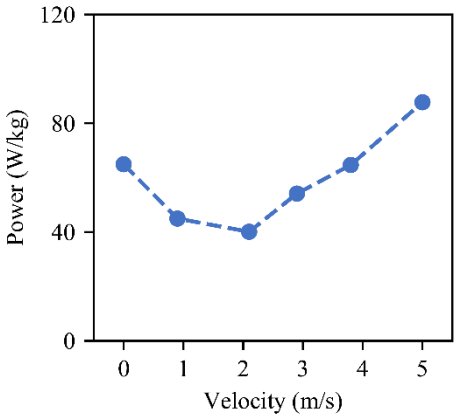

Fig. 4-5 Time-averaged body-mass-specific total positive mechanical powers during hovering and during five forward flights.

As depicted in Fig. 4-5, the correlation between power cost and flight velocity is further investigated with the time-averaged, body-mass-specific, total positive mechanical power during hovering and forward flight at five velocities. The results produce a *J*-shaped power curve in which the minimum mechanical power density (40.1 W/kg) occurs near the slow flight velocity of 2.1 m/s, whereas both hovering (64.9 W/kg) and fast forward flight consume significant power, particularly at the top velocity of 5 m/s (87.7 W/kg). Note that the relatively low power consumption at intermediate flight velocities may due to the effective utilize of drag force for lift generation [43], which provides the hawk moth an energetic and efficient forward-flight zone.

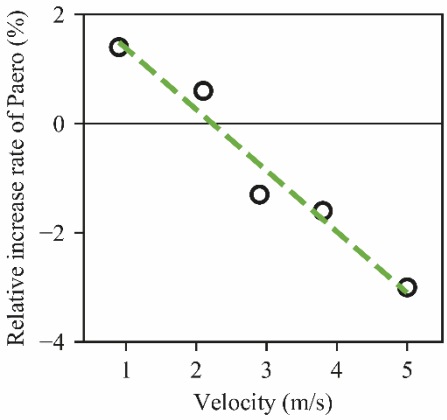

Fig. 4-6 Relative rates of increase of body-mass-specific aerodynamic power for WB model with respect to the sum of body-mass-specific aerodynamic powers for the body-only (BO) and WO models in various forward flight velocities [$\Delta P_{\mathrm{aero}}(\%) = \frac{P_{\mathrm{aero,WB}}}{P_{\mathrm{aero,BO}} + P_{\mathrm{aero,WO}}} - 1$].

We further show how the WB interaction affects energetics by comparing the power consumption of the realistic WB model with that of the body-only and WO models. Since the inertial power remains constant, the relative rate of increase of the aerodynamic power for the WB model is positive for hovering and slow forward flight but becomes negative for fast forward flight, indicating a decrease with increasing flight velocity (Fig. 4-6). This indicates that the required power decreases for the WB model for intermediate-speed and fast forward flights, with the highest energy saving of 3% occurring with the combination of body-only and WO models. Thus, the WB interactions play a crucial role in lowering the aerodynamic power cost in association with forward flights of intermediate and high velocities.

4.3 Discussions

4.3.1 Effect of aspect ratio

The effects of the aspect ratio *AR* of the hawk-moth wing on aerodynamics and energetics at various forward flights speeds are now further investigated by modifying the

wing morphology in both the spanwise and chord-wise directions while keeping the wing area unchanged. Given that the hawk-moth wing (i.e., the original model) has *AR* = 5.4 and a single wing area S_w, which is determined as the product of the wing length *R* and the mean chord length c_m, with $AR = \frac{2R^2}{S_w}$ we define two additional wing models: *AR* = 3.8 (Model 1) and *AR* = 7.2 (Model 2) (Fig. 4-7). Simulations were undertaken for hovering and for forward flights with four velocities with the case of the top velocity (5.0 m/s) excluded because the enlarged wing Model 2 does not ensure the numerical convergence and stability for that flight velocity. Moreover, since the previous studies on the forward flight of cicadas [41] and hummingbirds [58] both reported that the body kinematics significantly affect the increase in lift over a broad range of body angle (20°–50°), here we focus only on the *AR* effect with the same WB kinematics used for the three wing models.

We now examine the LEV-based and body-vortex-based lift enhancement mechanism in terms of *AR* via pressure distribution on three wings configurations and on body surface during the downstroke in Fig. 4-7 (*a*) and (*b*). Both the downstroke LEV and body vortex increase in size and strength with increasing flight velocity, producing an increasingly enlarged negative-pressure region with increasing *AR*. In addition in Fig. 4-8 (*a*) and (*b*), both mean wing- and body-based vertical forces significantly decrease as *AR* decreases compared with the realistic WB model and significantly increase as *AR* increases. This implies that high-*AR* wings enhance both the wing- and body-based vertical force, and the strengthened LEV may significantly affect the reinforcement of the body vortex due to their interplay.

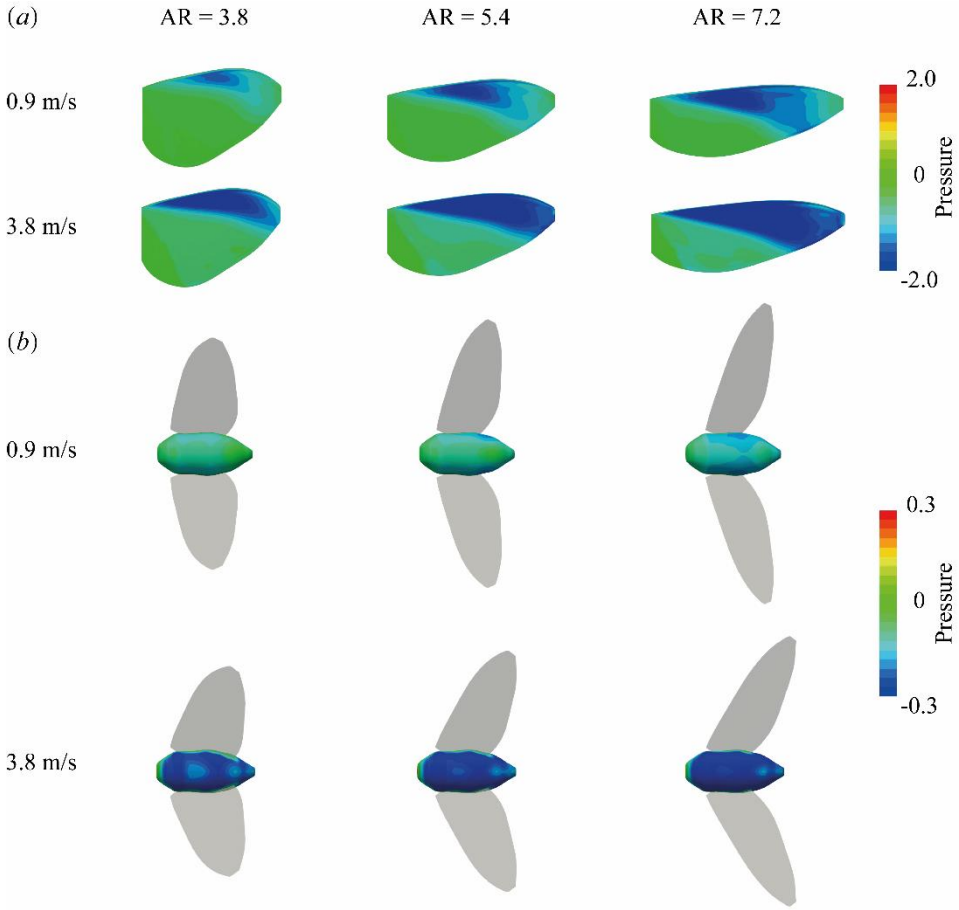

Fig. 4-7 (*a*) Wing- and (*b*) body-surface pressure distributions for the three wing models (Model 1: *AR* = 3.8; Realistic model: *AR* = 5.4; Model 2: *AR* = 7.2) for slow and fast forward flight.

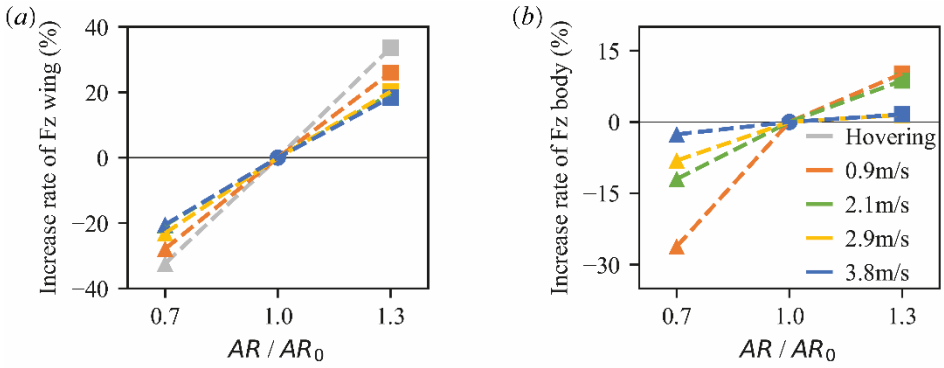

Fig. 4-8 Relative rate of increase of (a) wing-based vertical force and (b) body-based vertical force for the WB model with the modified wings of *AR* = 3.8 (triangle) and 7.2 (square) and the original wing with *AR* = 5.4 (circle) for flights of various velocities.

To further quantify how wing morphology affects the LEV and body-vortex aerodynamics, we use the pressure-based LEV angle γ, as proposed in our previous study [108]. As the negative pressure distribution in the chord-wise direction tends to have an inflection point, we define here the imprint points by choosing three chord-wise positions corresponding to the non-dimensional negative pressure $P_0 = -1.0$ at the three cutting planes of 30%, 50%, and 70% wingspan (Fig. 4-9). Following the method of Chen *et al.* [108], we then define the LEV angle γ as

$$= \frac{1}{N}\sum_{i=1}^{N}\left[\tan^{-1}\left(\frac{x_i}{y_i}\right) - \tan^{-1}\left(\frac{x_{LE_i}}{y_i}\right)\right], \qquad (4-1)$$

where x_{LE_i} is the leading-edge position on the cutting plane, x_i is the chord-wise position of the imprint points, y_i is the spanwise position with respect to the wing base, and N is the number of imprint points. We thus quantify the LEV morphology in terms of the chord-wise expansion of the vortex core at various forward velocities.

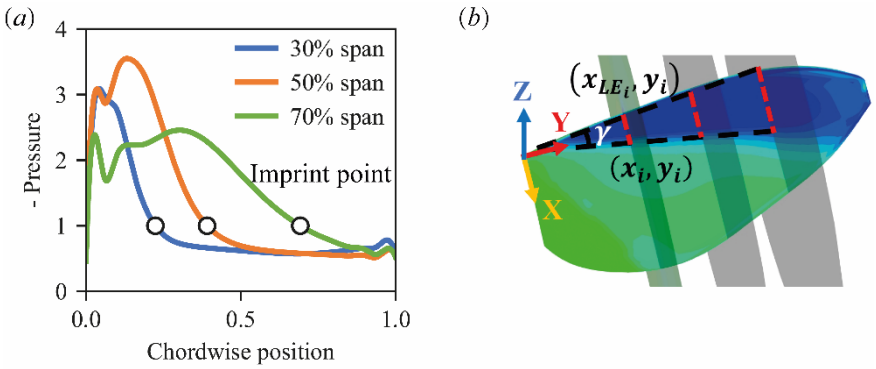

Fig. 4-9 Imprint point and LEV angle. (a) Sectional imprint points defined at non-dimensional negative pressure, $P_0 = -1.0$, on pressure distribution curves of three span-wise positions. The chord-wise position is normalized by the sectional chord length. (b) Schematic showing LEV angle γ.

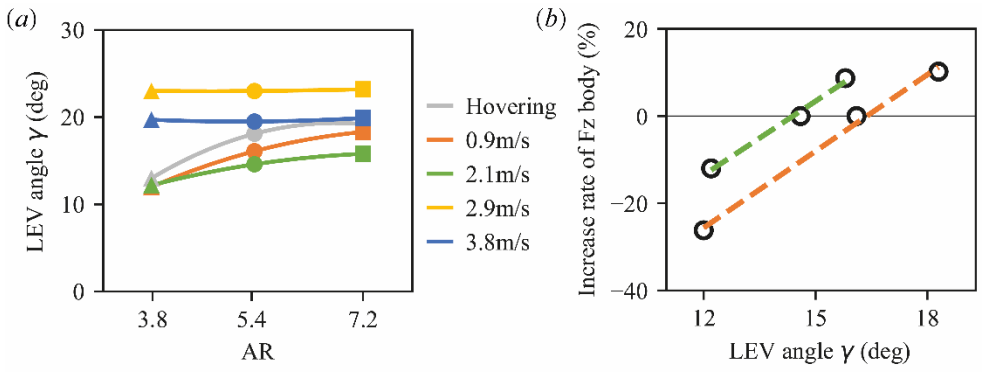

Fig. 4-10 (*a*) Calculated LEV angle γ with different wing *AR* = 3.8 (triangles), 5.4 (circles), and 7.2 (squares) at various flight velocities. (*b*) Correlation between LEV angle and relative rate of increase of body-based vertical forces with different *AR*s for forward flight at slow velocities of 0.9 and 2.1 m/s.

Fig. 4-10 shows the LEV angles for three wing *AR*s and for hovering and forward-flight velocities of 0.9−3.8 m/s. The calculated LEV angle γ increases with increasing *AR* for slow forward flight, whereas it depends less on *AR* for fast forward flight. The LEV-induced negative-pressure region grows significantly, being stretched spanwise in high-*AR* wings for all flight velocities (Fig. 4-7), whereas the conical LEV angle is more sensitive to the shortened wing chord length for slow forward flight, with even an increase in wing chord length (Fig. 4-10). This is consistent with the results for the LEV features of flapping fruit fly wings [62] that the increasing *AR* shortens the chord length of wings relative to the size of LEV.

More importantly, we may further assume that the body-induced vortex and the WB interaction are more sensitive to wing-chord length. The body-based vertical force shows the highest relative rate of increase with different aspect ratios, particularly for hovering and slow forward flights (Fig. 4-8 (*b*)), which is consistent with the significant increase in LEV angle with higher aspect ratios for hovering and slow forward flights (Fig. 4-10 (*a*)). As depicted in Fig. 4-10 (*b*), the body-based vertical force increases significantly as the conical LEV angle grows, which is likely because of the larger chord-wise LEV involved with the body vortex in the vicinity of the wing root. This indicates that, although the

formation of leading-edge vortices matches well spanwise with the wing morphology [108], the reinforcement of the body vortex is very likely due to the enlarged LEV morphology in the chord-wise direction owing to the WB interaction.

4.3.2 Effect of wing-to-body mass ratio

The WBMR plays a significant role in altering the aerodynamics and energetics of the free hovering flight of insects [64]. We further investigate this phenomenon here for the case of the five forward flights of a hawk moth with three different WBMRs: 0.0%, 4.49% (realistic), 8.98% ($\varepsilon = [0, 1, 2]\ \varepsilon_r$) with the total mass kept constant. Here, the same WB kinematics are used for the three different WBMR models because we aim to examine the WBMR effect. Xu *et al* [64] showed that, in free hovering flight, the body oscillation in flapping-wing feathering angle significantly reduces the vertical force. In the present work, with both fixed body and wing kinematics of tethered forward flight, the inertial forces, torques, and unsteady aerodynamics are independent of the WBMR.

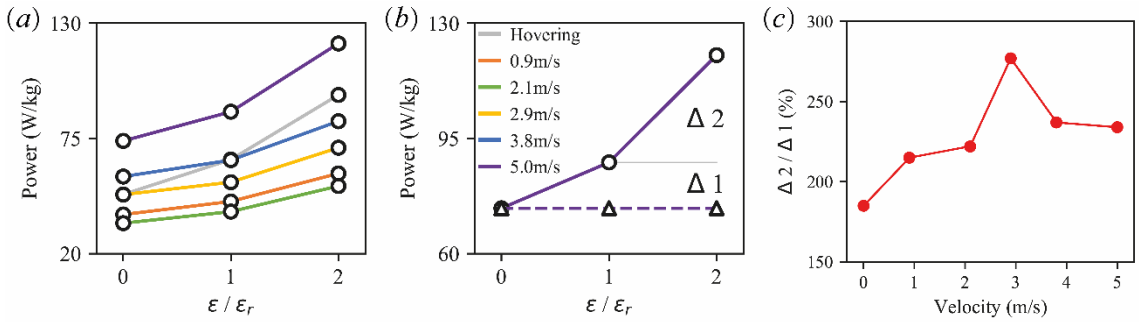

Fig. 4-11 (*a*) Cycle-averaged body-mass-specific total positive mechanical power vs WBMR for hovering and forward flights of hawk moth (solid lines). (*b*) Definition of the extra power consumption (Δ1, Δ2) and the additional perfect elastic-energy storage (dashed lines) during fast forward flight at 5 m/s. (*c*) Relative ratio of extra power consumption in two rising regions (Δ2 / Δ1) at various flight velocities.

Thus, we investigate here the key role of inertial and/or aerodynamic components in power consumption. Fig. 4-11 (*a*) plots the cycle-averaged body-mass-specific total

positive power with different WBMRs. With the assumption of elastic storage as zero, the total power consumed is significantly affected by wing inertia. For comparison, we also show in Fig. 4-11 (*b*) a perfect case of elastic-energy storage because the average inertial power vanishes, so the total power in a stroke comes into a pure aerodynamic power [64].

The power cost vs WBMR increases at a greater rate during hovering and fast forward flight than during slow forward flight, and a similar trend occurs for all flight velocities (i.e., the power consumption increases significantly for $\varepsilon/\varepsilon_r$>1 than for $\varepsilon/\varepsilon_r$< 1), with the extra power consumption occurring for $\Delta 2 > \Delta 1$ (Fig. 4-11 (*b*)). At some WBMR below the realistic one ($\varepsilon/\varepsilon_r$<1), based on the assumption of non-elastic-energy storage whereby the negative total power is assumed to be zero, portions of the aerodynamic power are canceled out by the negative part of inertial power, which suppresses the increase in total power [64]. When the WBMR becomes greater than the realistic ratio ($\varepsilon/\varepsilon_r$>1), the aerodynamic power remains unchanged and the added inertial power leads to less negative power in the total power, so that the increase in total power is similar to the rise in inertial power. This phenomenon is entirely consistent with the results from hovering flights of fruit flies, bumblebees, and hawk moths in terms of WBMR [64]. Comparing extra power consumption of the slow region with that of the fast region shows that the relative ratio of extra power consumption between two rising regions ($\Delta 2$ and $\Delta 1$) increases with increasing flight velocity and even triples when $\varepsilon/\varepsilon_r$>1 at the intermediate flight velocity of 2.9 m/s (Fig. 4-11 (*c*)). We infer from this that the realistic WBMR is likely to be a common and crucial inflection point between the slow and fast rates of increase and is more sensitive for intermediate and fast forward flight, capable of producing relatively low power consumption for various forward flights of the hawk moth.

4.3.3 Effect of reduced frequency

When analyzing a natural flyer's aerodynamic performance, an important parameter reduced frequency k [4] characterizes rotation vs translation in flapping flight, which is

defined as

$$k = \frac{\pi f L_{ref}}{U_{ref}} = \frac{\pi f c_m}{U_f}, \qquad (4-2)$$

where the mean chord length c_m serves as L_{ref}, the forward velocity U_f is U_{ref}, and f is the flapping frequency.

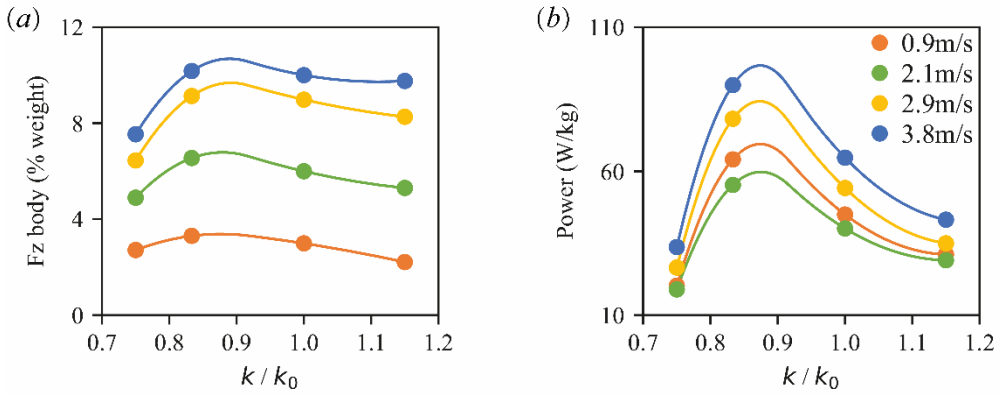

Fig. 4-12 Reduced frequencies (realistic k_0, relative k/k_0) vs (a) body-based vertical force (% weight) and (b) body-mass-specific total positive power for various flight velocities.

To elucidate how reduced frequency affects the aerodynamic force production and energetics of hawk-moth forward flight, Fig. 4-12 shows reduced frequency as a function of body-based vertical force and the body-mass-specific total positive power. The body-based contributions for vertical force account for 2%–12% of the insect's weight, which is particularly significant for fast forward flight (3.8 m/s). The body-based vertical force decreases at both the low and high ends of the relative reduced frequencies (k/k_0) but sustains the greatest enhancement in the region $0.8k_0 < k < k_0$ (Fig. 4-12 (*a*)). Similar optimal reduced frequency corresponding to significant lift enhancement is reported for cicadas at $k = 0.75k_0$ [41], which indicates that the hawk moth may also reach the optimal aerodynamic performance with a slightly lower flapping frequency, benefiting more from the WB interaction at various speeds of forward flight.

Finally, the total mechanical power consumption, which generally rises with increasing flight velocity (Fig. 4-12 (*b*)), decreases sharply with increasing reduced

frequency when $k > 0.9k_0$, whereas it reaches its lowest level at $k = 0.75k_0$. This implies that the power consumption in hawk moth forward flight may be less robust near the realistic k_0 because it can be more sensitive to variations in insect size and flapping frequency.

4.4 Concluding remarks

This chapter develops an integrated computational framework to study how the interplay between flapping wings and the flying body affects the unsteady aerodynamics and energetics of hawk-moth flight (*Manduca Sexta*) over a broad range of flight velocities. We apply a realistic wing-body morphological model, a realistic wing-body kinematic model, and a high-fidelity CFD solver [9]. For different velocities in hovering and forward flights, the trimmed flapping flights are obtained by using a CFD-driven genetic algorithm [92]. A systematic simulation-based study is presented for various flight modes comprising hovering, slow, intermediate, and fast forward flight to explore the near-field flow structures, the aerodynamic force produced, and the power consumption associated with wing-body (WB) interaction over a broad range of parameter space defined by aspect ratio, wing-to-body mass ratio, and reduced frequency. The main findings are summarized as follows:

(1) Both the leading-edge-vortex-based and body-vortex-based mechanisms, as well as their velocity-dependent interactions augment the aerodynamic force for forward flight of various speeds of the hawk moth. Since the universal leading-edge vortex (LEV) becomes stronger with increasing flight velocity and creates most of the aerodynamic force, the unique body vortex involving a rear-body vortex and a thorax vortex induced by wing-body interaction augment the vertical force by up to 10%, particularly for forward flight of intermediate and high velocities. The velocity-dependent body vortex is due to the interplay between the intense head

vortex and the leading-edge vortex induced by the wing-body interaction at high flight velocities.

(2) The body-mass-specific time-averaged total mechanical power forms a *J*-shaped power curve with increasing flight velocity, and the power cost decreases for the realistic wing-body model, with the greatest energy saving of 3% occurring due to the interplay between flapping wings and body, particularly for flight at intermediate and high velocities.

(3) High-*AR* wings enhance both wing- and body-based vertical force for forward flight at various velocities, additionally implying that body-vortex formation is affected by the morphology of the leading-edge vortex in the chord-wise direction due to the wing-body interaction. The realistic wing-body mass ratio (WBMR) reflects a crucial inflection capable of producing low power consumption for all forward-flight velocities. A slightly lower reduced frequency produces the optimal aerodynamic performance for the body of the hawk moth for forward flight of various velocities.

Chapter 5 Biofluid wave-based scaling laws in biological flight of insects, bats and birds

5.1 Introduction

Bio-swimmers and flyers exploit the interplay between their body and the induced flow to achieve aquatic and aerial locomotion [109-111]. More than 60 years, traditional views on classifying the fluid physics of animal locomotion in swimming and flying can be summarized via four typical criterions, such as, laminar or turbulent flow-based Reynolds number (*Re*) [73, 111]; steady or unsteady motion-based Strouhal number (*St*) [72]; viscous or inertial force-based fluid drag [73]; Froude efficiency (η_{Fr}) or Cost of Transport (*CoT*) -based energetic efficiency [69, 74-76, 112]. Taylor *et al* demonstrate a narrow range of Strouhal number (*St*) for the cruising flying and swimming animals to achieve high power efficiency [72]. Gazzola *et al* derived a scaling principle that links velocity to body kinematics and fluid properties, spanning eight orders of magnitude in Reynolds number [73]. Considering that most macroscopic locomotion is essentially characterized in wave phenomenon, a unique biofluid wave-based scaling law for biological flight of insects, bats and birds as well as its correlations with the force-based Reynolds number (*Re*) and the motion-based Strouhal number (*St*) remain uncovered.

Inconsistency associated with traditional viewpoints still exists according to several computational and experimental studies. Bio-swimmers and flyers are explained to follow a principle that they locomote at a specific Strouhal number (*St*) or reduced frequency (*k*) to maximize Froude efficiency (η_{Fr}) [72]. Observations of fish swimming however demonstrate that they obey a rule to minimize Cost of Transport (*CoT*) through adjusting the essential kinematic parameters of frequency and amplitude associated with body undulation or fin flapping [74, 76]. Since an evolutionary convergence of locomotory

strategies should be an ultimate solution to a tradeoff between the optimization of mechanical efficiency and the diminishment of energy expenditure limited by muscle capability, identifications for the ultimate propulsive strategy obeyed by bio-locomotors over a broad range of species and velocities remain still unexplored.

We unravel a universal mechanistic principle characterizing and unifying the wave phenomenon associated with swimming and flying by deriving a scaling law that correlates the transition of wave energy between transverse (lateral motion of undulating body and flapping wings) and longitudinal (forward movement of body) wave with energetic cost. A unique Wave Energy number (*We*) is proposed linking flight speed to wing kinematics (frequency and amplitude) as well as wing-to-body mass ratio (WBMR) and gravity. We introduce a versatile and high-fidelity CFD model which enables precise prediction of the aerodynamic forces and powers for forward flight of various flapping insects. A universal mechanistic principle obeyed by bio-locomotors has been uncovered through investigating the correlations between wave-based Wave Energy number (*We*) with the force-based Reynolds number (*Re*) and the motion-based Strouhal number (*St*) in biological flapping flights covering broad experimental observations of various species including insects, bats and birds. Furthermore, a systematic analysis on the performance landscapes predicted from realistic insects allow us to figure out whether some combination of flapping frequency and stroke amplitude can optimize flight-speed-specific Froude efficiency, Cost of Transport and Wave Energy number, and finally to identify which propulsive strategy is dominant in biological flights.

5.2 Wave Energy number

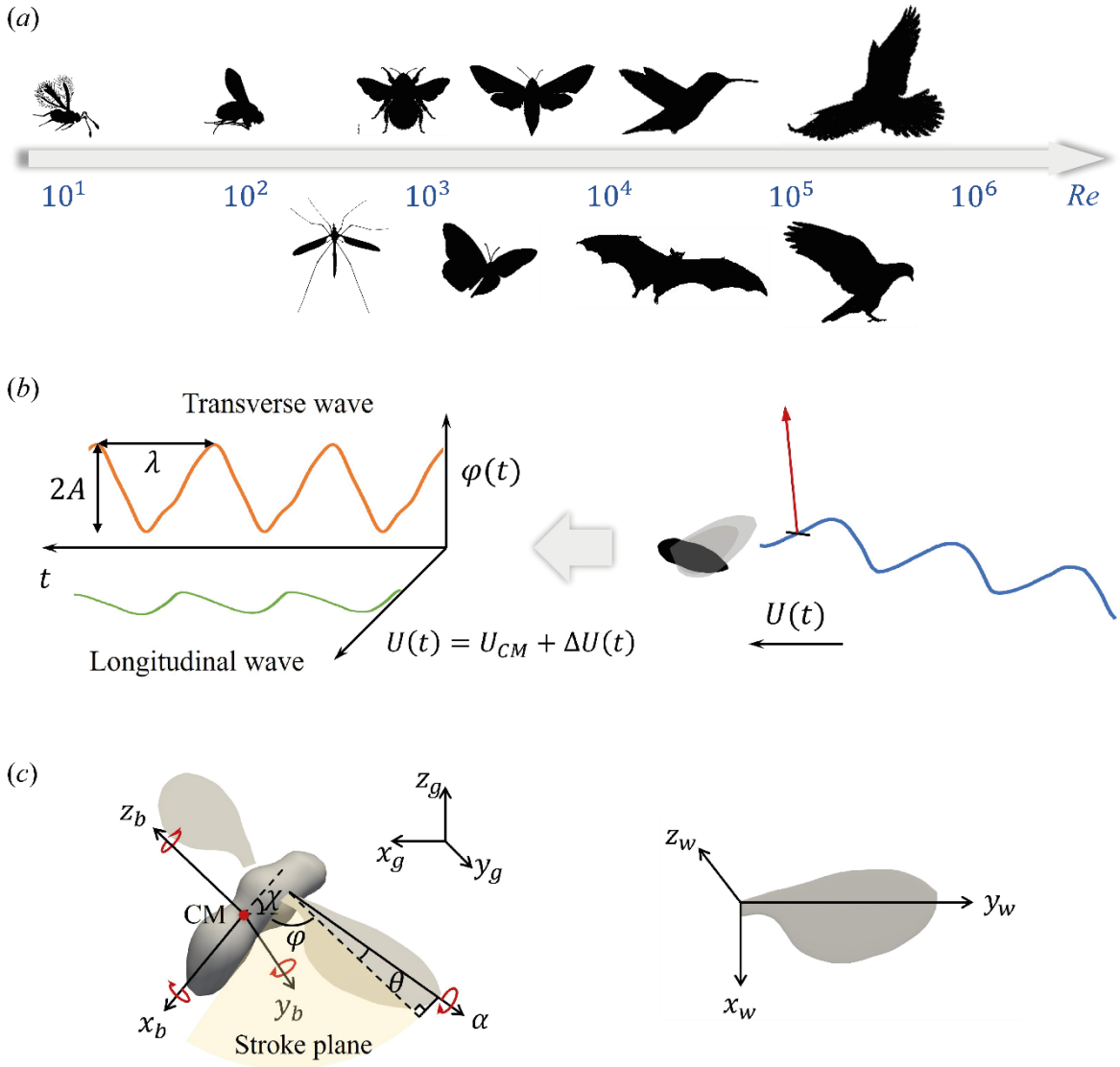

Fig. 5-1 Biological flapping flight in insects, bat and birds. (*a*) Insects, bats and birds fly over a broad range of *Re* encompassing wasp, fruit fly, crane fly, bumblebee, butterfly, hawkmoth, hummingbird, bat, pigeon and gyrfalcon. (*b*) Schematic representation of the wave phenomenon in flapping flights: transverse wave in flapping-wing kinematics (positional angle φ) and longitudinal wave in forward flight (speed) of a flying body. (*c*) Schematic of coordinate systems and wing-body kinematic parameters of a fruit fly model. High-fidelity CFD wing-body models of typical insects have been built up based on the realistic morphology and wing-body kinematics.

During forward flapping flight, both flapping wings and moving body of the flyers will generate waves, which can be divided into transverse and longitudinal components. The transverse wave generated by the flapping wing motion can be demonstrated as the kinetic energy K_{Tw} of the flapping wings for dual-wing flyers,

$$K_{Tw} = 2 \times \left(\frac{1}{2} m_w \omega^2 A^2\right) = m_w \omega^2 A^2, \quad (5-1)$$

where A is the amplitude, m_w is the wing mass and ω is the flapping wing angular velocity. The longitudinal wave caused by body's horizontal motion is served as the kinetic energy for forward movement

$$K_{Lb}^h = \frac{1}{T}\int_0^T \frac{1}{2} m_b U_h(t)^2 dt\,. \quad (5-2)$$

Here the horizontal velocity of the body is expressed as $U_h(t) = U_{CM-h} + \Delta U_h(t)$, where $\Delta U_h(t)$ is verified to be negligibly small than the cycle-averaged velocity U_{CM-h} (Fig. 5-2). Thus,

$$\begin{aligned} K_{Lb}^h &= \frac{1}{T}\int_0^T \frac{1}{2} m_b [U_{CM-h} + \Delta U_h(t)]^2 dt \\ &= \frac{m_b}{2T}\int_0^T \left[{U_{CM-h}}^2 + \Delta U_h(t)^2 + 2U_{CM-h}\Delta U_h(t)\right] dt \\ &\approx \frac{m_b}{2T}\int_0^T {U_{CM-h}}^2 dt = \frac{1}{2} m_b {U_{CM-h}}^2. \end{aligned} \quad (5-3)$$

The transverse wave caused by body's vertical motion can be described as the potential energy U_{Tb}^v and the kinetic energy K_{Tb}^v to stay airborne, such as

$$K_{Tb}^v = \frac{1}{T}\int_0^T \frac{1}{2} m_b U_v(t)^2 dt\,, \quad (5-4)$$

$$U_{Tb}^v = \frac{1}{T}\int_0^T m_b g H_v(t) dt\,. \quad (5-5)$$

Since the vertical velocity of the body $U_v(t) \ll U_h(t)$, the vertical kinetic energy K_{Tb}^v is negligible compared with the horizontal one K_{Lb}^h. Additionally, the vertical movement of

the body can be expressed as $H_v(t) = H_{CM-v} + \Delta H_v(t)$, where $\Delta H_v(t)$ is verified to be negligibly small than the cycle-averaged height H_{CM-v} (Fig. 5-2). Thus,

$$U_{Tb}^{v} = \frac{1}{T}\int_0^T m_b g[H_{CM-v} + \Delta H_v(t)]dt$$
$$\approx \frac{m_b g}{T}\int_0^T H_{CM-v}\,dt \;=\; m_b g H_{CM-v}. \qquad (5-6)$$

The total energy of body's motion can be calculated as

$$E_b = U_{Tb}^{v} + K_{Lb}^{h} = m_b g H_{CM-v} + \frac{1}{2} m_b {U_{CM-h}}^2. \qquad (5-7)$$

Considering that the transverse wave is caused by the actively flapping motions of wings, which demonstrates the total input kinetic energy of the power stroke, the longitudinal wave is a result of the transverse wave as it represents the effective output potential and kinetic energy to make the flyers stay airborne while moving forward. A new index Wave Energy number (*We*) for bio-flights is proposed as the ratio of energy output of body motion to energy input of flapping-wing motion, which is written by

$$We = \frac{E_b}{K_{Tw}} = \frac{U_{Tb}^{v} + K_{Lb}^{h}}{K_{Tw}}. \qquad (5-8)$$

Based on the Eq. 5-1 and Eq. 5-7, the amplitude can be calculated by the stroke amplitude $\emptyset$ and wing length R as $A = \frac{1}{2}\emptyset R$, and the angular velocity $\omega = 2\pi f$ can be scaled as flapping frequency f. With the assumption of flying height H_{CM-v} = 1m and $U_{CM-h} \approx U_{CM}$ for all flyers, the Wave Energy number (*We*) is finally written as two components

$$We^{v} = \frac{U_{Tb}^{v}}{K_{Tw}} = \frac{m_b g H_{CM-v}}{m_w \omega^2 A^2} \propto \frac{m_b g}{m_w f^2 A^2}, \qquad (5-9)$$

$$We^{h} = \frac{K_{Lb}^{h}}{K_{Tw}} = \frac{\frac{1}{2} m_b {U_{CM-h}}^2}{m_w \omega^2 A^2} \propto \frac{m_b {U_{CM}}^2}{m_w f^2 A^2}. \qquad (5-10)$$

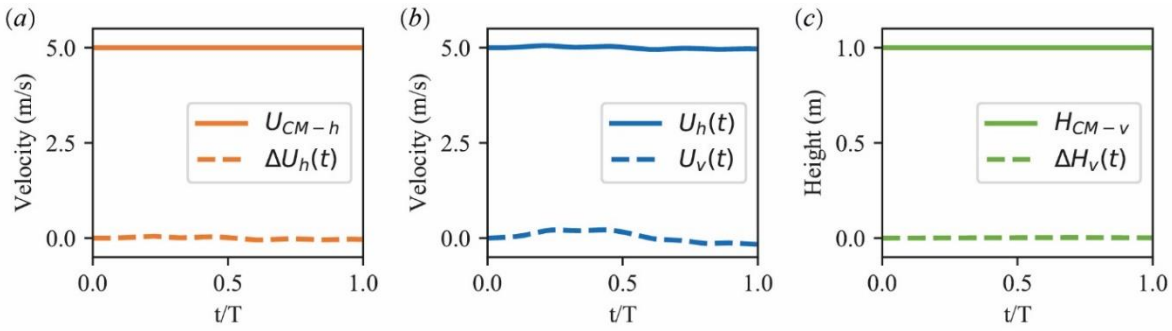

Fig. 5-2 Verification through CFD-based trimmed forward flight of hawkmoth that the flapping-induced transverse wave-based energy of body motion is negligibly small than the longitudinal wave-based one. $(a)\ \Delta U_h(t) \ll U_{CM-h}$; $(b)\ U_v(t) \ll U_h(t)$; $(c)\ \Delta H_v(t) \ll H_{CM-v}$.

Considering obtaining precise estimation of energetics in balanced condition, we further employ a method to modify the wing kinematics with intention of achieving trimmed flights of insect and bird models in various flight velocities. A genetic algorithm (GA) involving the covariance matrix adaptation-based derandomized evolution strategy (CMA-ES) [93, 94] is employed for finely tuning the wing kinematics, embedded with a CFD data-driven aerodynamic model (CDAM) by Cai *et al* [92]. Flow chart of the approach to determine trimmed flights are illustrated in detail in Xue *et al* [113].

5.3 Results

5.3.1 Wave-based scaling over broad Reynolds number regimes

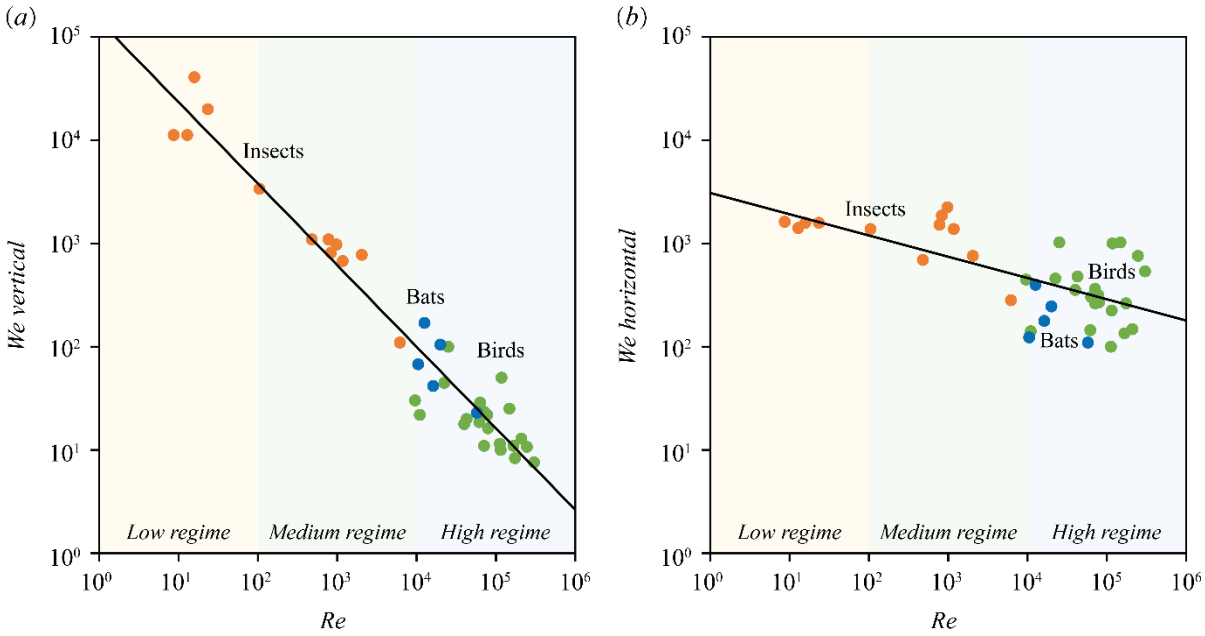

Fig. 5-3 Scaling biological flapping flights: correlations between Reynolds number (*Re*) and Wave Energy number (*We*) over a broad range of various species including insects, bats and birds at various flight speeds [4, 16, 17, 66, 99, 100, 115-122]. (*a*) The vertical component of Wave Energy number We^v; (*b*) the horizontal component of Wave Energy number We^h.

In Fig. 5-3, measurements show that the Wave Energy number (*We*) varies with the Reynolds number (*Re*) in biological flapping flights over a broad range of various species including insects, bats and birds. Compiled from a variety of experimental data with double logarithmic scales, the species vary in size from 0.0001 to 1 m with the Reynolds number (*Re*) varying from 10^1 to 10^6 (Table 5-1 lists the detailed kinematic and morphological parameters). It is noticeable that both vertical and horizontal components of Wave Energy number show significant decrease with higher *Re* (Fig. 5-3), which means the effective wave transition from energy input of flapping-wing motion to energy output of body motion experiences an enhancement along with the downsize of the bio-flyers

from large birds to small insects.

Table 5-1 Wing-body mass, flight velocity, stroke amplitude and flapping frequency, as well as wing length and mean chord length of 38 flapping insects, bats and birds.

Species	$\boldsymbol{m_b}(kg)$	$\boldsymbol{m_w}(kg)$	$\boldsymbol{U_f}(m/s)$	$\boldsymbol{f}(Hz)$	$\emptyset(rad)$	$\boldsymbol{R}(m)$	$\boldsymbol{c_m}(m)$
Paratuposa placentis	2.4E-09	2.4E-11	1.2	385.0	3.1	4.9E-04	1.1E-04
Encarsia formosa	1.9E-08	2.2E-10	1.1	361.0	2.5	6.1E-04	1.8E-04
Franklinella intonsa	6.1E-08	6.1E-10	0.6	254.0	2.4	5.0E-04	3.8E-04
Franklinella occidentalis	1.7E-08	1.7E-10	0.9	239.0	2.4	7.6E-04	3.9E-04
Drosophila melanogaster	2.0E-06	9.6E-09	2.0	200.0	2.6	3.0E-03	7.8E-04
Tipula paludosa	5.0E-05	4.7E-07	2.5	59.0	2.0	1.7E-02	2.9E-03
Eristalis tenax	9.5E-05	3.4E-07	3.7	172.0	1.7	1.1E-02	3.1E-03
Bibio marci	2.7E-05	1.5E-07	4.8	130.0	2.4	9.4E-03	2.6E-03
Calliphora vicina	6.2E-05	2.4E-07	4.8	152.0	2.3	9.2E-03	3.1E-03
Bombus terrestris	1.8E-04	9.0E-07	4.5	144.0	1.8	1.3E-02	3.9E-03
Sympetrum sanguineum	1.3E-04	2.8E-06	3.1	33.4	1.7	2.7E-02	1.0E-02
Manduca sexta	1.6E-03	9.4E-05	5.0	25.0	2.0	4.9E-02	1.8E-02
Glossophaga soricina1	1.2E-02	1.5E-03	4.2	11.8	1.5	1.2E-01	3.8E-02
Rhinolophus ferrumequinum1	9.8E-03	1.1E-03	4.8	10.0	1.1	1.3E-01	3.9E-02
Glossophaga soricina2	1.1E-02	1.4E-03	6.5	13.5	1.7	1.2E-01	3.7E-02
Rhinolophus ferrumequinum2	2.2E-02	2.5E-03	4.8	9.1	1.1	1.8E-01	6.2E-02
Macroderma gigas	1.3E-01	1.5E-02	6.9	7.0	1.5	3.8E-01	1.2E-01
Selasphorus rufus	3.4E-03	2.4E-04	12.0	41.7	2.2	4.7E-02	1.2E-02

Lampornis clemenciae	8.4E-03	5.9E-04	8.0	23.0	2.6	8.5E-02	2.1E-02
Taenopygia guttata	1.3E-02	1.1E-03	10.0	26.5	1.6	7.5E-02	3.3E-02
Delichon urbica	1.7E-02	1.9E-03	10.0	9.1	1.4	1.5E-01	3.8E-02
Hirundo rustica	1.6E-02	3.1E-03	14.0	9.0	2.4	1.6E-01	4.3E-02
Fringilla coelebs	2.0E-02	2.2E-03	15.3	18.2	2.0	1.2E-01	4.1E-02
Accipiter nisus	2.8E-01	4.5E-02	8.7	5.1	2.0	3.6E-01	1.1E-01
Larus ridibundus	2.6E-01	3.8E-02	10.1	3.3	2.0	4.6E-01	9.4E-02
Sturnus vulgaris	5.8E-02	7.4E-03	18.0	16.0	1.8	1.9E-01	5.9E-02
Corvus corone	3.3E-01	5.8E-02	10.5	4.0	2.0	3.9E-01	1.0E-01
Columba livia1	2.9E-01	4.5E-02	12.0	6.7	1.6	3.2E-01	9.7E-02
Colaptes auratus	1.3E-01	1.3E-02	12.7	9.2	2.2	2.6E-01	9.4E-02
Buteo buteo	7.7E-01	1.5E-01	9.3	3.6	2.0	5.9E-01	1.8E-01
Falco peregrinus	4.8E-01	6.8E-02	14.8	5.5	2.0	4.8E-01	1.2E-01
Pica pica	1.6E-01	1.3E-02	14.0	6.5	1.9	2.5E-01	1.3E-01
Columba livia2	3.2E-01	4.0E-02	20.0	5.8	2.2	2.8E-01	1.1E-01
Ardea cinerea	2.1E+00	3.3E-01	11.0	2.9	2.0	8.3E-01	2.2E-01
Falco rusticolus	9.9E-01	1.3E-01	17.6	5.3	2.0	5.9E-01	1.5E-01
Pandion haliaetus	1.1E+00	3.1E-01	10.6	3.3	2.0	5.0E-01	2.9E-01
Centrocercus urophasianus1	1.4E+00	6.6E-02	26.4	9.7	2.0	4.5E-01	1.4E-01
Centrocercus urophasianus2	2.5E+00	1.2E-01	26.4	9.7	2.0	5.4E-01	1.7E-01

Regressing *We* against *Re* shows that the vertical component of Wave Energy number

scales as $We^v \propto Re^{-0.8}$ (R^2 = 0.94) (Fig. 5-3 (*a*)) and the horizontal component of Wave Energy number scales roughly as $We^h \propto Re^{-0.2}$ (R^2 = 0.44) (Fig. 5-3 (*b*)), which is applicable over a broad range of fluid regimes for various biological flights. Gazzola *et al* [73] offer a drag-based explanation for aquatic locomotion scaling and classify laminar and turbulent regimes by different power laws of *Re*-*Sw*. However, the novel Wave Energy number provides a universal scaling relation unifying the fluid physics of animal locomotion covering all the low *Re* regime 10^0~10^2 (*i.e.* thrips, wasp and tiny beetle with bristled wings) where viscous force dominates the fluid drag, the medium *Re* regime 10^2~10^4 (*i.e.* fruit fly, hawkmoth and hummingbird) where both inertial and viscous force are the dominant, and the high *Re* regime 10^4~10^6 (*i.e.* bats and birds) where inertial force is the dominant. The wave energy transition stays higher at viscous force-dominated regime while operating a progressive reduction approaching inertial force-dominated regime, which may ascribe to the higher exploit efficiency needed for maintaining the lift-drag ratio for smaller flyers with limited wave energy input [4].

Difference in slopes between We^v and We^h indicates that the vertical transition to potential energy may be more sensitive to the fluid drag compared with the horizontal transition to kinetic energy. The proportion of vertical components We^v/We varies from 87% to 1% while the horizontal counterparts We^h/We accounts for 13% to 99% as *Re* increases from 10^1 to 10^6, demonstrating that bio-flyers intrinsically shift their energy output focus from staying airborne to moving faster in forward flights. Since the size of hovering insects is almost proportional to *Re* ($= \frac{c_m U_{CM-h}}{\nu}$) with double logarithmic scales [4, 11], here the mean chord length of bio-flyers is precisely verified as $c_m \propto Re^{0.7}$ (R^2 = 0.98) for various forward flight of insects, bats and birds (Fig. 5-4). With the constant kinematic viscosity ν, the forward flight velocity increases with higher *Re* and scales as $U_{CM-h} = \frac{\nu Re}{c_m} \propto Re^{0.3}$. Based on the definition of We^h and We^v in Eq. 5-9 and Eq. 5-10, the relative ratio between horizontal and vertical Wave Energy number can be scaled

as $We^h / We^v = \frac{U_{CM-h}{}^2}{gH_{CM-v}} \propto Re^{0.6}$ under the assumption of constant flying height H_{CM-v} and gravity g, which is consistent with the regression slopes in Fig. 5-3. We infer that the bio-fluid drag may play a significant role in the re-distribution of wave energy consumption among broad range of biological locomotion of insects, bats and birds.

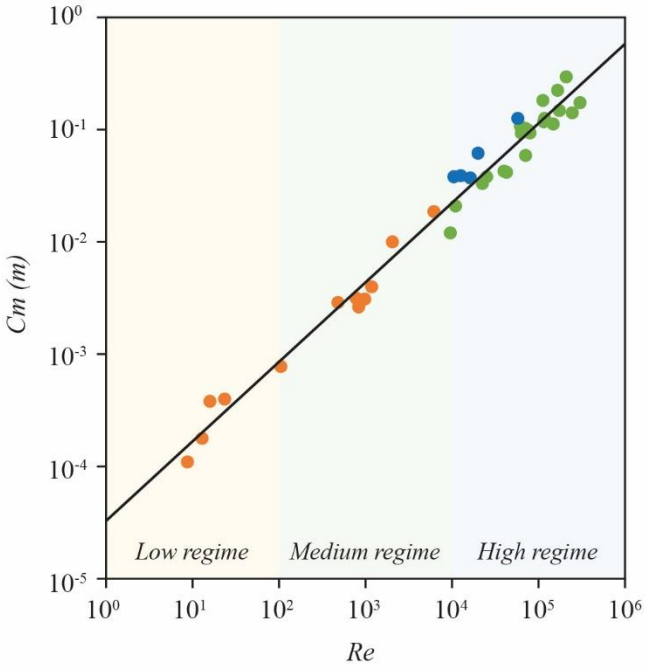

Fig. 5-4 Scaling biological flapping flights: correlations between Reynolds number (*Re*) and mean chord length of the wing (c_m) over a broad range of various species including insects (red), bats (blue) and birds (green) at various flight speeds ($c_m \propto Re^{0.7}$, R^2 = 0.98).

5.3.2 Wave-based scaling with motion-based Strouhal number

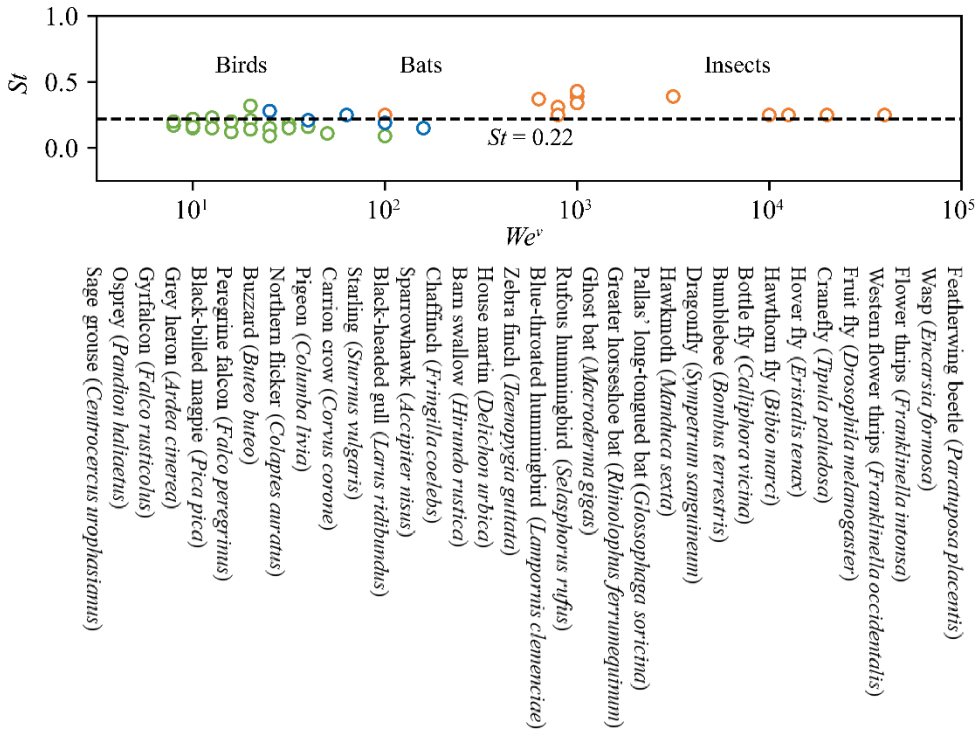

Fig. 5-5 Scaling biological flapping flights: correlations between Strouhal number (*St*) and Wave Energy number (*We*) over a broad range of various species including insects, bats and birds at various flight speeds [4, 16, 17, 66, 99, 100, 115-122].

The Strouhal number (*St*) is employed for characterizing the vortex dynamics in most locomotion studies [72, 73, 114]. For flapping flight, the *St* represnets the wing velocity with respect to the characteristic velocity [4], which is defined as

$$St = \frac{fL_{ref}}{U_{ref}} = \frac{fA}{U_f}, \qquad (5-11)$$

where the wingtip amplitude approximated as $A = \frac{1}{2}\emptyset R$ serves as the reference length L_{ref}, the forward velocity U_f is the reference velocity U_{ref}, and f is the flapping frequency. As depicted in Fig. 5-5, the Strouhal numbers for insects, bats and birds are commonly within a narrow region, in agreement with the universal findings of *St* tuned for high power efficiency in many cruising flying and swimming animals [72]. The wave

energy transition *We* seems to be operated with similar motion-based *St* at all the bio-fluid regimes. Since insects span at higher *We* than bats and birds (Fig. 5-3), we note that the mean value of *St* for insects (≈ 0.31) ranges slightly higher compared with those of bats (≈ 0.22) and birds (≈ 0.17) (Fig. 5-5). Similar phenomenon was also reported in aquatic locomotion scaling that a crossover exists from the laminar to the turbulent power law of *St*-*Re* [73]. Larger birds and bats have intrinsically lower *St*, as the very fast forward flight velocity affects *St* strongly with the constrained flapping frequency and amplitude by physiology and morphology [72]. Small flyers were reported to be more unsteady in their flight than large ones as the reduced frequency decreases with growing size and mass for a variety of birds and insects [4]. Considering that the wave energy transition *We* is comparatively low in most intermittent flight of birds and bats (Fig. 5-3), the underlying mechanism may lie in that the intermittent flight are helpful for minimizing the energy losses associated with vortex separation through lowering the Strouhal number [72].

Therefore, the novel Wave Energy number provides a universal scaling law covering all the bio-fluid regimes, that biological flights obey a specific *Re*-*We* principle ($We^{v} \propto Re^{-0.7}$, $We^{h} \propto Re^{-0.2}$) and the wave energy transition can be achieved within a narrow range of motion-based Strouhal number.

5.4 Ultimate propulsive strategy in bio-locomotion

According to the study on bio-swimming by Li *et al* [74], the two dimensionless indices η_{Fr} $(=\frac{\bar{T}\cdot V_f}{\bar{P}_{toto}})$ and CoT $(=\frac{\bar{P}_{toto}}{V_f \cdot m_b})$ are different in optimizing energetic performance. Here $\bar{T}$ denotes the cycle-averaged thrust predicted as the sum of positive components of aerodynamic forces acting on each surface element relative to the direction of the path of motion; V_f and $\bar{P}_{toto}$ are the forward flight velocity and time-averaged total mechanical power, respectively. They found fishes regulate tail-beat kinematics of amplitude and

frequency to minimize CoT rather than Froude mechanical efficiency [74]. With the intention of figuring out which energetic indices is the dominant for bio-flights and whether the flapping bio-flyers obey a rule to minimize energetic expenditure through adjusting the stroke frequency and amplitude at various flight speeds, we examine the three strategies including minimizing Cost of Transport *CoT*, maximizing Froude efficiency η_{Fr} and maximizing Wave Energy number *We*.

First, we build a parameter landscape for flapping frequency *f* and stroke amplitude Φ as a function of flight speed V_f through interpolation among several simulations with experimental kinematics. This performance map is determined by modifying the flight velocity of each flyer with the purpose of achieving trimmed flight for each combination of flapping frequency and amplitude. The corresponding Cost of Transport, Froude efficiency and Wave Energy number heatmaps in frequency and amplitude plane can be obtained by dozens of numerical simulations. Further, we apply the iso-velocity curves in three heatmaps to search for points corresponding to the minimum *CoT*, maximum η_{Fr} and maximum *We* respectively at each specific flight velocity [74]. Finally, the velocity-specific optimal trajectories representing the minimum *CoT* strategy, the maximum η_{Fr} strategy and the maximum *We* strategy are achieved for three typical insects, such as fruit fly (*Drosophila melanogaster*) [11, 33, 59, 101], bumblebee (*Bombus terrestris*) [34, 66, 102] and hawkmoth (*Manduca Sexta*) [18, 113].

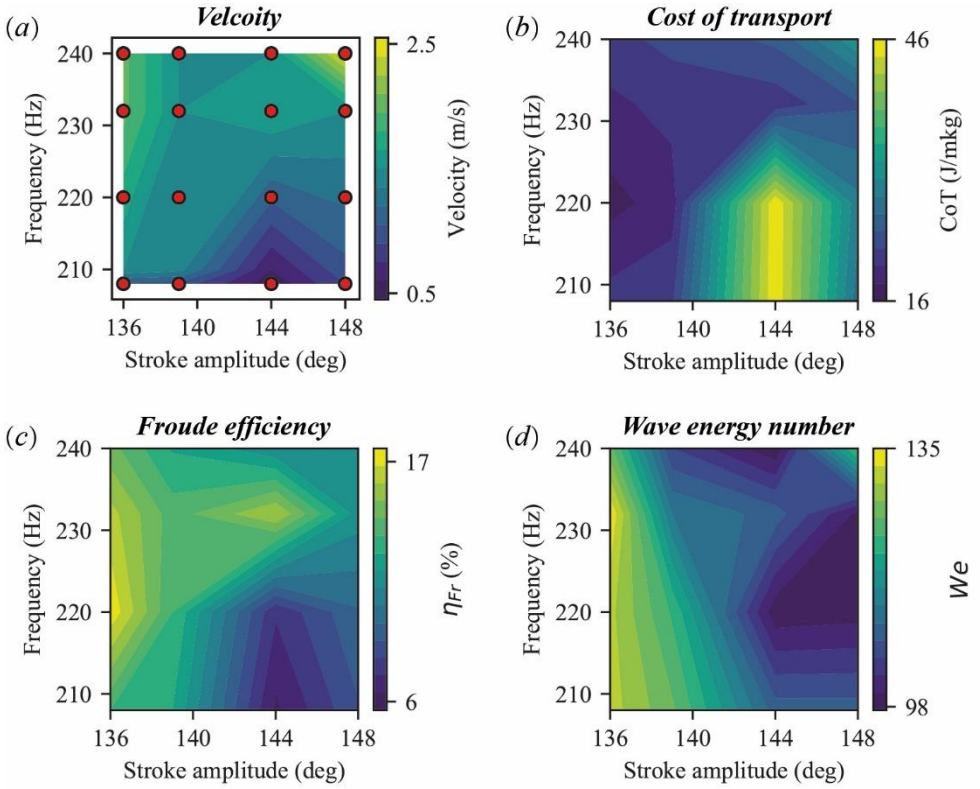

Fig. 5-6 Performance heatmap as a function of stroke amplitude and flapping frequency for a simulated fruit fly. (*a*) Flight velocity based on CFD simulations (Red circles); (*b*) Cost of Transport (*CoT*); (*c*) Froude mechanical efficiency (η_{Fr}); (*d*) Wave Energy number (*We*).

Detailed morphological and kinematic models in various flight velocities, as well as the exploration details of all optimal curves can be found as following. For each insect, we first achieve the trimmed flights through genetic algorithm (GA) based on experimental wing kinematics over a broad range of forward flight velocities. Since each flight velocity corresponds to certain flapping frequency and stroke amplitude in trimmed flights, we consider the flight velocity as functions of frequency and amplitude, and further obtain new predicted velocity for each combination of f and A through interpolation, such as V_{ij} ~ (f_i, A_j), *i.e.* i, j=1~4, maximum and minimum f , A are determined according to the trimmed cases. These predicted V_{ij} will be verified through input a set of [f_i, A_j, V_{ij}] into the CFD simulations (*i.e.* 4×4=16 cases). If one set of [f_i, A_j, V_{ij}] does not satisfy the trim conditions,

we modify the flight velocity to test new combination $V_{new,\ ij}$ ~ (f_i, A_j) through CFD simulation. Finally, all the simulation-based points (*i.e.* 4×4=16 cases) determined for generating the performance map are verified to achieve trimmed forward flights (Fig. 5-6 (*a*), Fig. 5-7 (*a*) and Fig. 5-8 (*a*)).

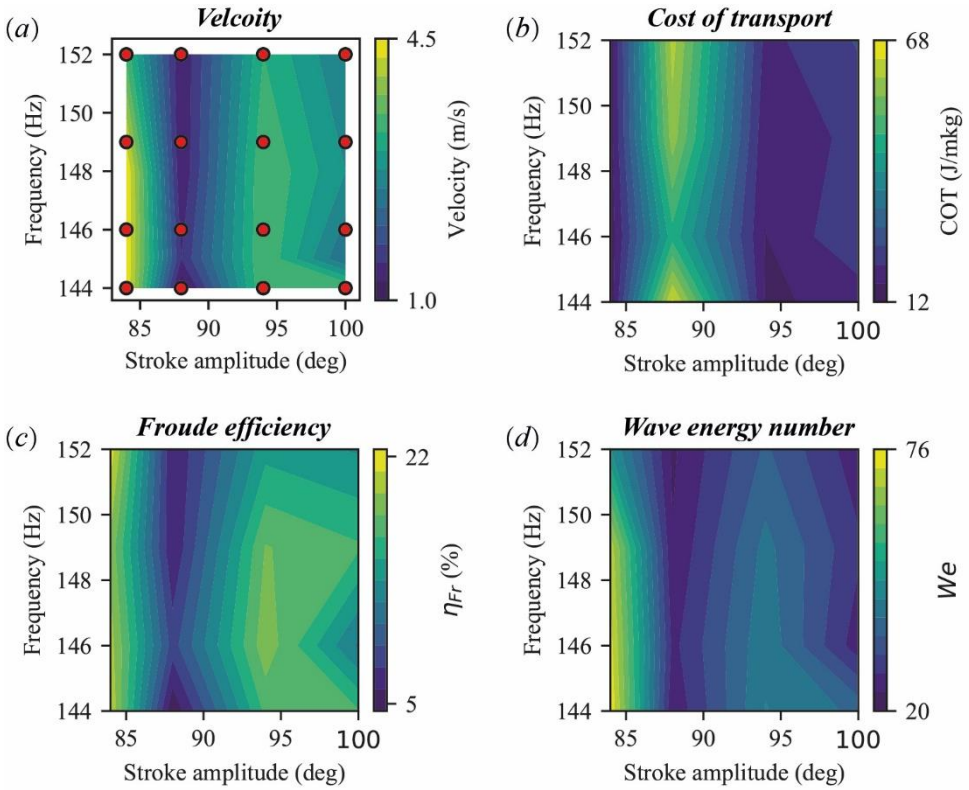

Fig. 5-7 Performance heatmap as a function of stroke amplitude and flapping frequency for a simulated bumblebee. (*a*) Flight velocity based on CFD simulations (Red circles); (*b*) Cost of Transport (*CoT*); (*c*) Froude mechanical efficiency (η_{Fr}); (*d*) Wave Energy number (*We*).

The corresponding Cost of Transport, Froude efficiency and Wave Energy number heatmaps in frequency and amplitude plane can be obtained by dozens of numerical simulations (Fig. 5-6 (*b,c,d*), Fig. 5-7 (*b,c,d*) and Fig. 5-8 (*b,c,d*)). Further, we apply the iso-velocity curves in three heatmaps to search for points corresponding to the minimum *CoT*, maximum η_{Fr} and maximum *We* respectively at each specific flight velocity based on the searching process of Li *et al*. Finally, the velocity-specific optimal trajectories

representing the minimum *CoT* strategy, the maximum η_{Fr} strategy and the maximum *We* strategy are achieved for three typical insects.

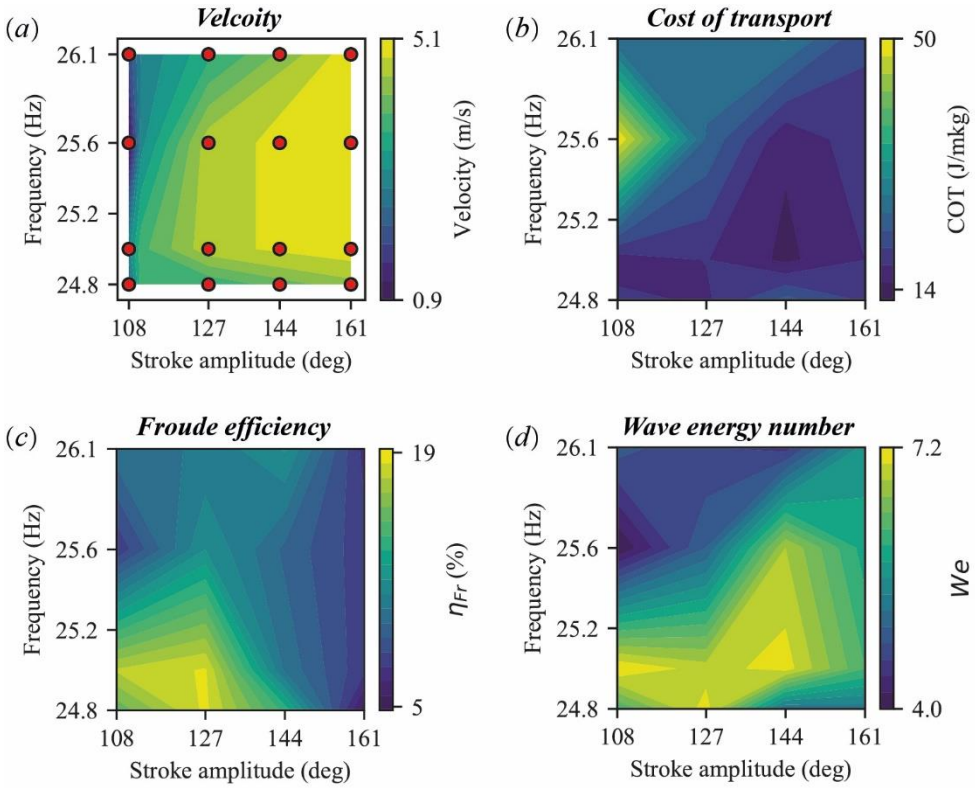

Fig. 5-8 Performance heatmap as a function of stroke amplitude and flapping frequency for a simulated hawk moth. (*a*) Flight velocity based on CFD simulations (Red circles); (*b*) Cost of Transport (*CoT*); (*c*) Froude mechanical efficiency (η_{Fr}); (*d*) Wave Energy number (*We*).

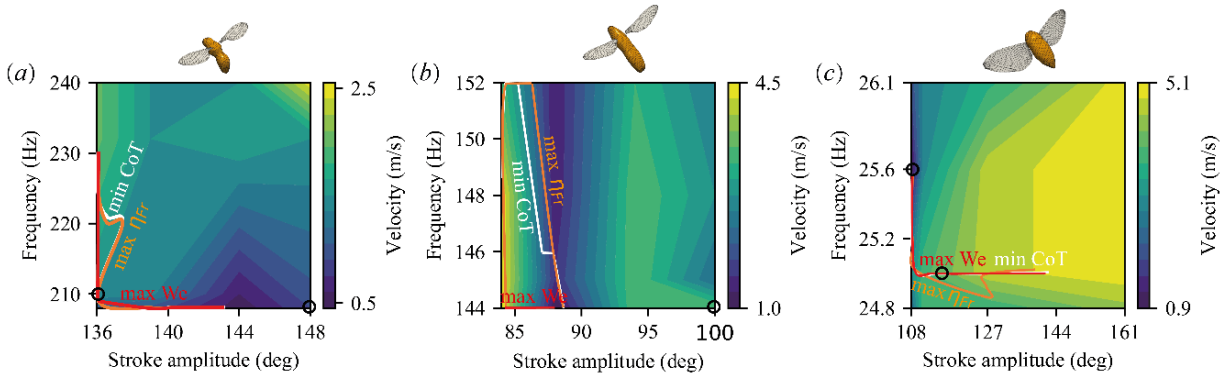

Fig. 5-9 CFD-based velocity-specific minimum Cost of transport (*CoT*) trajectory (white line), maximum Froude efficiency (η_{Fr}) curve (orange line) and maximum Wave Energy number (*We*) curve (red line) superimposed and compared on the heatmap of flight velocity as a function of flapping frequency and amplitude for (*a*) the fruit fly, (*b*) the bumblebee as well as (*c*) the hawk moth, validated by some measurement-based experimental observations (black circles).

The CFD-based performance maps show that flapping frequency generally increases with higher flight velocity of fruit fly while the stroke amplitude is highly correlated with the flight velocity in bumblebee and hawkmoth trimmed forward flight. For fruit fly, all three energetic strategies predict a reduction in stroke amplitude at low flight speed while raising the flapping frequency almost vertically as the flight velocity becomes higher (Fig. 5-9 (*a*)), indicating that varying frequency while keeping amplitude within a narrow range may control the energetic performance at fast forward flight. However, although coincided with the minimum *CoT* curve and maximum η_{Fr} curve in slow forward flight, the maximum *We* strategy is found to require the least stroke amplitude to maintain high velocity in fruit fly forward flight (Fig. 5-9 (*a*)). It is also noticed in bumblebee and hawkmoth forward flights (Fig. 5-9 (*b, c*)) that larger stroke amplitude is apparently needed for maximum η_{Fr} strategy at specific flight velocities compared with minimum *CoT* strategy and maximum *We* strategy. Similar phenomenon has been found in fish swimming as the minimum *CoT* strategy limits amplitude but the maximum η_{Fr} strategy will not [74], which can further be explained as preventing excessive energy consumption

by optimizing kinematics to limit drag. Moreover, the maximum *We* strategy shows significantly lower flapping frequency for most of the flight velocities of bumblebee than the minimum *CoT* strategy and the maximum η_{Fr} strategy (Fig. 5-9 (*b*)). The maximum *We* strategy offers a path with lower preference in both flapping frequency and amplitude for three insects, implying that insects are likely to maximize the Wave Energy number rather than minimize the cost of transport and maximize the Froude efficiency.

Comparing the CFD-based predictions with experimental measurements suggest that three strategies show a close match with the realistic forward flights of insects (Fig. 5-9 (*a, c*)). It is remarkable that the measurement-based points lie closer to the maximum *We* trajectory than the minimum *CoT* strategy and the maximum η_{Fr} strategy (Fig. 5-9 (*c*)). This further demonstrates our previous conjecture that biological flapping flyers can regulate their wing-beat amplitude and frequency with increasing flight velocity to achieve the maximum speed-specific wave energy expenditure. Since an evolutionary convergence of locomotory strategies should be an ultimate solution to a tradeoff between the optimization of mechanical efficiency and the diminishment of energy expenditure limited by muscle capability, we infer that the wave phenomenon in bio-locomotion is an ultimate propulsive strategy as a consequence of evolution in nature.

5.5 Concluding remarks

A universal mechanistic principle characterizing and unifying the wave phenomenon in biological flapping flights has been unraveled over a variety of species including insects, bats and birds at various flight speeds. The novel Wave Energy number (*We*) representing the transition of wave energy between transverse and longitudinal wave provides a universal scaling law that biological flights obey a specific *Re*-*We* principle ($We^v \propto Re^{-0.7}$, $We^h \propto Re^{-0.2}$) covering all the bio-fluid regimes and the wave energy transition is achieved within a narrow range of Strouhal number (*St*). Our findings further point to an

important mechanism that bio-flyers may prefer to maximize the flight-speed-specific *We* via regulating stroke frequency and amplitude, which further demonstrates that the wave phenomenon in bio-locomotion is an ultimate propulsive strategy as consequence of evolution in nature.

Chapter 6 Deep reinforcement learning (DRL) controller for insect-inspired flight systems

6.1 Introduction

Flapping insects enable outperforming stability and maneuverability under a wide array of extreme disturbances such as wind gusts and turbulences. Although the small insect body is susceptible even by gentle disturbance, flapping-wing insects are able to restore large deviations through continuous adjustments on wing kinematics within several wing-beat strokes [123, 124, 125]. Insect flight control system is a highly integrated, closed-loop system [5], in which the nonlinear dynamic system couples the motion equations for body dynamics and the Navier-Stokes equations for unsteady aerodynamics and [8]. The nonlinear control strategy required for dealing with the insect flight stabilization in case of large perturbations in full degrees of freedom are still limited for controller design.

Conventional proportional-derivative (PD) controller [123, 124, 125] has been widely adapted for insect-inspired flight control system. The linear PD control strategy is demonstrated as significantly efficient tool for 1-DoF control under small perturbations [124, 125, 126, 127], as well as 3-DoF control for body attitudes [128] and longitudinal motions [92] in insect hovering flight. It is also suggested to be feasible for bumblebee flight control under both small and large perturbations in full 6 degrees of freedom [129], in which the adjustment on control parameters of proportional and derivative gains can be obtained based on a CFD data-driven aerodynamic model (CDAM) and a simplified flight dynamic model. However, since the correlation between aerodynamic forces, torques and wing kinematics manipulation [130, 131] may not be linear for some extreme conditions,

and the optimal PD control parameters tailored to various complex tasks may be quite different and require re-implementation, a more feasible option of bio-inspired intelligence controller designed for large disturbance conditions based on autonomous deep reinforcement learning algorithm need to be extensively studied.

Flying animals tend to develop their control skills via randomly trial-and-error evolutionary process, which is consistent with the reinforcement learning (RL) [132] process to work out which behavior interacting with the environment will maximize the rewards. Due to the nonlinear motions and continuous action-state spaces for biomimetic aerial vehicles, deep reinforcement learning (DRL) controller is proven to give solutions for severe disturbances conditions and complex maneuvering tasks. Bøhn *et al* [133] achieved the attitude control on fixed-wing UAV using the deep reinforcement learning method of on-policy proximal policy optimization (PPO). Fei *et al* [134] presented a deep reinforcement learning control strategy trained by off-policy deep deterministic policy gradient (DDPG) and achieved goal-directed maneuvering for flapping-wing MAVs. Other challenging fields from games to robotics have employed a variety of state-of-art RL algorithms, such as on-policy learning requiring new collected samples for every policy updating: trust region policy optimization (TRPO) [135], proximal policy optimization (PPO) [136] and A3C [137], and off-policy learning re-utilizing the past exploration experience: DDPG [138], twin delayed deep deterministic policy gradient (TD3) [139] and soft actor-critic (SAC) [140]. Haarnoja *et al* [141] developed the SAC algorithm embedded with an automatic gradient-based temperature tuning method, which could achieve better performance without hyperparameter tuning for various tasks compared with other on-policy and off-policy algorithms. Whether the insect-inspired wing kinematics-based flight control strategy could be combined with deep reinforcement learning tasked with achieving fast control for 6-DoF flight stabilization even under large perturbations remains a challenge requiring further solution.

Here we propose a novel wing kinematics-based controller optimized by deep reinforcement learning (DRL) for bumblebee hovering stabilization under large perturbations. We establish a high-fidelity Open AI Gym environment through coupling a CFD data-driven aerodynamic model and a 6-DoF flight dynamic model. The control policy with action space of 4 is optimized by Soft Actor-Critic (SAC) algorithm with automating entropy adjustment. The benchmark tests are conducted to examine whether our wing kinematics-based DRL control strategy is capable of achieving fast stabilization under full 6-DoF large disturbances for bumblebee hovering, and further providing an efficient autonomous controller design for bio-inspired flapping-wing MAVs.

6.2 Methods

6.2.1 Morphological and kinematic bumblebee models

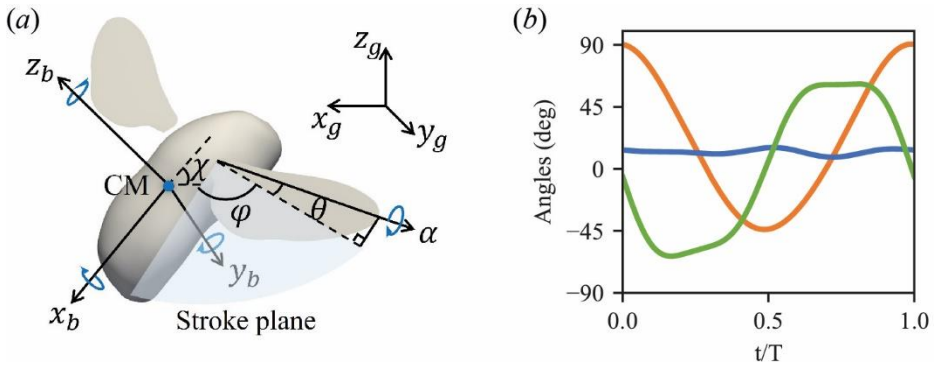

Fig. 6-1 Morphology and kinematics of bumblebee (*Bombus terrestris*) model. (*a*) Schematic of kinematic parameters defined in a global (x_g, y_g, z_g) and a body-fixed (x_b, y_b, z_b) coordinate systems. The yaw angle ψ, pitch angle χ and roll angle ρ of insect's body are determined along the body axis of z_b, y_b and x_b, respectively. (*b*) Wing kinematics of bumblebee in hovering flight are based on the experimental observations from Kolomenskiy *et al* [102], where the positional angle φ (red), elevation angle θ (blue) and feathering angle α (green) are expressed in Fourier series.

The bumblebee (*Bombus terrestris*) wing-body model is depicted in Fig. 6-1 (*a*), whose body mass m_b is 391 mg, mean chord length c_m is 4.1 mm, wing length *R* is 15.2

mm and body length L is 21 mm. The wing kinematics model of a hovering bumblebee is built according to the experimental observations of Kolomenskiy *et al* [102], which is defined by the three angles expressed as the first three terms of a Fourier series with respect to the stroke plane (Fig. 6-1 (*b*)): the positional angle φ, the elevation angle θ and the feathering angle α. The initial stroke amplitude Φ equals to 139.36° and the wing beat frequency f for bumblebee hovering flight is 136 Hz. The stroke plane angle β is 0° with the initial body angle χ equals 45° for hovering flight of bumblebee. For the rigid moving body, it is determined as three yaw ψ, pitch χ, roll ρ body angles, in which the pitch angle χ is determined as the body inclination angle with the horizontal plane, the yaw angle represents the rotational angle along body axis of z_b, and the roll angle ρ denotes the rotational angle along body axis of x_b.

6.2.2 Aerodynamic and flight dynamic models for hovering flight

We construct a control environment in the framework of Open AI Gym to achieve realistic hovering flight of bumblebee and provide fast response during deep reinforcement learning. A CFD data-driven aerodynamic model (CDAM) by Cai *et al* [92] is employed for fast prediction on aerodynamic forces and torques, combined with a flight dynamic model based on Cai and Liu [129] for mimic extreme motions under large perturbations. The CDAM consists of a CFD-informed quasi steady model based on blade element method for flapping wings and a simplified quasi-steady approximation-based aerodynamic model for a moving body [92], which is a better alternative to the time-consuming CFD simulations. The flight dynamic model of bumblebee applicable to large deviations is built by deriving the full dynamic equations extended from Gebert *et al* [142] and Sun *et al* [143]. The flight dynamic model is able to mimic the bumblebee wing-body interactions, where the wing kinematics are served as inputs and the insect's motion could be solved in a fast and precise manner. The dynamic equations of insect's moving body are determined as,

$$\begin{bmatrix} m_b + a_{1v} & A_{1o} & B_{1wR} & B_{1wL} \\ A_{2vR} + A_{2vL} & I_{bd} + A_{2oR} + A_{2oL} & B_{2wR} & B_{2wL} \end{bmatrix} \frac{\mathrm{d}}{\mathrm{d}t} \begin{bmatrix} {}_b\boldsymbol{v}_{cg} \\ {}_b\boldsymbol{\omega}_{bd} \\ \boldsymbol{\omega}_{R0b} \\ \boldsymbol{\omega}_{L0b} \end{bmatrix}$$

$$= \begin{bmatrix} {}_bF_{a,bd} + {}_bF_{a,R} + {}_bF_{a,L} + m_b\,{}_bg - m_b\,{}_b\omega_{bd} \times {}_bv_{cg} - a_1 - b_1 \\ {}_bM_{a,bd} + {}_bM_{a,R} + {}_bM_{a,L} - {}_b\omega_{bd} \times \left(I_{bd}\,{}_b\omega_{bd}\right) - (a_{2R} + a_{2L}) - (b_{2R} + b_{2L}) \end{bmatrix}, (6-1)$$

where ${}_bF_{a,bd}$, ${}_bF_{a,R}$, ${}_bF_{a,L}$, ${}_bM_{a,bd}$, ${}_bM_{a,R}$, ${}_bM_{a,L}$ calculated via CDAM denote the aerodynamic forces as well as torques on body and two wings. The flapping-wing dynamic equations are written as,

$$\begin{bmatrix} A_{2vR} + C_{vR} & A_{2oR} - C_{oR} & B_{2wR} - C_{wR} & 0 \\ A_{2vL} + C_{vL} & A_{2oL} - C_{oL} & 0 & B_{2wL} - C_{wL} \end{bmatrix} \frac{\mathrm{d}}{\mathrm{d}t} \begin{bmatrix} {}_b\boldsymbol{v}_{cg} \\ {}_b\boldsymbol{\omega}_{bd} \\ \boldsymbol{\omega}_{R0b} \\ \boldsymbol{\omega}_{L0b} \end{bmatrix} - \begin{bmatrix} M_{b2R} \\ M_{b2L} \end{bmatrix}$$

$$= \begin{bmatrix} {}_bM_{a,R} - a_{2R} - b_{2R} + c_R \\ {}_bM_{a,L} - a_{2L} - b_{2L} + c_L \end{bmatrix}, \quad (6-2)$$

where M_{b2R} and M_{b2L} denote the torques because of the wing-body interactions. We further apply two equations by adding the wing kinematics-based control inputs,

$$\dot{E}^{-1}_{dEulerR2sp} E'_{spR2b} \boldsymbol{\omega}_{R0b} + E^{-1}_{dEulerR2sp} E'_{spR2b} \frac{d\boldsymbol{\omega}_{R0b}}{dt} = \begin{pmatrix} \ddot{\varphi}_R \\ \ddot{\theta}_R \\ \ddot{\eta}_R \end{pmatrix}, \quad (6-3)$$

$$\dot{E}^{-1}_{dEulerL2sp} E'_{spL2b} \boldsymbol{\omega}_{L0b} + E^{-1}_{dEulerL2sp} E'_{spL2b} \frac{d\boldsymbol{\omega}_{L0b}}{dt} = \begin{pmatrix} \ddot{\varphi}_L \\ \ddot{\theta}_L \\ \ddot{\eta}_L \end{pmatrix}. \quad (6-4)$$

By integrating equations Eq. 6-1 ~ Eq. 6-4, the bumblebee motion could be solved. Detailed coefficients in dynamic equations for the body and two wings can be found in Cai and Liu [129].

6.2.3 Wing kinematics-based controller design

Cai and Liu [129] proposed a 6-DoF proportional-derivative (PD) control strategy through directly tuning four wing kinematics parameters for bumblebee flight stabilization, leaving the *x* and *y* positions controlled indirectly by modifying the pitch and roll angles.

Our controller design also selects four typical wing kinematics parameters to be served as the action space for deep reinforcement learning, and the aerodynamic torques and forces induced through wing kinematics variations are depicted in Fig. 6-2: symmetric stroke amplitude variation $\Delta\emptyset$ will cause pitch torque T_y and vertical forces F_z; symmetric mean positional angle variation $\Delta\bar{\varphi}$ may generate pitch torque T_y; asymmetric stroke amplitude variation $\Delta\emptyset_{RL}$ and asymmetric mean feathering angle variation $\Delta\bar{\alpha}_{RL}$ between left and right wings could induce yaw T_z and roll torques T_x.

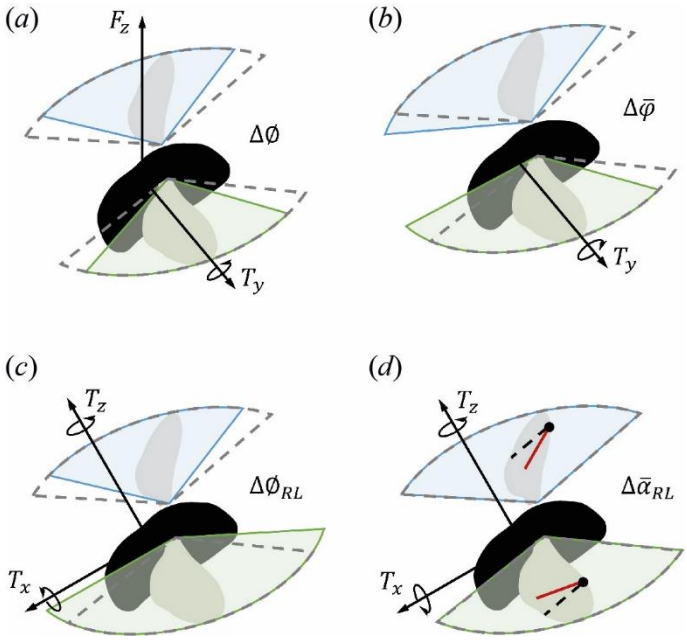

Fig. 6-2 Aerodynamic forces and torques induced through wing kinematics variations: (*a*) symmetric stroke amplitude variation $\Delta\emptyset$; (*b*) symmetric mean positional angle variation $\Delta\bar{\varphi}$; (*c*) asymmetric stroke amplitude variation between right and left wings $\Delta\emptyset_{RL}$; (*d*) asymmetric mean feathering angle variation between left and right wings $\Delta\bar{\alpha}_{RL}$. Dotted region: initial wing motion for trimmed hovering flight; shaded region with solid line: manipulated wing kinematics.

Here we propose a deep reinforcement learning (RL) policy for insect-inspired flight control systems with the intention of achieving the bumblebee hovering stabilization under large perturbations. The bumblebee behaviors are served as Markov decision process (MDP) in continuous control. We build a state space $s_t = [\psi,\ \chi,\ \rho,\ \dot{\psi},\ \dot{\chi},\ \dot{\rho},\ x,\ y,\ z,\ \dot{x},$

$\dot{y},\ \dot{z}]^T$ with a dimension of 12 to observe the angular position, angular velocity, position and velocity of insect, and an action space $a_t = [\Delta\emptyset,\ \Delta\bar{\varphi},\ \Delta\emptyset_{RL},\ \Delta\bar{\alpha}_{RL}]^T$ with a dimension of 4 to provide a continuous manipulation on the wing kinematics of bumblebee. Fig. 6-3 illustrates the schematic diagram of the wing kinematics-based bumblebee flight control system, where deep reinforcement learning gives solutions for controller design. The state transition for generating s_{t+1} can be achieved through our bumblebee environment based on the closed-loop flight dynamic model with feedback controller.

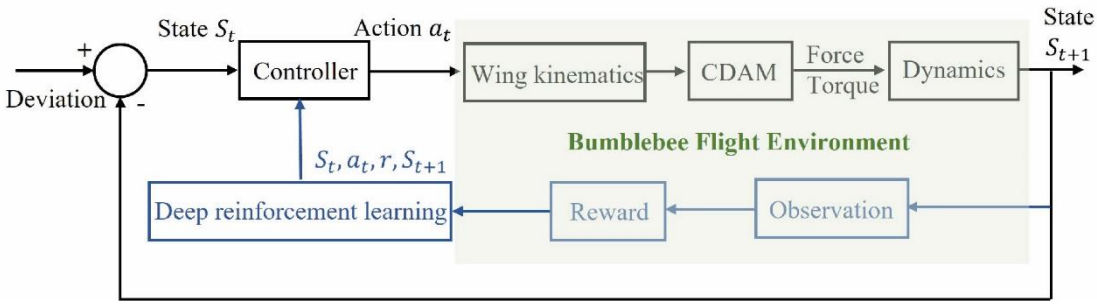

Fig. 6-3 Schematic diagram of the wing kinematics-based bumblebee flight control system, where deep reinforcement learning gives solutions for controller design.

Since our flight control system requires continuous manipulation and updated strategy at the beginning of each wing-beat stroke, we choose the popular off-policy actor-critic algorithm based on the maximum entropy RL framework, Soft Actor-Critic (SAC) to train the policy [141]. There are three key components in SAC algorithm: separate policy and value function-based actor-critic networks, high-efficiency data-reusing off-policy formulation, as well as stability and exploration-encouraging entropy maximization. The state value function is written as

$$V(s_t) = \mathbb{E}_{a_t \sim \pi}[Q(s_t, a_t) - \alpha \log \pi(a_t|s_t)], \qquad (6-5)$$

Thus, the Q value function based on soft Bellman equation [140, 141] is given by

$$Q(s_t, a_t) = r(s_t, a_t) + \gamma \mathbb{E}_{s_{t+1}, a_{t+1}}[Q(s_{t+1}, a_{t+1}) - \alpha \log \pi(a_{t+1}|s_{t+1})], \qquad (6-6)$$

where r is the one-step reward, $\mathbb{E}$ denotes the mathematical expectation, γ is the

discount factor, and π is the adopted policy. Here, α controls how important the entropy term is, known as temperature parameter. The SAC updates the policy to minimize the Kullback-Leibler (KL) divergence [140, 141],

$$\pi_{new} = arg\min_{\pi' \in \Pi} D_{KL}\left(\pi'(\cdot|s_t) \middle\| \frac{\exp\left(\frac{1}{\alpha} Q^{\pi_{old}}(s_t,\cdot)\right)}{Z^{\pi_{old}}(s_t)}\right), \quad (6-7)$$

where Π denotes the family of Gaussian distributions, and Z represemts the partition function for distribution normalization. The parameters of soft Q-function θ is trained to by [140, 141],

$$J_Q(\theta) = \mathbb{E}_{(s_t,a_t)\sim\mathcal{D}}\left[\frac{1}{2}\left(Q_\theta(s_t,a_t) - \left(r(s_t,a_t) + \gamma \mathbb{E}_{s_{t+1},a_{t+1}}[V_{\bar{\theta}}(s_{t+1})]\right)\right)^2\right], \quad (6-8)$$

where $\mathcal{D}$ is the replay buffer storing the transitions tuple $[s_t, a_t, r, s_{t+1}]$. A soft update is performed in target value network,

$$\bar{\theta} \leftarrow \tau\theta + (1-\tau)\bar{\theta}, \quad (6-9)$$

where τ denotes the step factor, and $\bar{\theta}$ is an exponentially moving average of the weights. And the policy network with parameter ϕ is updated by [140, 141],

$$\begin{aligned} J_\pi(\phi) &= \nabla_\theta D_{KL}\left(\pi_\phi(\cdot|s_{t+1}) \middle\| \exp\left(\frac{1}{\alpha} Q_\theta(s_t,\cdot) - \log Z_\theta(s_t)\right)\right) \\ &= \mathbb{E}_{a_t\sim\pi}\left[\log \pi_\phi(a_t|s_t) - Q_\theta(s_t,a_t) + \log Z_\theta(s_t)\right]. \end{aligned} \quad (6-10)$$

Since a sub-optimal temperature may cause poor performance in maximum entropy RL [140], a constrained formulation for automatically tuning the temperature hyperparameter has been employed in SAC without the requirement for hyperparameter tuning in every task. The optimal temperature parameter α in every step can be learned by minimizing the same objective function [140, 141],

$$J(\alpha) = \mathbb{E}_{a_t\sim\pi_t}[-\alpha \log \pi_t(a_t|s_t) - \alpha\mathcal{H}_0], \quad (11)$$

where $\mathcal{H}_0$ is the desired minimum expected entropy. The Soft Actor-Critic (SAC) with automating entropy adjustment has been evaluated through a variety of benchmark and real-world tasks of robotics [141], which could achieve outstanding asymptotic

performance and sample-efficiency compared with other off-policy and on-policy algorithms [135, 136, 137, 138, 139].

6.3 Results and discussion

6.3.1 Deep reinforcement learning policy

Since the goal of bumblebee flight control systems is to restore body angular position and position to the initial equilibrium state after large angular velocity or velocity perturbations via several strokes controlling. The reward design is determined as a negative cost function composed of stability cost and control cost, such as

$$Reward = -\left(\lambda_p {e_p}^2 + \lambda_v {e_v}^2 + \lambda_R {e_R}^2 + \lambda_\omega {e_\omega}^2 + \lambda_a {a_t}^2 + \lambda_a {\dot{a}_t}^2\right). \quad (6-12)$$

The stability cost is defined as the errors between current states and target states, where e_p denotes the position errors of $\Delta x,\ \Delta y,\ \Delta z$; e_v denotes the velocity errors of $\Delta \dot{x},\ \Delta \dot{y},\ \Delta \dot{z}$; e_R denotes the attitude errors of $\Delta \psi,\ \Delta \chi,\ \Delta \rho$; e_ω denotes the angular velocity errors of $\Delta \dot{\psi},\ \Delta \dot{\chi},\ \Delta \dot{\rho}$. The action cost a_t and action changing rate $\dot{a}_t$ are also included in reward design as control cost for ensure the stable wing kinematics and equilibrium state in trimmed hovering flight of bumblebee. As all the quantities of time, length, velocity, mass, force and torque are expressed in a dimensionless form, the scaling factors are determined by nondimensional magnitude of each composition to ensure the equivalent return for each error cost, such as

$$\lambda_p : \lambda_v : \lambda_R : \lambda_\omega : \lambda_a : \lambda_a = 10^0 : 10^4 : 10^0 : 10^4 : 10^0 : 10^0. \quad (6-13)$$

Considering the realistic morphology and kinematics of insects, we set the limitations of action space, such as maximum rising in stroke amplitude for 20% or maximum deviation in mean positional and feathering angle for 20 deg to avoid overlapping of two wings. We also modify the hyperparameters based on Haarnoja *et al* [141] and utilize several tricks such as reward scale incorporated with SAC to improve the training

robustness. Training process illustrated by learning curve with obtained reward at the end of each exploration episode is shown in Fig. 6-4. The accumulated negative reward could converge to highest, which is close to zero after randomly giving deviations at the beginning of each episode and exploring actions for 5000 steps (50 flapping strokes for each episode).

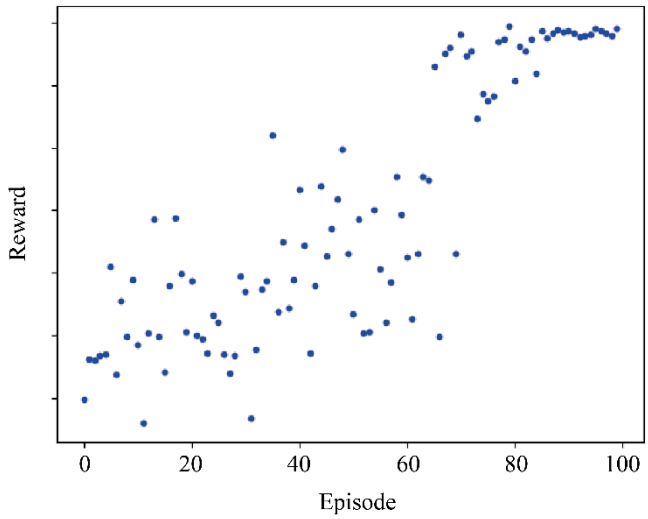

Fig. 6-4 Training process illustrated by the learning curve with obtained reward at the end of each exploration episode.

6.3.2 Stabilization control under large perturbations

Experiments on bumblebee flight control under large perturbations are conducted through applying large angular velocity perturbations along body axis of (x_b, y_b, z_b) and large velocity perturbations in directions of (x_g, y_g, z_g), which mimics the impact of wind gusts disturbance on tiny insect body [124, 144]. We employ the trained deep reinforcement learning policy as control strategy after adding the angular velocity disturbances 3% ω_{ref} ($\approx$ 20 rad/s) and the velocity disturbances 3% U_{ref} ($\approx$ 0.3 m/s) to trimmed hovering state of bumblebee. Fig. 6-5 and Fig. 6-6 depict the control results in terms of three body attitude (yaw, pitch, roll angles) and three body positions (X, Y, Z) under three yaw, pitch, and roll angular velocity perturbations, as well as three horizontal, lateral, and vertical velocity perturbations, respectively. Although all the large

perturbations in different directions result in deviations in three rotational angles and body positions, the deep reinforcement learning (DRL) controller based on four parameters of wing kinematics can largely achieve the 6-DoF stabilization in bumblebee hovering flight.

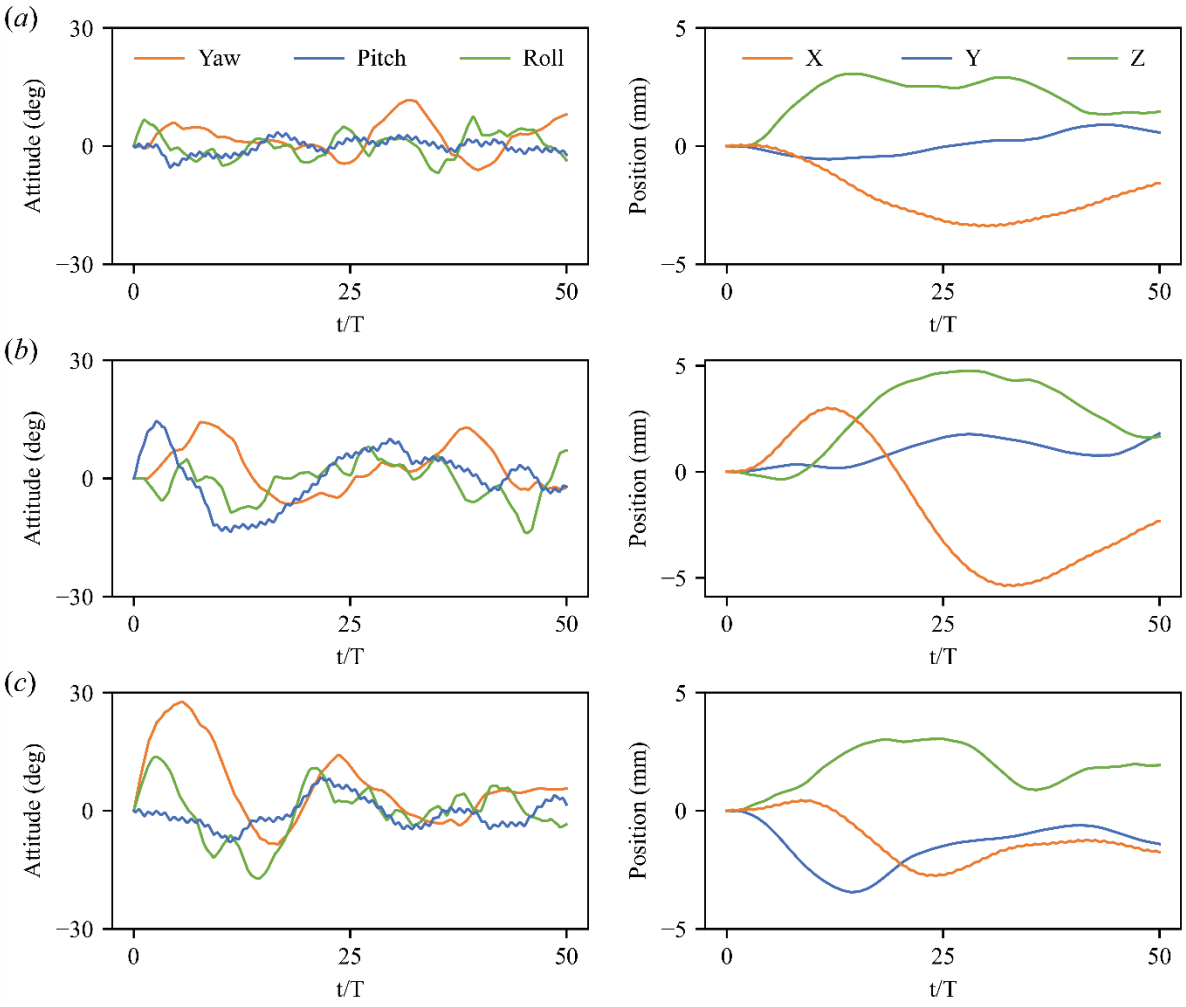

Fig. 6-5 Attitude and position control results under large angular velocity disturbances. (*a*) Yaw perturbation along body axis of z_b; (*b*) Pitch perturbation along body axis of y_b; (*c*) Roll perturbation along body axis of x_b.

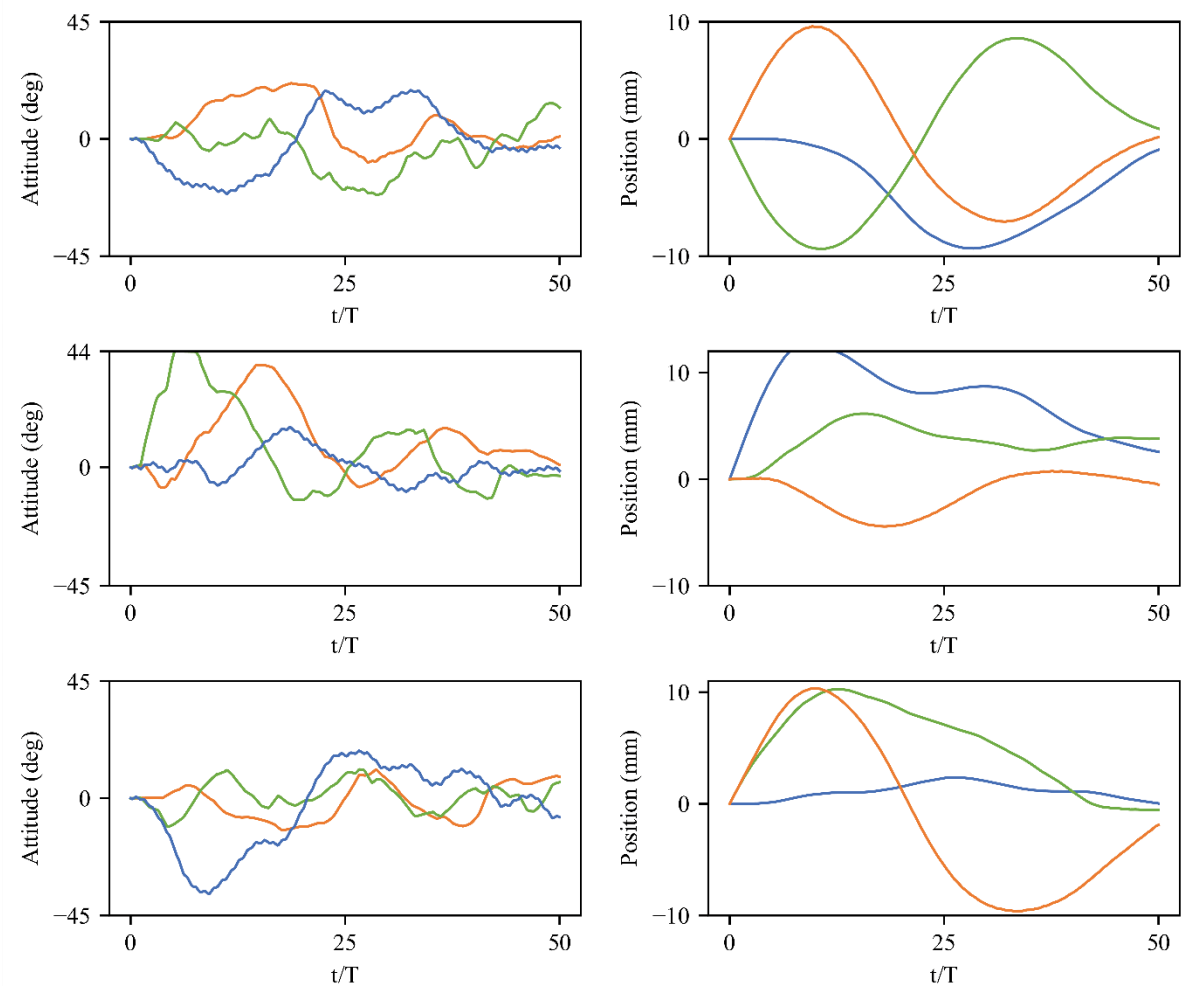

Fig. 6-6 Attitude and position control results under large velocity perturbations. (*a*) Horizontal perturbation in direction of x_g; (*b*) Lateral perturbation in direction of y_g; (*c*) Vertical perturbation in direction of z_g.

Highly coupled features appear in time-course of sideways motions as well as the longitudinal motions, which were reported by Cai and Liu [129] based on the control results of PD controller for 6-DoF stabilization under larger perturbations. Strong coupling between yaw and roll motions can be noticed in Fig. 6-5(*a*, *c*), and lateral velocity perturbation in direction of y_g may induce large rotational deviations in yaw and roll angles (Fig. 6-6(*b*)). Meanwhile, large pitch deviation and horizontal deviation in direction of x_g can be caused via vertical velocity perturbation in direction of z_g (Fig. 6-6(*c*)). The

horizontal deviation occurs to be comparable with the vertical deviation under large vertical velocity perturbation, which was even greater utilizing the PD controller presented by Cai and Liu [129]. Similar results of DRL control as PD control on the correlation between sideways and longitudinal motions under large yaw and roll perturbations are additionally shown in Fig. 6-5(*a*, *c*). The discrepancy lies in that remarkable deviations appear in horizontal and vertical directions rather than the pitch angles. The attitude control based on DRL policy under large perturbations can be achieved at around 25 wing-beat strokes of bumblebee including the yaw, pitch and roll rotational angles, which is comparatively slower than the control results of 10 strokes with PD controller [129] as well as the experimental observations on various insect flights [123, 124, 125, 126, 127]. However, the same restoring time of approximately 50 strokes are needed for DRL controller to obtain the position control in terms of horizontal, lateral and vertical motions after large perturbations, which may be less essential compared with the attitude stabilization [145].

Despite the different dynamic responses, the highly coupling and nonlinear feature of bumblebee hovering stabilization under large perturbations are still uncovered based on the deep reinforcement learning control strategy. More importantly, since the DRL controller is proved to be effective and robust under randomly given large perturbations in any degrees of freedom without optimization of control parameters as PD controller, the four-wing-kinematics-based flight control strategy solved by deep reinforcement learning will be of significant impact on the autonomous controller design for insect-inspired flight systems and flapping-wing MAVs.

6.4 Concluding remarks

In this section, we have developed a simulation framework with bio-inspired flight intelligence controller optimized by deep reinforcement learning (DRL) tasked with achieving bumblebee hovering stabilization under large perturbations. A high-fidelity Open AI Gym environment is established coupling a CFD data-driven aerodynamic model and a 6-DoF flight dynamic model tailored to provide fast aerodynamics prediction and mimic a wide array of realistic flight conditions. We propose a unique wing kinematics-based flight control strategy optimized by Soft Actor-Critic (SAC) algorithm, which is proven to be successful with action space of 4 for stabilization under full disturbances from 6 degrees of freedom. Fast control within 25 strokes after large perturbations could be obtained in body attitude stabilization of yaw, pitch and roll angles while it takes more time for body position stabilization of horizontal, lateral and vertical motions. The DRL controller is demonstrated to be of effectiveness and robustness under random perturbations in any directions without special treatments for controller implementation, which will give solutions and inspire the autonomous controller design for insect-inspired flapping-wing MAVs.

Chapter 7 Conclusion and perspectives

7.1 Conclusions

Systematic simulation-based studies on mechanics analysis underlying biological flapping flight in terms of unsteady aerodynamics, energetics and scaling law are presented in this thesis. To study how the interplay between flapping wings and the flying body affects the aerodynamics and energetics of insect forward flight over a broad range of flight velocities, a computational framework integrating high-fidelity CFD wing-body model and CFD-driven genetic algorithm is developed for exploring the near-field flow structures, the aerodynamic force produced, and the power consumption over a broad range of parameter space defined by aspect ratio, wing-to-body mass ratio, and reduced frequency during trimmed flapping flight. A universal macro-aerodynamic principle is also unraveled to unify the biofluid wave by deriving a scaling argument *We*, which correlates the transition of wave energy between transverse (lateral motion of flapping wings) and longitudinal (forward movement of body) wave with energetic cost over a variety of species including insects, bats and birds at various flight speeds.

For unsteady aerodynamics, both the leading-edge-vortex-based and body-vortex-based mechanisms, as well as their velocity-dependent interactions augment the aerodynamic force for forward flight of various speeds of insect. Since the universal leading-edge vortex (LEV) becomes stronger with increasing flight velocity and creates most of the aerodynamic force, the unique body vortex involving a rear-body vortex and a thorax vortex induced by wing-body interaction augment the vertical force by up to 10%, particularly for forward flight of intermediate and high velocities. The velocity-dependent body vortex is due to the interplay between the intense head vortex and the leading-edge

vortex induced by the wing-body interaction at high flight velocities.

For flapping energetics, the body-mass-specific time-averaged total mechanical power forms a *J*-shaped power curve with increasing flight velocity, and the power cost decreases for the realistic wing-body model, with the greatest energy saving of 3% occurring due to the interplay between flapping wings and body, particularly for flight at intermediate and high velocities.

The novel Wave Energy number (*We*) representing the transition of wave energy between transverse and longitudinal wave provides a universal scaling law that biological flights obey a specific *Re*-*We* principle ($We^v \propto Re^{-0.7}$, $We^h \propto Re^{-0.2}$) covering all the bio-fluid regimes and the wave energy transition is achieved within a narrow range of Strouhal number (*St*). Our findings further point to an important mechanism that bio-flyers may prefer to maximize the flight-speed-specific *We* via regulating stroke frequency and amplitude, which further demonstrates that the wave phenomenon in bio-locomotion is an ultimate propulsive strategy as consequence of evolution in nature.

7.2 Innovative points

Below are the innovative points of this dissertation on the integrated mechanistic analysis of unsteady aerodynamics, energetics and scaling in bioflights:

- The effects of wing-body interactions on velocity-dependent aerodynamic performance are unveiled with leading-edge-vortex-based and body-vortex-based mechanisms, as well as their correlations with aerodynamic forces production and power consumption.
- A universal biofluid wave-based scaling law in biological flights over a broad range of Reynolds numbers and flight velocities is uncovered, which offers an ultimate propulsive strategy for bio-locomotors.

- A novel wing kinematics-based deep reinforcement learning strategy is developed to achieve robust control under 6-DoF large disturbances for hovering stabilization, which inspires autonomous controller design for flapping-wing MAVs.

7.3 Future tasks

7.3.1 Flexible wing-body interactions in insect forward flight

The systematic analysis provides an overall understanding of the wing-body interaction in terms of the unsteady aerodynamics and energetics for various forward-flight velocities of the hawk moth, which should help to provide the design guideline of biomimetic flapping MAVs. Note that the CFD wing-body models are established by assuming a rigid wing and body and the prescribed wing-body kinematics. How the flexible structures, including flexible wings and wing hinges, and the deformable body [5, 12, 30, 88, 89] work interactively and complementarily to alter the wing-body interaction and thus the unsteady aerodynamic performance while retaining robustness in various flight velocities remains an open question. This leaves us future challenges to unveil the passive and active mechanisms associated with flexible wing-body interactions in insect forward flight.

7.3.2 Deep reinforcement learning for locomotion control in FMAVs

The reinforcement learning controller is demonstrated to generalize well to severe disturbances conditions such as wind gusts for hovering stabilization. Since the point-to-point locomotion like takeoff and pollination [146] are quite common in insect flapping flight, the exploration for flight mode control such as hovering-forward transfer as well as flight trajectory optimization are still essential issues. Fei *et al* [134] presented a control policy based on deep reinforcement learning for goal-directed maneuvering of flapping-wing MAV to mimic the hummingbird's takeoff. A bio-inspired flight intelligence

controller optimized by the state-of-art RL algorithms tasked with achieving robust and autonomous locomotion control remains a challenge for flapping-wing MAVs and requires further solution.

Achievements

Papers

[1] **Y. Xue**, X. Cai and H. Liu, 2022 Effects of wing-body interaction on Hawk-moth aerodynamics and energetics at various flight velocities. *Physics of Fluids* 34, 051915.

[2] **Y. Xue**, X. Cai, D. Kolomenskiy, R. Xu and H. Liu, 2022 Elastic storage enables robustness of flapping wing dynamics. *Bioinspiration & Biomimetics* 17, 045003.

[3] **Y. Xue**, X. Zhang, X. Cai, R. Xu and H. Liu, Biofluid wave-based scaling laws in biological flight of insects, bats and birds. (To be submitted)

[4] **Y. Xue**, X. Cai, R. Xu and H. Liu, Wing kinematics-based flight control strategy in insect-inspired flight systems: deep reinforcement learning gives solutions and inspires controller design in fMAVs. (To be submitted)

Conferences

[1] **Y. Xue** and H. Liu, Biofluid wave-based scaling laws in biological flapping flights. The Japan Society of Mechanical Engineers, 33rd Bio-Frontier Seminar, Kobe, 2022.

[2] **Y. Xue**, X. Cai and H. Liu, Aerodynamics and energetics in hawkmoth forward flight. The Japan Society for Computational Engineering and Science, 15th World Congress on Computational Mechanics & 8th Asia Pacific Congress on Computational Mechanics, Yokohama, 2022.

[3] **Y. Xue**, X. Cai and H. Liu, Aerodynamics and energetics in forward flight of hawkmoth. The Society for Experimental Biology, Annual Conference, Belgium, 2021.

[4] **Y. Xue** and H. Liu, A macroscopic aerodynamic scaling of biological flights. The Japan Society of Mechanical Engineers, 31st Bio-Frontier Seminar, 2020.

References

[1] F.E. Fish, C.M. Schreiber, K.W. Moored, G. Liu, H. Dong and H. Bart-Smith, 2016 Hydrodynamic performance of aquatic flapping: efficiency of underwater flight in the manta *Aerospace* **3**, 20.

[2] Y. Chen, E.F. Helbling, N. Gravish, K. Ma and R.J. Wood, 2015 Hybrid aerial and aquatic locomotion in an at-scale robotic insect in *2015 IEEE/RSJ International Conference on Intelligent Robots and Systems (IROS),* 331-338.

[3] Y. Chen, H. Wang, E.F. Helbling, N.T. Jafferis, R. Zufferey, A. Ong, K. Ma, N. Gravish, P. Chirarattananon, M. Kovac and R.J. Wood, 2017 A biologically inspired, flapping-wing, hybrid aerial-aquatic microrobot *Science Robotics* **2**, 5619.

[4] W. Shyy, H. Aono, C. Kang and H. Liu, 2013 *An introduction to flapping wing aerodynamics.* Cambridge University Press.

[5] H. Liu, 2020 Simulation-based insect-inspired flight systems *Curr. Opin. Insect Sci.* **42**, 105-109.

[6] A.R. Ennos, 1989 Comparative functional-morphology of the wings of diptera *Zool. J. Linn. Soc.* **96**, 27-47.

[7] S.P. Sane, 2003 The aerodynamics of insect flight *J. Exp. Biol.* **206**, 4191-4208.

[8] H. Liu, S. Ravi, D. Kolomenskiy and H. Tanaka, 2016b Biomechanics and biomimetics in insect-inspired flight systems *Phil. Trans. R. Soc.* B **371**, 20150390.

[9] H. Liu, 2009 Integrated modelling of insect flight: from morphology, kinematics to aerodynamics *J. Comput. Phys.* **228**, 439-459.

[10] H. Liu, C.P. Ellington, K. Kawachi, C. Van Den Berg and A.P. Willmott, 1998 A computational fluid dynamic study of hawk moth hovering *J. Expl Biol.* **201**, 461-477.

[11] H. Liu and H. Aono, 2009 Size effects on insect hovering aerodynamics: an integrated computational study *Bioinspir. Biomim.* **4**, 015002.

[12] W. Shyy, H. Aono, S.K. Chimakurthi, P. Trizila, C.K. Kang, C.E.S. Cesnik and H. Liu, 2010 Recent progress in flapping wing aerodynamics and aeroelasticity *Pro Aerosp Sci* **46**, 284-327.

[13] C.P. Ellington, C. Van Den Berg, A.P. Willmott and A.L.R. Thomas, 1996 Leading-edge vortices in insect flight *Nature* **384**, 626-630.

[14] M.H. Dickinson, F.O. Lehmann, S.P. Sane, 1999 Wing rotation and the aerodynamic basis of insect flight *Science* **284**, 1954-1960.

[15] J. Young, S.M. Walker, R.J. Bomphrey, G.K. Taylor, A.L.R. Thomas, 2009 Details of insect wing design and deformation enhance aerodynamic function and flight efficiency *Science* **325**, 1549-1552.

[16] A.R. Ennos, 1989 The kinematics and aerodynamics of the free flight of some Diptera *J. Expl Biol*. **142**, 49-85.

[17] B.W. Tobalske, D.R. Warrick, C.J. Clark, D.R. Powers, T.L. Hedrick, G.A. Hyder and A.A. Biewener, 2007 Three-dimensional kinematics of hummingbird flight *J. Expl Biol*. **210**, 2368-2382.

[18] A.P. Willmott and C.P. Ellington, 1997a The mechanics of flight in the hawk moth Manduca sexta. I. Kinematics of hovering and forward flight *J. Expl Biol*. **200**, 2705-2722.

[19] C.P. Ellington, 1984 The aerodynamics of hovering insect flight. III. Kinematics *Phil. Trans. R. Soc. Lond.* B **305**, 41-78.

[20] M.H. Dickinson and K.G. Gotz, 1993 Unsteady aerodynamic performance of model wings at low Reynolds numbers *J. Expl Biol*. **174** (1), 45-64.

[21] H. Liu and K. Kawachi, 1998 A numerical study of insect flight *J. Comput. Phys*. **146**, 124-156.

[22] T. Maxworthy, 1979 Experiments on the Weis-Fogh mechanism of lift generation by insects in hovering flight. Part 1. Dynamics of the 'fling' *J. Fluid Mech*. **93**, 47-63.

[23] A.K. Brodsky, 1991 Vortex formation in the tethered flight of the peacock butterfly Inachis 10 L and some aspects of insect flight evolution *J. Expl Biol*. **161**, 77-95.

[24] A.P. Willmott, C.P. Ellington and A.L.R. Thomas, 1997 Flow visualization and unsteady aerodynamics in the flight of the hawk moth, Manduca sexta *Phil. Trans. R. Soc. Lond.* B **352**, 303-316.

[25] R.B. Srygley and A.L.R. Thomas, 2002 Unconventional lift-generating mechanisms in free-flying butterflies *Nature* **420**, 660-664.

[26] A.R. Thomas, G.K. Taylor, R.B. Srygley, R.L. Nudds and R.J. Bomphrey, 2004 Dragonfly flight: Free-flight and tethered flow visualizations reveal a diverse array of unsteady lift-generating mechanisms, controlled primarily via angle of attack *J. Expl Biol*. **207**, 4299-4323.

[27] R.J. Bomphrey, G.K. Taylor and A.L.R. Thomas, 2009 Smoke visualization of free-flying bumblebees indicates independent leading-edge vortices on each wing pair *Exp. Fluids* **46**, 811-821.

[28] R.J. Bomphrey, N.J. Lawson, N.J. Harding, G.K. Taylor and A.R. Thomas, 2005 The aerodynamic of Manduca sexta: Digital particle image velocimetry analysis of the leading-edge vortex *J. Expl Biol*. **208**, 1079-1094.

[29] R.J. Bomphrey, 2006 Insects in flight: Direct visualization and flow measurements *Bioinspir. Biomim.* **1**, 1-9.

[30] R.J. Bomphrey, 2012 Advances in animal flight aerodynamics through flow measurement *Evol Biol* **39**, 1-11.

[31] Y. Zheng, Y. Wu and H. Tang, 2015 Force measurements of flexible tandem wings in hovering and forward flights *Bioinspir. Biomim.* **10**, 016021.

[32] A. Hedenström and L.C. Johansson, 2015 Bat flight: aerodynamics, kinematics and flight morphology *J. Expl Biol*. **218**, 653-663.

[33] M. Sun and J.H. Wu, 2003 Aerodynamic force generation and power requirements in forward flight in a fruit fly with modeled wing motion *J. Expl Biol*. **206**, 3065-3083.

[34] J. Wu and M. Sun, 2005 Unsteady Aerodynamic Forces and Power Requirements of a Bumblebee in Forward Flight *Act. Mech. Sin.* **21**, 207-217.

[35] J.K. Wang and M. Sun, 2005 A computational study of the aerodynamics and forewing-hindwing interaction of a model dragonfly in forward flight *J. Expl Biol*. **208**, 3785-3804.

[36] F.B. Tian, H. Luo, J. Song and X.Y. Lu, 2013 Force production and asymmetric deformation of a flexible flapping wing in forward flight *J. Fluids Struct.* **36**, 149-161.

[37] C. Hefler, R. Noda, H.H. Qiu and W. Shyy, 2020 Aerodynamic performance of a free-flying dragonfly—A span-resolved investigation *Phys. Fluids*. **32**, 041903.

[38] L. Zheng, T.L. Hedrick and R. Mittal, 2013 Time-varying wing-twist improves aerodynamic efficiency of forward flight in butterflies *PLoS ONE*. **8**, e53060.

[39] N. Yokoyama, K. Senda, M. Lima and N. Hirai, 2013 Aerodynamic forces and vortical structures in flapping butterfly's forward flight *Phys. Fluids*. **25**, 021902.

[40] H. Wan, H. Dong and K. Gai, 2015 Computational investigation of cicada aerodynamics in forward flight *J. R. Soc. Interface* **12**, 20141116.

[41] G. Liu, H. Dong and C. Li, 2016 Vortex dynamics and new lift enhancement mechanism of wing–body interaction in insect forward flight *J. Fluid Mech*. **795**, 634-651.

[42] J. Song, B.W. Tobalske, D.R. Powers, T.L. Hedrick and H. Luo, 2016 Three-dimensional simulation for fast forward flight of a calliope hummingbird *R. Soc. open sci.* **3**, 160230.

[43] J. Yao and K.S. Yeo, 2020 Forward flight and sideslip manoeuvre of a model hawk moth *J. Fluid*

Mech. **896**, A22.

[44] J. Yao and K. S. Yeo, 2019 Free hovering of hummingbird hawkmoth and effects of wing mass and wing elevation *Comput. Fluids* **186**, 99–127.

[45] S. E. Farisenkov, D. Kolomenskiy, N.A. Lapina, P.N. Petrov, T. Engels, F-O Lehmann, R. Onishi, H. Liu, A.A. Polilov, 2022 Novel flight style and light wings boost flight performance of tiny beetles. *Nature*. **602** (7895), 96-102.

[46] X. Cheng and M. Sun, 2021 Wing kinematics and aerodynamic forces in miniature insect Encarsia formosa in forward flight *Phys. Fluids*. **33**, 021905.

[47] M.J. Lighthill, 1973 On the Weis-Fogh mechanism of lift generation *J. Fluid Mech*. **60**, 1-17.

[48] T. Weis-Fogh, 1973 Quick estimates of flight fitness in hovering animals, including novel mechanisms for lift production *J. Expl Biol*. **59**, 169-230.

[49] J.M. Birch and M.H. Dickinson, 2003 The influence of wing–wake interactions on the production of aerodynamic forces in flapping flight *J. Exp. Biol*. **206**, 2257-2272.

[50] C. Van Den Berg and C.P. Ellington, 1997 The three-dimensional leading-edge vortex of a hovering model hawk moth *Phil. Trans. R. Soc. Lond.* B **352**, 329-340.

[51] S. Wang, X. Zhang, G. He and T. Liu, 2014 Lift enhancement by dynamically changing wingspan in forward flapping flight *Phys. Fluids.* **26**, 061903.

[52] W. Shyy and H. Liu, 2007 Flapping wings and aerodynamic lift: the role of leading-edge vortices *AIAA J.* **45**, 2817-2819.

[53] J.M.V. Rayner, 1979b A vortex theory of animal flight. Part 2. The forward flight of birds *J. Fluid Mech.* **91**, 731-763.

[54] P.J. Phlips, R.A. East and N.H. Pratt, 1981 An unsteady lifting line theory of flapping wings with application to the forward flight of birds *J. Fluid Mech.* **112**, 97-125.

[55] R. Dudley, 1991 Biomechanics of flight in neotropical butterflies: Aerodynamics and mechanical power requirements *J. Expl Biol.* **159**, 335-357.

[56] H. Nagai, K. Isogai, T. Fujimoto and T. Hayase, 2009 Experimental and numerical study of forward flight aerodynamics of insect flapping wing *AIAA J.* **47**, 730-742.

[57] Y. Yao and K.S. Yeo, 2018 Longitudinal free flight of a model insect flyer at low Reynolds number *Comput. Fluids.* **162**, 72-90.

[58] J. Wang, Y. Ren, C. Li and H. Dong, 2019 Computational investigation of wing-body interaction and its lift enhancement effect in hummingbird forward flight *Bioinspir*. *Biomim*. **14,** 046010.

[59] H. Aono, F. Liang and H. Liu, 2008 Near- and far-field aerodynamics in insect hovering flight: an integrated computational study *J. Expl Biol*. **211**, 239-257.

[60] B. Liang and M. Sun, 2011 Aerodynamic interactions between contralateral wings and between wings and body of a model insect at hovering and small speed motions *Chin. J. Aeronaut.* **24** 396-409.

[61] A. Shahzad, F.B. Tian, J. Young and J. C. S. Lai, 2018 Effects of hawkmoth-like flexibility on the aerodynamic performance of flapping wings with different shapes and aspect ratios *Phys. Fluids* **30**, 091902.

[62] R.R. Harbig, J. Sheridan and M.C. Thompson, 2014 The role of advance ratio and aspect ratio in determining leading-edge vortex stability for flapping flight *J. Fluid Mech*. **751**, 71-105.

[63] K. Suzuki, I. Okada and M. Yoshino, 2019 Effect of wing mass on the free flight of a butterfly-like model using immersed boundary-lattice Boltzmann simulations *J. Fluid Mech.* **877**, 614–647.

[64] R. Xu, X. Zhang and H. Liu, 2021 Effects of wing-to-body mass ratio on insect flapping flights *Phys*. *Fluids*. **33**, 021902.

[65] A.P. Willmott and C.P. Ellington, 1997b The mechanics of flight in the hawkmoth Manduca sexta. II. Aerodynamic consequences of kinematic and morphological variation *J. Expl Biol*. **200**, 2723-2745.

[66] R. Dudley and C.P. Ellington, 1990b Mechanics of forward flight in bumblebees: II. Quasi-steady lift and power requirements *J. Expl Biol*. **148**, 53-88.

[67] K. Warfvinge, M. KleinHeerenbrink and A. Hedenström, 2017 The power–speed relationship is U-shaped in two free-flying hawkmoths (Manduca sexta) *J. R. Soc. Interface* **14**, 20170372.

[68] R.M. Alexander, 1997 The U, J and L of bird flight *Nature* **390**, 13.

[69] P.J. Butler 2016 The physiological basis of bird flight *Phil. Trans. R. Soc. B* **371**, 20150384.

[70] B.W. Tobalske, T.L. Hedrick, K.P. Dial and A.A. Biewener, 2003 Comparative power curves in bird flight *Nature* **421**, 363-366.

[71] L.C. Johansson, M. Maeda, P. Henningsson and A. Hedenström, 2018 Mechanical power curve measured in the wake of pied flycatchers indicates modulation of parasite power across flight speeds *J. R. Soc. Interface* **15**, 20170814.

[72] G. K. Taylor, R. L. Nudds and A. L. R. Thomas, 2003 Flying and swimming animals cruise at a Strouhal number tuned for high power e-ciency *Nature* **425**, 707-711.

[73] M. Gazzola, M. Argentina and L. Mahadevan, 2014 Scaling macroscopic aquatic locomotion

Nature Phys **10**, 758-761.

[74] G. Li, H. Liu, U.K. Müller, C.J. Voesenek and J.L. van Leeuwen, 2021 Fishes regulate tail-beat kinematics to minimize speed-specific cost of transport *Proc. R. Soc. B.* **288**, 20211601.

[75] V.A. Tucker, 1970 Energetic cost of locomotion in animals *Comp. Biochem. Physiol.* **34**, 841-846.

[76] G. Li, U.K. Müller, J.L. van Leeuwen and H. Liu, 2016 Fish larvae exploit edge vortices along their dorsal and ventral fin folds to propel themselves *J. R. Soc. Interface* **13**, 20160068.

[77] R.J. Templin 2000 The spectrum of animal flight: insects to pterosaurs *Progress in Aerospace Sciences* **36**, 393-436.

[78] D.L. Altshuler, W.B. Dickson, J.T. Vance, S.P. Roberts and M.H. Dickinson, 2005 Short-amplitude high-frequency wing strokes determine the aerodynamics of honeybee flight *PNAS* **102**, 18213–18218.

[79] T.J. Mueller, 2001 *Fixed and flapping wing aerodynamics for micro air vehicle applications. Prog. Astronaut. Aeronaut.* **195**, Reston, VA: AIAA.

[80] D. Floreano and R.J. Wood, 2015 Science, technology and the future of small autonomous drones *Nature* **521**, 460-466.

[81] G.C. de Croon, M.A. Groen, C.D. Wagter, B. Remes, R. Ruijsink and B.W. van Oudheusden, 2012 Design, aerodynamics and autonomy of the DelFly *Bioinspir. Biomim.* **7**, 025003.

[82] T. Nakata, H. Liu, Y. Tanaka, N. Nishihashi, X. Wang and A. Sato, 2011 Aerodynamics of a bioinspired flexible flapping-wing micro air vehicle *Bioinspir. Biomim.* **6**, 045002.

[83] M. Keennon, K. Klingebiel, H. Won and A. Andriukov, 2012 Development of the nano hummingbird: a tailless flapping wing micro air vehicle In *50th AIAA Aerospace Sciences Meeting including the New Horizons Forum and Aerospace Exposition, AIAA* 20112-20588.

[84] R.J. Wood, B. Finio, M. Karpelson, K. Ma, N.O. Pérez-Arancibia, P.S. Sreetharan, H. Tanaka, J.P. Whitney, 2012 Progress on 'pico' air vehicles *Int. J. Robot. Res.* **31**, 1292-1302.

[85] J.P. Whitney and R.J. Wood, 2012 Conceptual design of flapping-wing micro air vehicles *Bioinspir. Biomim.* **7**, 036001.

[86] N.T. Jafferis, E.F. Helbling, M. Karpelson and R.J. Wood, 2019 Untethered flight of an insect-sized flapping-wing microscale aerial vehicle *Nature* **570**, 491-495.

[87] R.L. Harne and K.W. Wang, 2015 Dipteran wing motor-inspired flapping flight versatility and effectiveness enhancement *J. R. Soc. Interface* **12**, 20141367.

[88] T. Nakata and H. Liu, 2012 A fluid-structure interaction model of insect flight with flexible wings

J. Comput. Phys. **231**, 1822-1847.

[89] T.T. Nguyen, D. Shyam Sundar, K.S. Yeo and T.T. Lim, 2016 Modeling and analysis of insect-like flexible wings at low Reynolds number *J. Fluid Struct.* **62**, 294-317.

[90] T. Nakata, H. Liu and R.J. Bomphrey, 2015 A CFD-informed quasi-steady model of flapping-wing aerodynamics *J. Fluid Mech.* **783**, 323-343.

[91] R.J. Bomphrey, T. Nakata, N. Phillips and S.M. Walker, 2017 Smart wing rotation and trailing-edge vortices enable high frequency mosquito flight *Nature* **544**, 92–95.

[92] X. Cai, D. Kolomenskiy, T. Nakata and H. Liu, 2021 A CFD data-driven aerodynamic model for fast and precise prediction of flapping aerodynamics in various flight velocities *J. Fluid Mech.* **915**, A114.

[93] N. Hansen, S.D. Müller and P. Koumoutsakos, 2003 Reducing the time complexity of the derandomized evolution strategy with covariance matrix adaptation (CMA-ES) *Evolutionary Computation* **11**, 1-18.

[94] N. Hansen and S. Kern, 2004 *Evaluating the CMA Evolution Strategy on Multimodal Test Functions* 282-291. Springer.

[95] J.C.R. Hunt, A.A. Wray and P. Moin, 1988 Eddies, stream, and convergence zones in turbulent flows *Center for turbulence research report CTR-S88*, 193-208.

[96] K.Y. Ma, P. Chirarattananon, S.B. Fuller and R.J. Wood, 2013 Controlled flight of a biologically inspired insect-scale robot *Science* **340**, 603-607.

[97] X.X. Wang and Z.N. Wu, 2010 Stroke-averaged lift forces due to vortex rings and their mutual interactions for a flapping flight model *J. Fluid Mech.*, **654**, 453-472.

[98] H. Liu, T. Nakata, G. Li and D. Kolomenskiy, 2017 Unsteady bio-fluid dynamics in swimming and flying *Act. Mech. Sin.* **33**, 663-684.

[99] Y. Jiang, P. Zhao, X. Cai, J. Rong, Z. Dong, H. Chen, P. Wu, H. Hu, X. Jin, D. Zhang and H. Liu, 2022 Bristled-wing design of materials, microstructures, and aerodynamics enables flapping flight in tiny wasps *iScience* **25**, 103692.

[100] X. Cheng and M. Sun, 2018 Very small insects use novel wing flapping and drag principle to generate the weight-supporting vertical force *J. Fluid Mech.* **855**, 646–670.

[101] S.N. Fry, R. Sayaman, M.H. Dickinson 2005 The aerodynamics of hovering flight in Drosophila *J. Expl Biol.* **208**, 2303-2318.

[102] D. Kolomenskiy, S. Ravi, R. Xu, K. Ueyama, T. Jakobi, T. Engels, T. Nakata, J. Sesterhenn, K. Schneider, R. Onishi, H. Liu 2019 The dynamics of passive feathering rotation in hovering flight

of bumblebees *J. Fluids Struct.* **91**, 102628.

[103] J.M. Birch and M.H. Dickinson, 2001 Spanwise flow and the attachment of the leading-edge vortex on insect wings *Nature* **412**, 729-733.

[104] A. Hedenström, L.C. Johansson, M. Wolf, R. Von Busse, Y. Winter, G. R. Spedding, 2007 Bat flight generates complex aerodynamic tracks *Science* **316**, 894-897.

[105] B. Liang and M. Sun, 2013 Aerodynamic interactions between wing and body of a model insect in forward flight and maneuvers *J. Bionic Eng.* **10**, 19-27.

[106] S. S. Bhat, J. Zhao, J. Sheridan, K. Hourigan and M. C. Thompson, 2019 Aspect ratio studies on insect wings *Phys. Fluids* **31**, 121301.

[107] W. Nachtigall and U. Hanauer-Thieser, 1992 Flight of the honeybee. V. Drag and lift coefficients of the bee's body; implications for flight dynamics *J Comp Physiol B.* **162**, 267-277.

[108] D. Chen, D. Kolomenskiy, T. Nakata and H. Liu, 2018 Forewings match the formation of leading-edge vortices and dominate aerodynamic force production in revolving insect wings *Bioinspir. Biomim.* **13**, 016009.

[109] T. J. Pedley, 1977 *Scale effects in animal locomotion*. Cambridge University Press.

[110] S. Vogel, 1996 *Life in moving fluids: The physical biology of flow*. Princeton University Press.

[111] S. Childress, 1981 *Mechanics of swimming and flying*. Cambridge University Press.

[112] J.J. Videler, 1993 *Fish Swimming*. London: Chapman & Hall.

[113] Y. Xue, X. Cai and H. Liu, 2022 Effects of wing–body interaction on hawk moth aerodynamics and energetics at various flight velocities *Phys. Fluids.* **34**, 051915.

[114] M.S. Triantafyllou, G.S. Triantafyllou and D.K.P. Yue, 2000 Hydrodynamics of fishlike swimming *Annual Review of Fluid Mechanics* **32**, 33-53.

[115] U.M. Norberg, T.H. Kunz, J.F. Steffensen, Y. Winter and O.V. Helversen, 1993 The cost of hovering and forward flight in a nectar-feeding bat Glossophaga soricina, estimated from aerodynamic theory *J. Exp. Biol* **182**, 207-227.

[116] J.M. Wakeling and C.P. Ellington, 1997 Dragonfly flight. II. Velocities, accelerations and kinematics of flapping flight *J. Exp. Biol* **200**, 557-582.

[117] B.W. Tobalske and K.P. Dial, 1996 Flight kinematics of black -billed magpies and pigeons over a wide range of speeds *J. Exp. Biol* **199**, 263-280.

[118] B.W. Tobalske, W.L. Peacock and K.P. Dial, 1999 Kinematics of flap-bounding flight in the zebra finch over a wide range of speeds *J. Exp. Biol* **202**, 1725-1739.

[119] C. Van Den Berg and J.M.V. Rayner, 1995 The moment of inertial of bird wings and the inertial

power requirement for flapping flight *J. Exp. Biol* **198**, 1655-1664.

[120] K.J. Park, M. Rosen and A. Hedenström, 2001 Flight kinematics of the barn swallow over a wide range of speeds in a wind tunnel *J. Exp. Biol* **204**, 2741-2750.

[121] C.J. Pennycuick, 1990 Predicting wingbeat frequency and wavelength of birds *J. Exp. Biol* **150**, 171-185.

[122] C.J. Pennycuick, M.R. Fuller, J.J. Oar and S.J. Kirkpatrick, 1994 Falcon versus grouse: flight adaptations of a predator and its prey *J. Avian Biol* **25**, 39-49.

[123] L. Ristroph, A.J. Bergou, G. Ristroph, K. Coumes, G.J. Berman, J. Guckenheimer, Z. J. Wang and I. Cohen, 2010 Discovering the flight autostabilizer of fruit flies by inducing aerial stumbles *Proc. Natl. Acad. Sci.* **107**, 4820-4824.

[124] T. Beatus, J.M. Guckenheimer and I. Cohen, 2015 Controlling roll perturbations in fruit flies *J. R. Soc. Interface* **12**, 20150075.

[125] B. Cheng, X. Deng and T.L. Hedrick, 2011 The mechanics and control of pitching manoeuvres in a freely flying hawkmoth (manduca sexta) *J. Exp. Biol.* **214**, 4092.

[126] L. Ristroph, G. Ristroph, S. Morozova, A. J. Bergou, S. Chang, J. Guckenheimer, Z.J. Wang, I. Cohen, 2013 Active and passive stabilization of body pitch in insect flight *J. R. Soc. Interface* **10**, 20130237.

[127] S.C. Whitehead, T. Beatus, L. Canale, I. Cohen, 2015 Pitch perfect: how fruit flies control their body pitch angle *J. Exp. Biol.* **218**, 3508.

[128] X. Zhang and H. Liu, 2018 A three-axis PD control model for bumblebee hovering stabilization, *J. Bionic Eng.* **15**, 494-504.

[129] X. Cai and H. Liu, 2021 A six-degree-of-freedom proportional-derivative control strategy for bumblebee flight stabilization. *J. Biomech. Sci. Eng.* **16**, 21-00113.

[130] J. Yao and K.S. Yeo, 2019 A simplified dynamic model for controlled insect hovering flight and control stability analysis *Bioinspir. Biomim.* **14**, 056005.

[131] T.L. Hedrick and T.L. Daniel, 2006 Flight control in the hawkmoth Manduca sexta: the inverse problem of hovering *J. Exp. Biol*. **209**, 3114.

[132] R.S. Sutton and A.G. Barto, 2018 *Reinforcement learning: An introduction*. MIT Press.

[133] E. Bøhn, E.M. Coates, S. Moe and T.A. Johansen, 2019 Deep reinforcement learning attitude control of fixed-wing UAVs using proximal policy optimization In *2019 International Conference on Unmanned Aircraft Systems (ICUAS) IEEE,* 523-533.

[134] F. Fei, Z. Tu, Y. Yang, J. Zhang and X. Deng, 2019 Flappy hummingbird: An open source

dynamic simulation of flapping wing robots and animals In *2019 International Conference on Robotics and Automation (ICRA) IEEE*, 9223-9229.

[135] J. Schulman, S. Levine, P. Abbeel, M.I. Jordan and P. Moritz, 2015 Trust region policy optimization In *International Conference on Machine Learning (ICML)*, 1889-1897.

[136] J. Schulman, F. Wolski, P. Dhariwal, A. Radford and O. Klimov, 2017b Proximal policy optimization algorithms *arXiv preprint arXiv:1707.06347*.

[137] V. Mnih, A.P. Badia, M. Mirza, A. Graves, T.P. Lillicrap, T. Harley, D. Silver and K. Kavukcuoglu, 2016 Asynchronous methods for deep reinforcement learning In *International Conference on Machine Learning (ICML)*, 1928-1937.

[138] T.P. Lillicrap, J.J. Hunt, A. Pritzel, N. Heess, T. Erez, Y. Tassa, D. Silver and D. Wierstra, 2015 Continuous control with deep reinforcement learning *arXiv preprint arXiv: 1509.02971*.

[139] S. Fujimoto, H. van Hoof and D. Meger, 2018 Addressing function approximation error in actor-critic methods. *arXiv preprint arXiv:1802.09477*.

[140] T. Haarnoja, A. Zhou, P. Abbeel and S. Levine, 2018c Soft actor-critic: Off-policy maximum entropy deep reinforcement learning with a stochastic actor. In *International Conference on Machine Learning (ICML)*, 1861-1870.

[141] T. Haarnoja, A. Zhou, K. Hartikainen, G. Tucker, S. Ha, J. Tan, V. Kumar, H. Zhu, A. Gupta, P. Abbeel and S. Levine, 2018 Soft actor-critic algorithms and applications *arXiv preprint arXiv:1812.05905*.

[142] G. Gebert, P. Gallmeier and J. Evers, 2002 Equations of motion for flapping flight In *AIAA Atmospheric Flight Mechanics Conference and Exhibit*, 4872.

[143] M. Sun, J. Wang and Y. Xiong, 2007 Dynamic Flight Stability of Hovering Insects *Acta Mech. Sin.* **23**, 231-246.

[144] S. Ravi, J.D. Crall, A. Fisher, S.A. Combes, 2013 Rolling with the flow: bumblebees flying in unsteady wakes *J. Exp. Biol*. **216**, 4299.

[145] T. Jakobi, D. Kolomenskiy, T. Ikeda, S. Watkins, A. Fisher, H. Liu, S. Ravi, 2018 Bees with attitude: the effects of directed gusts on flight trajectories *Biology Open* **7**, bio034074.

[146] M. Matthews and S. Sponberg, 2018 Hawkmoth flight in the unsteady wakes of flowers *J. Exp. Biol*. **221**, 179259.